

TIME	EVENT
	<p>Loss of Voice Communications. The last audio transmission from <i>Columbia</i>, “Roger, [truncated mid-word]...”¹⁶ was cut off at GMT 13:59:32.136 (EI+923.136). A short-duration loss of voice communications was not unexpected because it coincided with the approximate time at which the on-board communications systems was to switch from the West TDRS to either the East TDRS or the ground station at Kennedy Space Center. [<i>STS-107 A/G recording</i>]¹⁷</p>
	<p>LOS. The last valid downlink frame was accepted by the Orbiter Data Reduction Complex at GMT 13:59:32.136 (EI+923.136).¹⁸ The following measurements were recorded in the MCC at the time of LOS:</p> <ul style="list-style-type: none"> • Cabin pressure = 14.64 pounds per square inch absolute (psia) • Cabin temperature = 71.6°F (22°C) • Humidity = 37.9% • ppO₂ levels (three sensors) <ul style="list-style-type: none"> 3.14 psia (sensor A), 3.14 psia (sensor B), 3.16 psia (sensor C) • Pressure change rate (DP/dt) = 0.004 psi/minute (within sensor bias limit for 0) • Partial pressure of carbon dioxide (ppCO₂) = 1.96 mmHg • Cabin temperature setting = full cool • Nitrogen (N₂) supply pressures <ul style="list-style-type: none"> 1011 psia (System 1), 1067 psia (System 2) • O₂ supply pressures <ul style="list-style-type: none"> 822 psia (System 1), 809 psia (System 2)
	<p>Start of First Period of RGPC-1 Data. Data reconstructed from GMT 13:59:32.136 (EI+923.136) to GMT 13:59:37.396 (EI+928.396).</p>
	<p>It is possible that the crew noticed the aileron trim increasing. Per procedures, no crew action would be required until the trim reached 3 degrees.</p>
	<p>There is an increase in the roll error as the orbiter uses roll control to correct the yaw error and rate. [<i>RGPC</i>]</p>

¹⁶*Columbia* Accident Investigation Board Report, Volume I, August 2003, p. 43.

¹⁷*Columbia* Accident Investigation Board Report, Volume I, August 2003, p. 43.

¹⁸STS-107 Investigation Action Response: OVE-204 Crew Inputs After Loss of COMM (Voice); CAIB-MRT-00099, 03/10/2003.

TIME	EVENT
	 The FCS Channel 4 problems that were developing at GMT 13:59:31 (EI+922) had progressed to the point that the FCS Channel 4 fail flags tripped (1 Hz) on all aerosurface actuators. [<i>Master Timeline, Rev. 15 Baseline; RGPC</i>]
	 During the RGPC-1 period, the vehicle remains in AUTO guidance and control.
	 Ground-based video coverage is regained.
13:59:33 (EI+924)	 PASS FSM: FCS CH 4. The fault message is associated with the removal of FCS Channel 4 from the control loop and would have been annunciated on the crew displays. [<i>TDRS-E data</i>]
	 Master Alarm. ¹⁹ The Master Alarm associated with the FCS Channel 4 fault message would have been annunciated to the crew (figure 1.2-39).

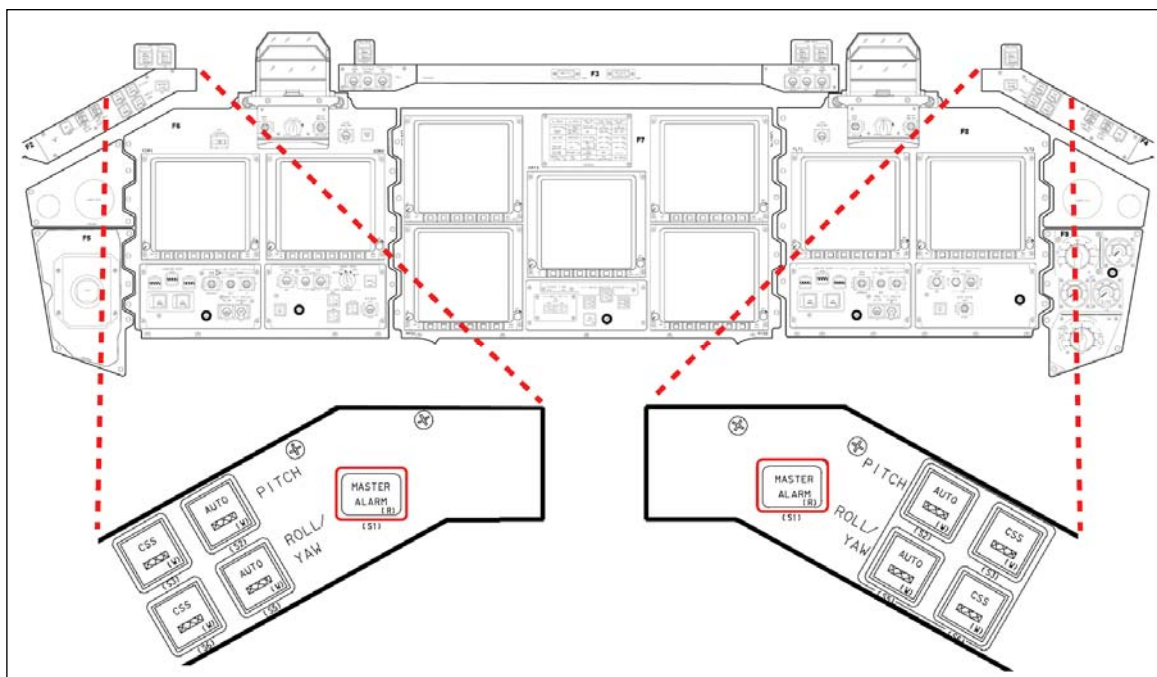


Figure 1.2-39. Location of the master alarm light. [Adapted from the Space Shuttle Systems Handbook]

¹⁹STS-107 Investigation Action Response: OVE-204 Crew Inputs After Loss of COMM (Voice); CAIB-MRT-00099, p. 4, 03/10/2003.

TIME	EVENT
13:59:34 (EI+925)	 FSP Message Downlink Stack (five deep): FSP1: FCS CH 4 32/13:59:33.68 FSP2: SM0 TIRE PRESS L OB 32/13:58:56.26 FSP3: SM0 TIRE PRESS L IB 32/13:58:49.54 FSP4: SM0 TIRE PRESS L IB 32/13:58:41.84 FSP5: SM0 TIRE PRESS L OB 32/13:58:39.94
13:59:36 (EI+927)	 Third RCS Yaw Jet (R4R) Begins Firing Continuously. Reconstructed data indicate that the DAP commanded a third RCS yaw jet (R4R) to fire at GMT 13:59:36.8 (EI+927.8) and that it fired continuously until end of data at GMT 13:59:37.4 (EI+928.4). [<i>Master Timeline, Rev. 15 Baseline</i>]
13:59:37 (EI+928)	 Aileron trim exceeds 3 degrees.
13:59:37 (EI+928)	 LOSS OF CONTROL NO-EARLIER-THAN (NET) TIME
13:59:37 (EI+928)	 Beginning of the Orbiter Pitch-up. Based on the time of the ROLL REF message (GMT 13:59:46 (EI+937)) and the divergence from the drag profile required to generate the ROLL REF alarm, this is the probable time that control was lost due to the probable loss of hydraulic pressure to the control surfaces. The loss of hydraulic pressure would have resulted in a Master Alarm being annunciated and the orbiter pitching up. While the drag had yet to diverge out of bounds of the drag profile, the orbiter was no longer in controlled flight. This marks the beginning of the transition from a controlled glide to an uncontrolled ballistic entry. Orbiter heating, lift, and drag would no longer be controlled, the ballistic number would be constantly changing with the changing attitudes, and downrange control would be lost (figure 1.2-40).

TIME

EVENT

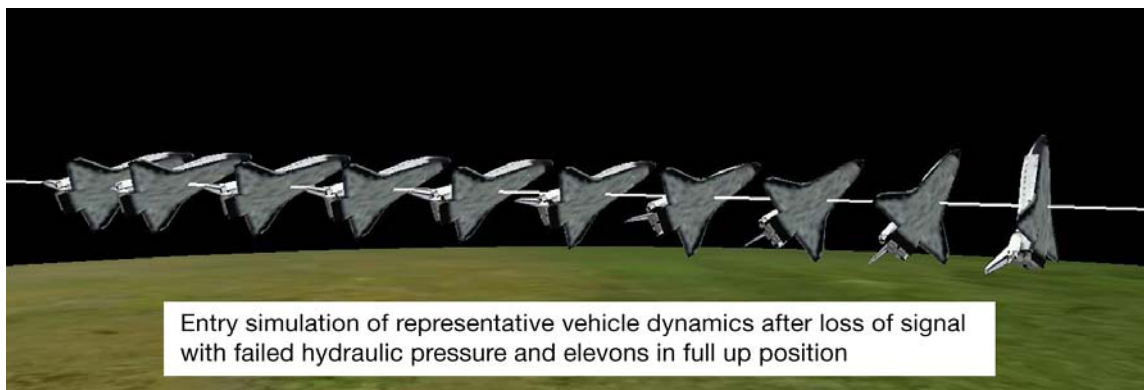


Figure 1.2-40. Sequence (1-second intervals) showing a simulation of orbiter loss of control pitch-up from GMT 13:59:37 (EI+928) to GMT 13:59:46 (EI+937). White line indicates vehicle trajectory relative to the ground.



Video imagery shows a dynamically changing orbiter trail after GMT 13:59:37 (EI+928) with a braided or corkscrew appearance, implying motion of the orbiter. However, the specific attitude of the orbiter cannot be derived from ground-based imagery. Brightening events, objects separating, “puffs,” and splitting of the trail are all seen in the video during this timeframe. Ballistic analysis of debris could not positively correlate shedding events seen in the video to a specific orbiter source. However, it is known that the left wing and left OMS pod were being compromised.²⁰ Figure 1.2-41 shows video frames from GMT 13:59:35.5 (EI+925.5) through GMT 13:59:43.5 (EI+934.5) and displays some of these dynamic changes, although they are much more clearly seen in the video.

²⁰Columbia Accident Investigation Board Report, Volume I, August 2003, p. 68.

TIME **EVENT**

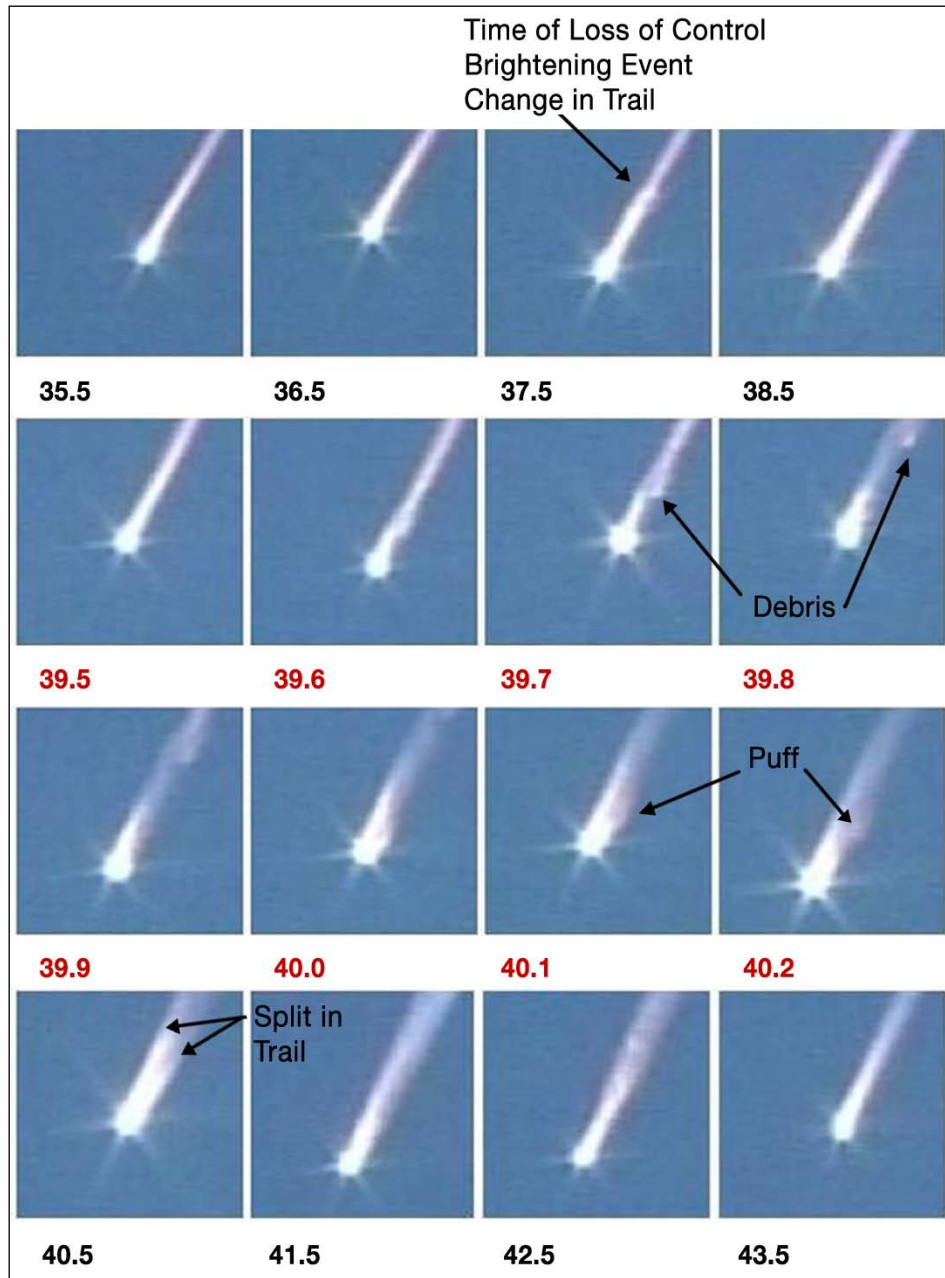


Figure 1.2-41. Video frame captures from ground-based video, beginning at GMT 13:59:35.5 (EI+926.5) and ending at GMT 13:59:43.5 (EI+937.5). The numbers below each frame indicate the seconds after GMT 13:59:00. The frames in the first and last rows are 1 second apart. The frames in the second and third rows are 0.1 second apart.



Beginning of Off-nominal Attitude and Loads. The CDR/Seat 1 and PLT/Seat 2 would have been aware of the off-nominal movement of the orbiter based on information from the flight displays and from the changing view in the forward windows. MS2/Seat 4 and MS4/Seat 3 may also have been aware of this information.

TIME	EVENT
	 The rate of change of the elevon trim had reached the maximum allowed by the DAP while in AUTO. [<i>Master Timeline, Rev. 15 Baseline</i>]
	 RGPC data recorded the left rudder pedal transducer assembly (RPTA) was near null at GMT 13:59:37.118 (EI+928.118), ²¹ indicating that there were no crew inputs on the rudder pedals.
	 Fourth RCS Yaw Jet (R1R) Begins Firing. Reconstructed data indicate that the DAP commanded a fourth RCS yaw jet (R1R) to fire at GMT 13:59:37.3 (EI+928.3). The R1R fired continuously until the end of data at 13:59:37.396 (EI+928.396). With four jets firing continuously, the fuel supply would be rapidly depleted (within 30 seconds).
	 End of RGPC-1. This is the end of the ~5-second period of RGPC data at GMT 13:59:37.396 (EI+928.396). ²² There were no confirmed indications of changes in positions of any of the switches on panel R2. ²³ No GPC data were recoverable for the next 25 seconds. ²⁴
13:59:44 (EI+935)	 Fuselage upper surface canopy thermocouple BP0439T (above window 2) starts to indicate an off-nominal sharp temperature increase followed by a drop to loss of sensor signal. ²⁵
13:59:46 (EI+937)	 ROLL REF. BFS recorded the PASS generating a Roll Alarm fault message. At this time, the drag of the vehicle had exceeded the limits of the entry drag profile. This message occurred less than 10 seconds after the fourth yaw jet (R1R) began firing, suggesting a rapid change in orbiter aerodynamics. [<i>Master Time Line, Rev. 15 Baseline; BFS, RGPC-2</i>]
	 Debris A (possible Left OMS Pod Cover). ²⁶ Video analysis identifies GMT 13:59:46.67 (EI+937.67) as the earliest time at which Debris A is observed. Debris A was identified as possibly being the cover of the left OMS pod. Debris A fades from view on the video at GMT 14:00:22.97 (EI+973.97).

²¹STS-107 Investigation Action Response: OVE-204 Crew Inputs After Loss of COMM (Voice); CAIB-MRT-00099, p. 4, 03/10/2003.

²²STS-107 Investigation Action Response: OVE-204 Crew Inputs After Loss of COMM (Voice); CAIB-MRT-00099, p. 4, 03/10/2003.

²³STS-107 Investigation Action Response: OVE-204 Crew Inputs After Loss of COMM (Voice); CAIB-MRT-00099, p. 2, 03/10/2003.

²⁴Data in RGPC-2 had time-stamped data for some events that occurred during this 25-second period between RGPC-1 and RGPC-2.

²⁵OEX Data Evaluation of End of Mission Data for STS-107, Vehicle Data Mapping Team, OV-102 Investigation, 08/22/2003, Rev 2.

²⁶See Section 2.2, Figure 2.2-9 Debris Tree.

TIME	EVENT
13:59:52 (EI+943)	<p> At GMT 13:59:52.114 (EI+943.114) the BFS recorded the PASS generating an “L RCS LEAK” fault message. [RGPC-2] [<i>Master Timeline, Rev. 15 Baseline</i>].</p> <p> Debris D (possible Left OMS Pod). Video analysis identifies this as the earliest time at which Debris D is observed. Debris D was identified as possibly being the left OMS pod. (figure 1.2-42).</p>



Figure 1.2-42. Debris D is depicted in this frame.

14:00:01 (EI+952)	<p> At GMT 14:00:01.54 (EI+952.54) the BFS recorded an “L RCS LEAK” fault message. [<i>Master Timeline, Rev. 15 Baseline</i>]</p> <p> RHC Moved. The RHC moved beyond neutral between approximately GMT 14:00:01.7 (EI+952.7) and GMT 14:00:03.6 (EI+954.6). The uncertainty in the time of the event is due to the processing rates of signal detection, signal processing, and message annunciation. This event resulted in the DAP downmode RHC Fault message that was recorded at GMT 14:00:03.637 (EI+954.637). By GMT 14:00:3.678 (EI+954.678) the crew returned the DAP back to AUTO, indicating that this RHC movement was accidental.</p> <p> At GMT 14:00:01.90 (EI+952.90) the BFS recorded another “L RCS LEAK” fault message. [<i>Master Timeline, Rev. 15 Baseline</i>]</p>
14:00:02 (EI+953)	<p> Final Recovered GPS State Vector at GMT 14:00:02.12 (EI+953.12). These data were recovered from the MAGR.²⁷</p>

²⁷Columbia Investigation: GPS Receiver (MAGR) Memory Extraction Summary and Disposition presentation, May 12, 2003.

TIME	EVENT
	 <p>PASS FSM: LJET L RCS. This Class 2 alarm message may not be the result of the actual vehicle condition since the message was generated based on data from a sensor path that contained noise. If valid, the message is used to indicate when an RCS jet has failed on or failed off, or is leaking. The failed off condition could be an indication that the fuel was exhausted.</p>
	 <p>Beginning of Final Period of RGPC Data at GMT 14:00:02.660 (EI+953.660). Reconstructed GPC data (RGPC-2), lasting from GMT 14:00:02.660 (EI+953.660) to GMT 14:00:04.826²⁸ (EI+955.826), contained multiple bit errors.</p> <p>Vehicle rates during this period were (Note: there is some uncertainty with the NAV-derived parameters since the high rates may have resulted in corruption of the inertial measurement unit state):</p> <ul style="list-style-type: none"> • roll rate command from the DAP was at –5.0 deg/sec during the entire RGPC-2 period, indicating that the DAP was in AUTO the entire time (maximum control rates allowed: AUTO is –5.0 deg/sec, control stick steering (CSS) is –6.0 deg/sec) • Roll rate transitioned from +7 deg/sec (right roll) to –23 deg/sec (left roll) • Yaw rate was at the sensor maximum of 20 deg/sec (nose right) • Pitch rate was 5 deg/sec
	 <p>Debris B (Portion of Left Wing). Video analysis identifies this as the earliest time at which Debris B is observed.</p>
	 <p>Debris C (Portion of Left Wing). Video analysis identifies this as the earliest time at which Debris C is observed.</p>
14:00:03 (EI+954)	 <p>At GMT 14:00:03.47 (EI+954.47) BFS recorded an “L OMS TK P” fault message. This message is annunciated when the left OMS oxidizer ullage pressure (V43P4221C) or fuel tank ullage pressure (V43P4321C) is out of limits either high or low.</p>
	 <p>DAP DNMODE RHC Fault Message. At GMT 14:00:03.637 (EI+954.637) the DAP Downmode RHC Fault message was recorded in the fault message buffer due to the movement of the RHC beyond neutral between approximately GMT 14:00:01.7 (EI+952.7) and GMT 14:00:03.6 (EI+954.6). This fault message was corroborated by an initialization flag for the aerojet DAP roll stick function. During the final 2-second RGPC period, all available data indicate that the RHC remained</p>

²⁸STS-107 Investigation Action Response: OVE-204 Crew Inputs After Loss of COMM (Voice); CAIB-MRT-00099, p. 1, 03/10/2003.

TIME	EVENT
	<p>in the detent position and that the DAP was in AUTO. This supports the RHC being bumped and the crew immediately returning the DAP to AUTO.</p>
	<p> DAP in AUTO. At GMT 14:00:03.678 (EI+954.678) the RPGC data recorded the first indication from PASS that the DAP was in the AUTO mode.²⁹ This requires a manual crew input by either the CDR/Seat 1 or the PLT/Seat 2. This manual command was in response to the RHC movement at GMT 14:00:01 (EI+952) moding the DAP out of AUTO. Because moding the DAP from CSS to AUTO requires either the CDR/ Seat 1 or the PLT/Seat 2 to press two buttons located on both panels F6 (CDR/Seat 1) and F8 (PLT/Seat 2), at least one crew member was conscious and able to respond to events that were occurring on board and that the vehicle dynamics were within human performance capabilities for this action.</p>
14:00:04 (EI+955)	<p> RHC in Detent. At GMT 14:00:04.179 (EI+955.179) the RGPC data recorded the first indication from PASS or BFS that the RHC was in detent.³⁰ This indicates that there were no manual inputs at this time on the RHC.</p>
	<p> MSG Reset on CRT 1. BFS recorded an MSG reset on CRT 1 some time after GMT 13:59:37 (EI+928) and before GMT 14:00:05 (EI+956).³¹ This event is part of the RGPC-2 data and is considered a valid input. This action would be a nominal crew response to a fault message and requires a crew member to manually acknowledge the message by keyboard entry on the C2 panel.</p>
	<p> End of RGPC-2. End of the final 2-second period of RGPC-2 data at GMT 14:00:04.826 (EI+955.826). At this time, the forward/mid/aft fuselage, PLBDs, right wing, and right OMS pod were still intact based on the following data: [<i>Master Timeline, Rev. 15 Baseline</i>]</p> <ul style="list-style-type: none"> • APUs were running and the panel R2 switches were ON. The APUs are located in the aftbody, indicating that this portion of the vehicle was still intact. • Water spray boiler (WSB) cooling was evident. The WSB is located in the aftbody, indicating that this portion of the vehicle was still intact and the data lines from it to the crew module were still intact.

²⁹STS-107 Investigation Action Response: OVE-204 Crew Inputs After Loss of COMM (Voice); CAIB-MRT-00099, 03/10/2003.

³⁰STS-107 Investigation Action Response: OVE-204 Crew Inputs After Loss of COMM (Voice); CAIB-MRT-00099, 03/10/2003.

³¹STS-107 Investigation Action Response: OVE-204 Crew Inputs After Loss of COMM (Voice); CAIB-MRT-00099, 03/10/2003.

TIME	EVENT
	<ul style="list-style-type: none"> • Panel R2 switches in nominal positions. Since panel R2 was recovered with switches in positions consistent with an attempted APU restart, this indicates that the switch throws occurred after this time. • Fuel cells were generating power, indicating that electrical power was still being produced. • Power reactant, storage, and distribution tanks and lines were intact, indicating that this portion of the vehicle was still relatively intact. • Main Propulsion System still intact indicated that the aft portion of the vehicle was still relatively intact. • Helium tanks and lines were intact. • Freon loops and radiators (located in the PLBDs) were intact; quantities, flow measurements, and pressure measurements were nominal. This indicates that the PLBDs were still intact at this time. • RHCs were in detent during the entire period of RGPC-2, indicating that the crew had not tried to manually control the vehicle during this time period. • Left RPTA indicated a small left rudder input/offset that remained nearly constant for the duration of RGPC-2, indicating that there may have been some pressure being applied on the pedal by one of the crew members. It should be noted that the RPTA signals are not transmitted to the flight control software at this phase of flight. In addition, the lack of hydraulic pressure would prevent control inputs to the control surfaces. • Communications and navigation systems in the forebody were performing nominally, indicating that this part of the vehicle was relatively intact. • Environmental Control and Life Support System (ECLSS) performance was nominal, indicating that the cabin environment was nominal.

The following systems were indicating off-nominal conditions:

- Hydraulic supply pressures were reading 0 psi and the reservoir quantities were at 0% on all three systems; the lack of hydraulic pressure results in the aerosurfaces (elevons, body flap, and rudder) were free to move in the wind stream.
- LIB and LOB elevon actuator temperatures were either OSL or no data existed.
- APU lube oil was possibly being overcooled by the WSB.
- The Flash Evaporator System appears to have shut down.
- Most of the left OMS pod sensors were OSL or off-scale high, or had no data available.

TIME	EVENT
	<ul style="list-style-type: none"> • The electrical power distribution circuit showed a general upward shift in main bus amps and a downward shift in main bus volts. • Alternating current (AC) Bus 3 (AC3) Phase A inverter was off-line; this would not impair crew or vehicle performance. • Elevated temperature readings were recorded at the bottom bondline centerline skin forward and aft of the wheel wells and at the portside structure over the left wing.
	 Another left wing piece separates based on ballistics analysis. This analysis was performed on a piece of recovered structure that was identified as being from the left wing.
14:00:05 (EI+956)	 End of GPC signal. The last GPC signal, which contained no recoverable data, was recorded at GMT 14:00:05.121 (EI+956.121).
	 PLT/Seat 2 takes actions in apparent attempt to restart APUs 2 and 3 . With the loss of hydraulic pressures and the vehicle LOC, the crew likely assumed a generic problem with the APUs. A crew module panel was recovered with switch configurations indicating an attempt by the PLT/Seat 2 to recover the hydraulic systems and hydraulic pressure by performing steps to initiate the restart of APUs 2 and 3. Switches for APU 1 were in the nominal position. Switches for hydraulic circulation pumps 2 and 3 were also in the “On” position. While turning on the hydraulic circulation pump is not on the emergency checklist, it nonetheless can provide some limited hydraulic pressure and shows good systems knowledge by the crew members as they worked to attempt to restore orbiter control. These actions took place after the end of RGPC-2 (after GMT 14:00:05 (EI+956)) and prior to loss of consciousness.
14:00:11 (EI+962)	 Video analysis identified a color change in the plume that is likely the result of an OMS tank rupturing.
14:00:13 (EI+964)	 The last MADS/OEX recorder data value (left wing spar cap sensor, V12G909A), marked GMT 14:00:13.439 (EI+964.439), is recorded. ³²

³²OEX Data Evaluation of End of Mission Data for STS-107, Vehicle Data Mapping Team, OV-102 Investigation, 08/22/2003, Rev 2.

TIME **EVENT**

**1.2.4 Phase 4: Catastrophic Event to Crew Module
Catastrophic Event
[GMT 14:00:18 (EI+969) through GMT 14:00:53 (EI+1004)]**

14:00:18 (EI+969)



CATASTROPHIC EVENT. The CE is a period of time during which the orbiter vehicle is undergoing a major structural breakup. At this time, the accelerations on the forebody were estimated to be 3.5 Gs. The breakup sequence progressed over several seconds. Analysis of ground-based video of the event established the first detectable signs at GMT 14:00:18 (EI+969). Based on engineering analysis, the CE is thought to have started with the compromise of the PLBDs, exposing the payload bay longeron sill to entry heating. The skin splice between the midbody and the X₀ 582 ring frame bulkhead area, aft of the starboard x-link, failed due to a combination of mechanical and thermal loads. The forebody rotated away from starboard to port, causing the port x-link to fail due to bending loads. As the forebody separated from the midbody, various power, data, and ECLSS lines failed and the crew module was free to move forward and strike the inside of the forward fuselage. At GMT 14:00:25 (EI+976), the separated forebody is marginally visible. The CE is further supported by a collection of evidence that includes ground-based video of a large debris-generating event, the loss of the MADS/OEX recorder function, and the debris footprint (figures 1.2-43 and 1.2-44).



Figure 1.2-43. The Catastrophic Event is depicted in these three frames of video that cover 0.1 second. There is no change in the magnification/zoom factor. The third frame represents GMT 14:00:18.3 (EI+969.3).

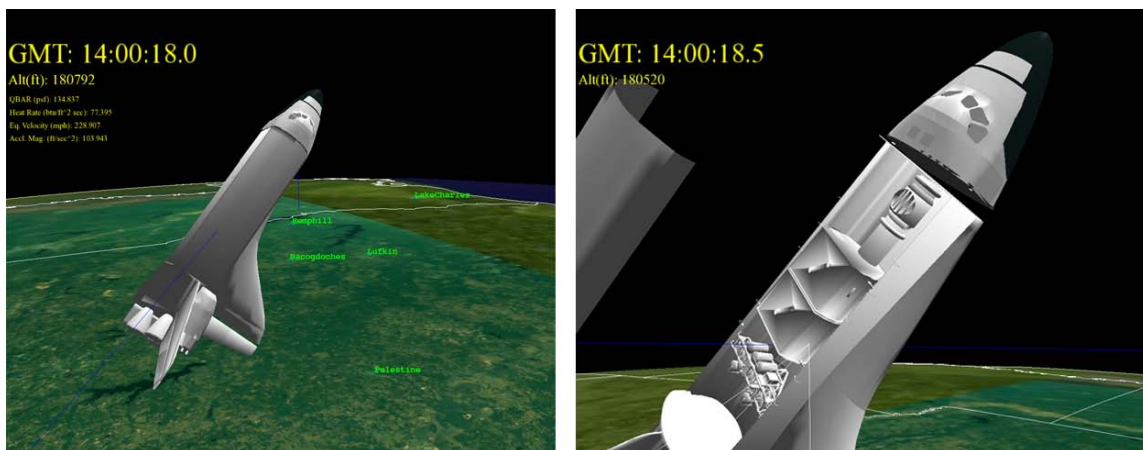


Figure 1.2-44. Simulation of the Catastrophic Event.

TIME**EVENT**

The separation of the forebody from the midbody resulted in:

- The crew module and forward fuselage becoming independent from the rest of the vehicle, moving farther downrange and remaining higher in altitude than the rest of the vehicle. Since there was no other debris ahead of the forebody, all material depositions and shock wave damage on the recovered forebody debris was generated by the forebody.
- Loss of electrical power – Electrical power for the orbiter systems is supplied from fuel cells located in Bays 1 and 2 of the midbody of the vehicle. Separation of the crew module and forward fuselage from the midbody caused a loss of power to the crew module. Loss of electrical power resulted in the loss of all powered systems, including:
 - Displays – The loss of displays resulted in a loss of all situational awareness from instrumentation.
 - Intercom System – The loss of the intercom system meant that crew-to-crew communications could only be performed by shouting.
 - Lighting – With the cabin lights lost, the only lighting was from the windows and the Cyalume chemical lights that are pre-positioned within the crew module and on the upper arms of the ACES of each of the crew members.
 - Ventilation – Electrically powered fans for circulating air through the cabin and the CO₂ scrubber shut down, resulting in a loss of cabin ventilation.
 - O₂ supply – Valves in the orbiter O₂ system are designed to close when power is lost, resulting in a loss of O₂ supply to the cabin and the suit O₂ hoses. Since none of the helmet visors were lowered and locked, it is unlikely that the crew members activated their emergency O₂ supplies since that step is performed after visors are lowered and locked.
 - MAGR – Last time value was recorded at GMT 14:00:18.6875 (EI+969.6875). No state vector data were recorded at this time.
- Sudden change in aerodynamic characteristics – The ballistic number of the forebody by itself is higher than the ballistic number of the rotating intact orbiter. This resulted in a reduction of drag with a corresponding reduction in translational force on the crew, estimated to have dropped from 3.5 Gs to 1 G.
- Unknown dynamic changes – In addition to the change in translational forces acting on the crew, the separation of the forebody resulted in a change to rotational loads.

TIME	EVENT
------	-------

Prior to the CE, the crew was experiencing rotational loads with the center of rotation located aft of the crew module at the center of mass of the orbiter. As a result of the crew module and forward fuselage separating from the rest of the orbiter, the rotational arm decreased (figure 1.2-45).

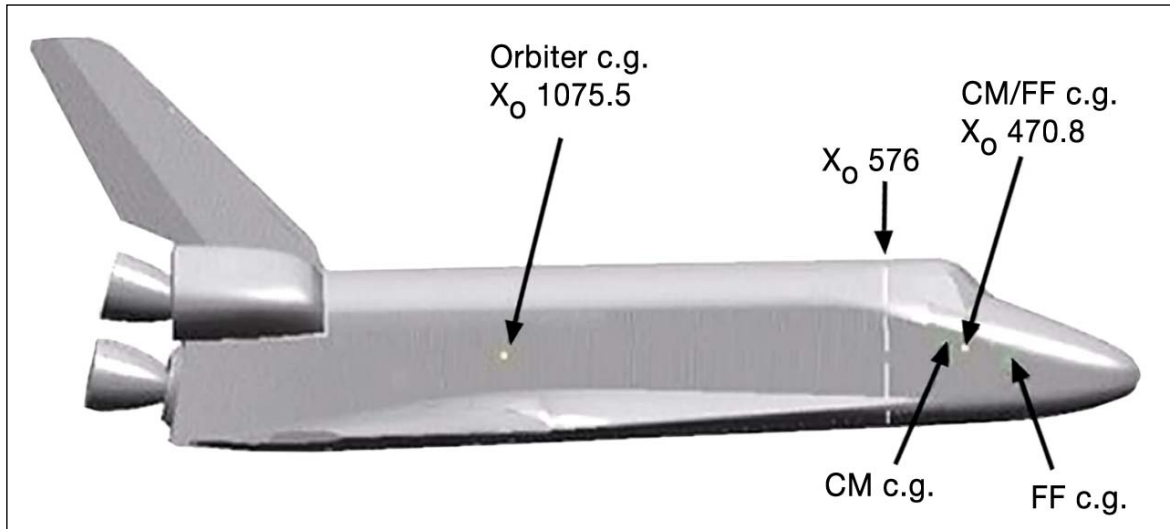


Figure 1.2-45. X-axis center-of-gravity locations for the intact orbiter, the crew module, the forward fuselage, and the forebody (crew module plus forward fuselage). The X_o 576 is the aft bulkhead of the crew module.

- Based on video analysis, triangulation data, and aerodynamic modeling, the initial rotation rate of the separated forebody was low, the rates built over time, and the forebody never trimmed.



The estimated vehicle state at GMT 14:00:18 (EI+969):

Alt = 181,000 feet [modeling]
Mach = 15 [modeling]
KEAS = 228 [modeling]
Qbar = 83 psf [modeling]



DEPRESSURIZATION BEGINS – NET Time. This is the first event of lethal potential.



Loss of consciousness and cessation of respiration.

14:00:19 (EI+970)



The MADS/OEX recorder stopped recording at GMT 14:00:19.44 (EI+970.44).³⁴

³³ This symbol is used to indicate a vehicle-related event that occurred after the separation of the crew module and forward fuselage from the midbody.

³⁴ Columbia Accident Investigation Board Report, Volume I, August 2003, p. 73.

TIME	EVENT
14:00:25 (EI+976)	 First visual indication that the orbiter had broken into multiple pieces (figure 1.2-46).

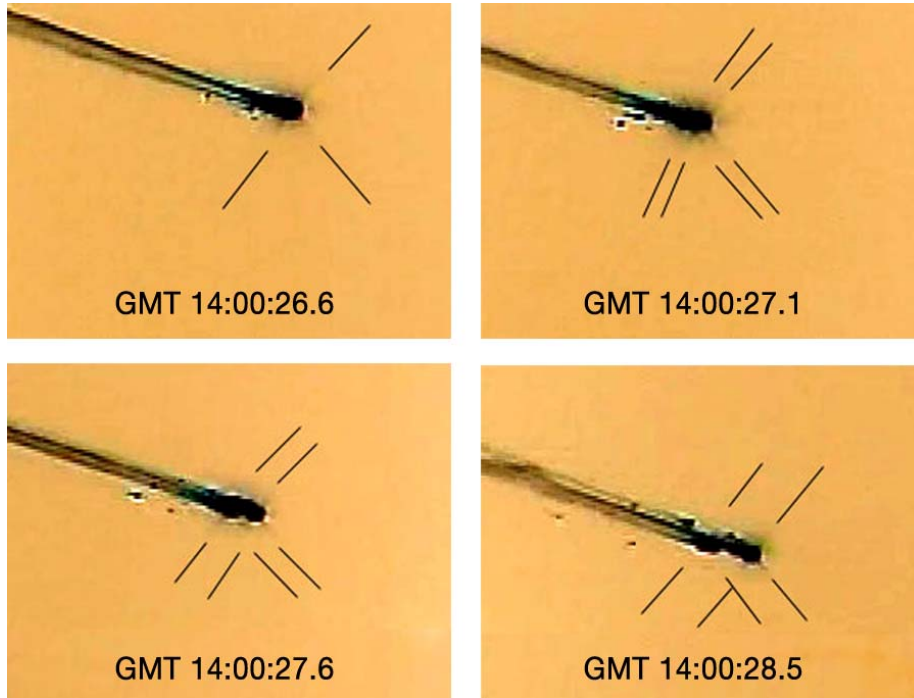


Figure 1.2-46. Color-inverted video images of the start of the double star event, GMT 14:00:26.6 (EI+977.6). Black lines have been added to more clearly identify the two separate objects.

14:00:35 (EI+986) ±5 sec	 DEPRESSURIZATION BEGINS – NLT Time. This time is based on the release times for items from a storage compartment within the crew module.
--------------------------	---

1.2.5 Phase 5: Crew Module Catastrophic Event to Total Dispersal [GMT 14:00:53 (EI+1004) through GMT 14:01:10 (EI+1021)]

14:00:53 (EI+1004)	 CREW MODULE CATASTROPHIC EVENT Begins. The CMCE is the initiation of a period of time during which the forebody was undergoing a major structural breakup. The breakup sequence progressed over several seconds and ends at approximately GMT 14:01:10 (EI+1021). Analysis of ground-based video of the event established the first detectable signs at GMT 14:00:53 (EI+1004). Based on engineering analysis, CMCE is thought to have started with the failure of the forward fuselage. Once the forward fuselage began to break away, the exposed crew module rapidly failed due to the combined effects of the high G-loads, aerodynamic forces, and thermal loads. The flight deck maintained structural integrity longer than the middeck (figure 1.2-47).
--------------------	--

TIME	EVENT
------	-------

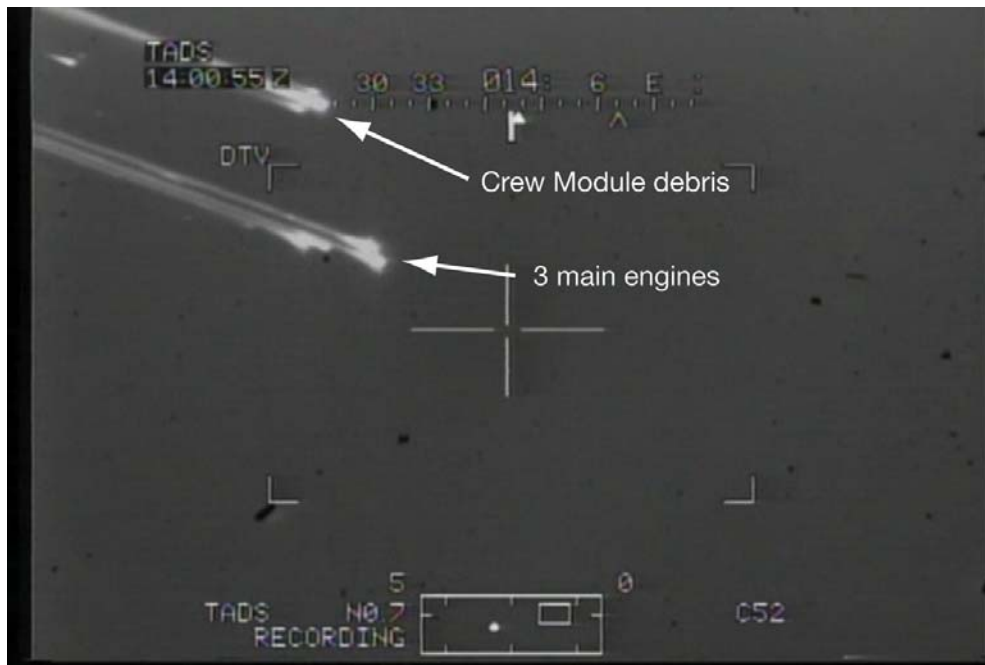


Figure 1.2-47. Image from Apache³⁵ video showing crew module debris (top cluster) and the three main engines (cluster to left of cross hairs).

		Thermal intrusion into the crew module – NLT time.
		Inertial reel straps fail – Metallic deposits on the inertial reel straps indicate that globules of molten metal were present in the crew module prior to the straps failing and retracting into the inertial reel housing.
14:00:57 (EI+1008)±5 sec		Based on ballistic analysis, a recovered piece of the forward RCS separated at this time.
14:00:59 (EI+1010)		DEPRESSURIZATION COMPLETE – NLT Time. Based on video evidence, the crew module no longer had sufficient structural integrity to maintain cabin pressure. However, the cabin depressurization was probably complete well before this time.
14:01:01 (EI+1012)±5 sec		Middeck CEE Released. Based on ballistic analysis, the earliest piece of recovered CEE from the middeck crew members separated at this time.
14:01:07 (EI+1018)±5 sec		Middeck Accommodation Rack (MAR) Separates. Based on ballistic analysis, the MAR, which was located on the port side of the middeck, separated at this time.

³⁵The “Apache” video was filmed from an Apache helicopter.

TIME	EVENT
14:01:08 (EI+1019)±5 sec	 Flight Deck CEE Released. Based on ballistic analysis, the earliest piece of recovered CEE from the flight deck crew members separated at this time.

1.2.6 Phase 6: Total Dispersal to ground impact [GMT 14:01:10 (EI+1021) through approximately GMT 14:35:00 (EI+3051)]

14:01:10 (EI+1021)	 TD – Forward fuselage and crew module have fragmented into pieces too small to be detected on any of the ground-based videos (figure 1.2-48).
--------------------	--



Figure 1.2-48. Image is from the Apache video. Dotted circle indicates area where crew module debris is last visible. The three points in the lower right are the three main engines.

14:35:00 (EI+3051)	  Approximate time at which the crew remains and the majority of the crew module debris completed the free fall to the ground.
--------------------	--

Chapter 2 – Vehicle Failure Assessment

2.1 Motion and Thermal Analyses

2.2 Orbiter Breakup Sequence

*2.3 Crew Cabin Pressure
Environment Analysis*

2.4 Forebody Breakup Sequence

2.1 Motion and Thermal Analyses

This section discusses the trajectory, dynamic attitude, and thermal analyses of the *Columbia* accident performed in support of the Spacecraft Crew Survival Integration Investigation Team (SCSIIT). The motion analyses provided information about the loads experienced by the crew and the vehicle through the evolving conditions. Because the thermal environment for atmospheric entry is highly dependent on the aerodynamic properties of an object as well as the aerodynamic conditions such as altitude and velocity, the aerodynamic analyses also provided reference data for thermal analyses. The purpose of the thermal analyses was to aid in understanding the probable failure sequence by comparing the physical condition of certain key items of debris with predicted entry heating.

“Trajectory” refers to the translational motion of an object relative to the Earth, and provides information about the deceleration of an object due to atmospheric drag. The trajectory of the intact orbiter after communications were lost was estimated from available aerodynamic data. However, this type of data did not exist for the forebody as a separate object following orbiter breakup at the Catastrophic Event (CE). An average ballistic number was approximated¹ for the forebody. A 3 degree-of-freedom trajectory simulation used this approximate ballistic number to estimate the trajectory of the forebody. The “reference trajectory” was a continuous trajectory used for ballistic and thermal analyses. The reference trajectory was a sequential combination of the trajectory of the intact orbiter followed by the trajectory of the forebody after separation from the orbiter.

“Dynamic attitude motion” refers to the rotational motion of an object relative to the trajectory. This information was necessary since aerodynamic drag was the predominant load on the vehicle. Because drag always acts in a direction opposite to a vehicle’s forward motion, a rotating vehicle will experience the drag force in varying directions relative to the body axes. Simulations were developed to characterize the dynamic attitude motion of the intact orbiter and the forebody. The first simulation modeled estimated dynamic attitude for the intact orbiter from loss of signal (LOS) to the CE. This simulation incorporated telemetry and the Modular Auxiliary Data System/orbiter experiment (MADS/OEX) recorder data into an existing orbiter aerodynamic model. The second simulation modeled the estimated dynamic attitude of the free-flying forebody from the CE to the Crew Module Catastrophic Event (CMCE). This simulation had no direct data available. The aerodynamic characteristics of the forebody were estimated and incorporated into an aerodynamic model. The rotational loads and attitudes were then combined with the drag loads identified through the trajectory analysis to estimate loads in all axes for both the intact orbiter and the forebody.

The data from these model-based analyses should be considered only as *representative* of the type of motion the vehicle and crew experienced. The results of these analyses were compared to a relative motion analysis obtained from ground-based video. The analyses were found to be in general agreement.

To better quantify the limits of crew survival for future flights, the survivability of an exposed crew module (CM) following orbiter breakup for ascent and entry conditions were examined from a thermal perspective. The results were compared to the estimates currently used in crew procedures and to the conditions experienced for both the *Challenger* and the *Columbia* accidents. Thermal analyses were also completed on individual recovered items to predict the amount of heating that they would have experienced given a specific

¹Ballistic number is an indicator of the performance of an un-powered object flying through the atmosphere. It is characterized by the ratio of the object’s weight over its aerodynamic drag.

release time. These results were compared to the thermal damage observed on debris items to confirm ballistic release times and to help sequence events.

The following is a summary of findings, conclusions and recommendations in this section:

Conclusion L3-1. Complete loss of hydraulic pressure to the aerosurfaces resulting from the breach in the left wing was the probable proximal cause for the vehicle loss of control.

Recommendation L3-2. Future vehicles should be designed with a separation of critical functions to the maximum extent possible and robust protection for individual functional components when separation is not practical.

Finding. The forebody and the CM of the orbiter are not aerodynamically stable in attitude with any initial rates or lateral center of gravity (c.g.) other than zero.

Finding. Triangulation results suggest that the free-flying forebody rotated at approximately 0.1 rev/sec in a multi-axis motion.

Conclusion L2-1. Between orbiter breakup and the forebody breakup, the free-flying forebody was rotating about all three axes at approximately 0.1 rev/sec and did not trim into a specific attitude.

Finding. The estimate for maximum thermal survivability on ascent of 280,000 feet is a reasonable estimate.

Finding. The maximum thermal survivable breakup altitude for the CM on entry is approximately 150,000 feet.

Conclusion L3-3. The actual maximum survivable altitude for a breakup of the space shuttle is not known.

Recommendation L2-2. Prior to operational deployment of future crewed spacecraft, determine the vehicle dynamics, entry thermal and aerodynamic loads, and crew survival envelopes during a vehicle loss of control so that they may be adequately integrated into training programs.

Recommendation L3-3. Future spacecraft design should incorporate crashworthy, locatable data recorders for accident/incident flight reconstruction.

Finding. Thermal analyses predicted that entry aeroheating alone was insufficient by an order of magnitude to produce the observed thermal damage on the x-links. Therefore, the x-links must have experienced other heating mechanism(s) in addition to normal entry heating.

Conclusion A13-1. Titanium may oxidize and combust in entry heating conditions dependent on enthalpy, pressure, and geometry.

Conclusion A13-2. The heating from a Type IV shock-shock impingement and titanium combustion (in some combination) likely resulted in the damage seen by the forward payload bay door rollers and the x-links.

Recommendation A13. Studies should be performed to further characterize the material behavior of titanium in entry environments to better understand optimal space applications of this material.

2.1.1 Intact orbiter trajectory

Figures 2.1-1 through 2.1-3 define the body axis coordinate system and the attitude angles that will be discussed in this section. Figure 2.1-1 defines the body axis coordinate system (X_{BY} , Y_{BY} , Z_{BY}) and the pitch, yaw, and roll angles. Figure 2.1-2 defines the angle of attack (α), and figure 2.1-3 defines sideslip (β). These angles are defined relative to the X_{BY} axis and the velocity vector (V). Proj(V) is the projection of the velocity vector (line of sight along the trajectory).

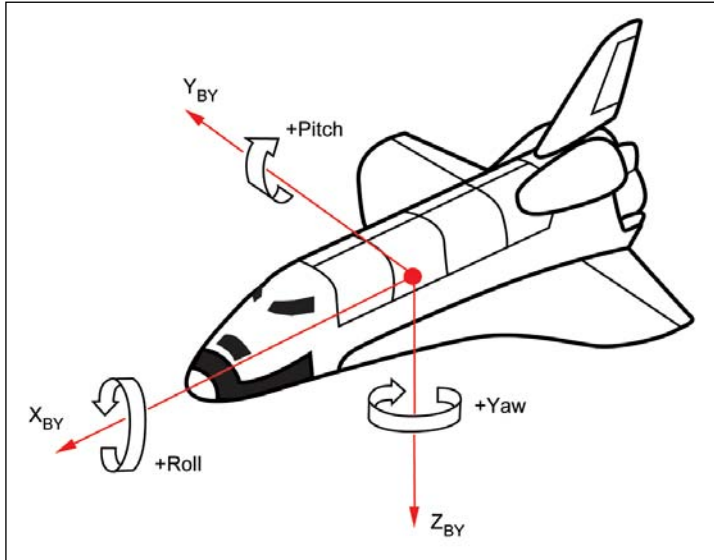


Figure 2.1-1. Depiction of the body axis coordinate system and pitch, yaw, and roll definitions.

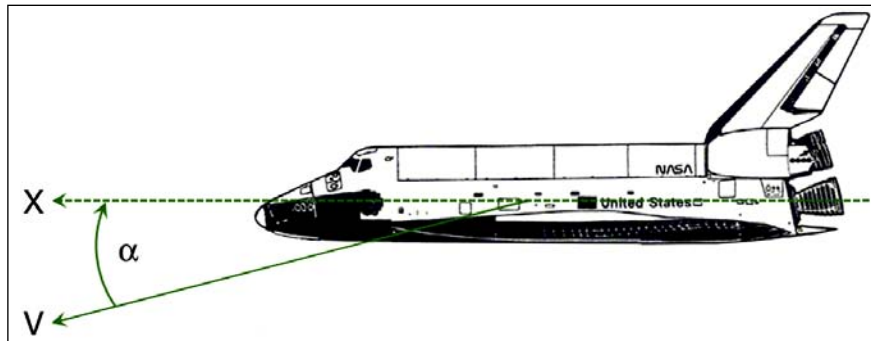


Figure 2.1-2. Depiction of angle of attack.

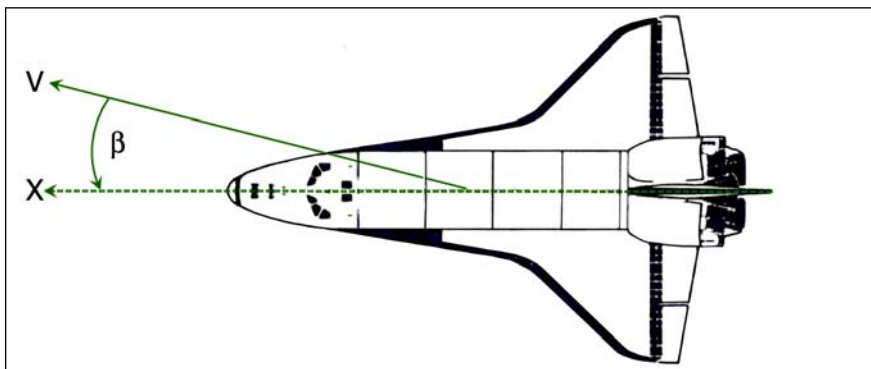


Figure 2.1-3. Depiction of sideslip.

Nominal dynamic, 3-axis coupled orbiter aerodynamic stability has been discussed in many documents and will not be discussed here. There are many documents available that discuss the orbiter's dynamic stability.^{2,3,4} The aerodynamic data used in this aerodynamic analysis were obtained from the Orbiter Aerodynamic Databook.⁵ The data in the Databook are limited to the operational range of the orbiter. After loss of control (LOC), the orbiter was probably out of that range in some parameters. However, no other data exists, and the Databook was the best source available. Engineering judgment was used to determine which data applied best to the conditions.

Some assumptions were necessary to provide a continuous reference trajectory for ballistic and thermal analyses. Four different sets of condition assumptions were used sequentially to determine the reference trajectory. To help clarify the differences for each of these phases, some discussion follows of these conditions and how they affected the trajectory.

An uncontrolled object entering the Earth's atmosphere is on a ballistic trajectory (see Ballistic Tutorial, Appendix). However, a vehicle may use aerodynamic controls and vehicle properties to generate lift, which modulates drag, to alter the ballistic number and, hence, the trajectory. The orbiter can generate lift when in the appropriate attitude. A simplified, static, 3-axis uncoupled analysis of aerodynamic stability shows that when in the high-altitude hypersonic flight regime, the orbiter is not statically stable in attitude. Active control is necessary to maintain orbiter stability. This active control is provided by the general purpose computers (GPCs) through the digital autopilot (DAP). The DAP uses the Flight Control System (FCS), a blend of Reaction Control System (RCS) jets and the elevons, body flap, and (at lower Mach numbers) rudder/speed brake aerosurfaces to control the orbiter attitude. As the orbiter descends into the atmosphere, the aerosurfaces have more control authority and the RCS jets play a lesser role in control.

The orbiter uses a drag-velocity profile to reduce its velocity, maintain heating and aerodynamic loads within orbiter limits, and reach the landing site. Figure 2.1-4 shows the entry drag-velocity profile and boundaries. The lower lift boundary is called the equilibrium glide boundary. This is typically defined as having 20% of vehicle lift remaining to adjust the trajectory, which is accomplished by modulating the angle of attack and bank angle. Bank angle also changes the trajectory laterally, so periodic roll reversals are accomplished to keep the orbiter from drifting too far crossrange.

²William T. Suit, "Summary of Longitudinal Stability and Control Parameters as Determined from Space Shuttle Columbia Flight Test Data," NASA Technical Memorandum 87768, August 1986.

³Robert Blanchard, Kevin Larman, Christina Moats, "Rarefied-Flow Shuttle Aerodynamics Flight Model," NASA Technical Memorandum 107698, February 1993.

⁴Robert Day, "Coupling Dynamics in Aircraft: A Historical Perspective," NASA Special Publication 532, 1997.

⁵Orbiter Aerodynamic Databook, STS85-0118, Volumes 1, 2, and 5, August 2001, Volume 3, February 1996, Volume 4, January 1994, Volume 6, December 2000.

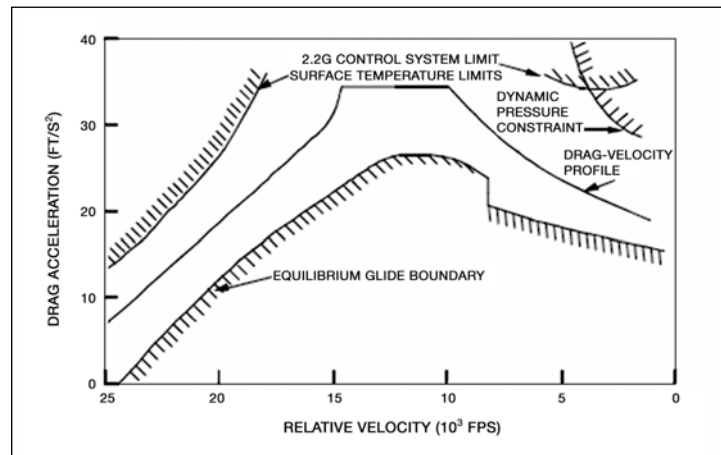


Figure 2.1-4. Entry guidance drag-velocity profile and limits.⁶

Existing orbiter aerodynamic data were used to estimate the ballistic number for the first phase. This phase of the trajectory was the “Nominal Orbiter Phase” with an intact, controlled orbiter ballistic number of 108 pounds per square foot (psf). This reflected conditions when signal was lost at Greenwich Mean Time (GMT) 13:59:32.

At some point after LOS, the orbiter lost attitude control. The degradation of the left wing appeared to be the most obvious cause. The Integrated Entry Environment Team pursued a more detailed investigation.

As mentioned above, the drag-velocity profile is controlled by the orbiter’s angle of attack and bank angle. Increasing the bank angle increases the drag slowly, while increasing the angle of attack increases the drag quickly. When the reference drag profile computed by the on-board guidance is below the equilibrium glide boundary, a “ROLL REF” alarm is annunciated to the crew. During STS-107, this alarm was annunciated at GMT 13:59:46, only 9 seconds after the LOS.

To determine which parameter (bank angle or angle of attack) caused the ROLL REF alarm, the Integrated Entry Environment Team ran simulations varying each parameter.⁷ The thermal degradation was causing increased drag on the left wing, which would induce increasing yaw and/or roll. However, the parameters driving the ROLL REF message proved to be much more sensitive to angle-of-attack deviations than bank angle deviations. Since LOS was at GMT 13:59:37, only 9 seconds passed before the message was annunciated. Based on these simulations, the Integrated Entry Environment Team concluded that it was most likely that a large angle-of-attack change (rather than bank angle) triggered the ROLL REF alarm, although the actual rate of change of the angle of attack could not be determined.

Reconstructed general purpose computer (RGPC) data from GMT 14:00:02.6 (referred to as RGPC-2) show all three hydraulic system pressures at zero, and the hinge moments of the aerosurfaces in the “up” position. Loss of hydraulic power would cause the pitch, roll, and yaw aerosurfaces to float. Pitch and roll RCS jets are no longer used for control at this Mach number and altitude, while yaw jets are still incorporated into control logic and could continue to provide some control in this axis.

Significantly, ground-based video shows a marked change in the appearance of the orbiter’s trail at GMT 13:59:37 (immediately after the end of the first RGPC data set, RGPC-1) (figure 2.1-5). The width of the trail increases at this time, which likely indicates a change in the orbiter’s flight condition. In addition to the change in the width of the trail, the trail appears to pulse or “corkscrew” over a period of less than 1 second. It is possible that a large debris event (such as loss of a major portion of the wing) may have caused

⁶Space Shuttle Orbiter Operational Level C Functional Subsystem Software Requirements; Guidance, Navigation and Control; Part A; Entry Through Landing Guidance.

⁷EG-DIV-08-32 – Integrated Entry Team Report Appendix G - Post-LOS Analysis.

the LOC. However, the debris event closest to the LOS that was apparent in the video occurred 2 seconds, or more than 60 frames (figure 2.1-6), after the change in the trail's appearance. This suggests that it was subsequent to the LOC and was not the cause. Video time errors are up to 1 second, but the relative sequence of the events (brightening, followed by a debris event) is not changed.



Figure 2.1-5. Noticeable change in brightness at GMT 13:59:37±1 second.

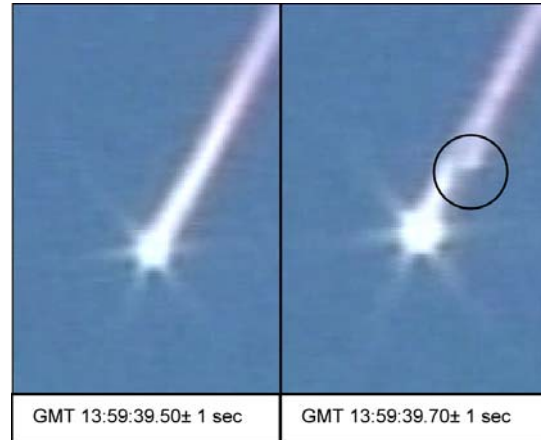


Figure 2.1-6. Noticeable debris shedding event (circled at right) at GMT 13:59:39±1 second.

It was concluded that the most credible scenario for LOC was the loss of all hydraulic systems, causing the aerosurfaces to float and resulting in an uncontrolled pitch-up. Since the left wing contains locations where all three hydraulic systems have lines that are in close proximity (including the left gear well), it is probable that the loss of hydraulics was due to thermal damage as a result of the breach in the wing. Consequently, the SCSIT defined the vehicle LOC to begin at GMT 13:59:37, immediately after the LOS, when it was determined by inference that hydraulic power to the aerosurfaces was lost. Prior to this time, *Columbia's* DAP was still in control of the orbiter. The FCS was commanding the elevons and the RCS yaw jets to counteract the increasing drag on the damaged left wing. The LOC marks the time when the *ability* to control the vehicle was lost, not when *Columbia* departed known attitudes (which occurred shortly thereafter).

Separation of redundant features is an important element in survivability design.⁸ It should be noted, however, that with the RCS jets continually firing, propellant would have been rapidly exhausted, causing an inevitable LOC regardless of the condition of the hydraulic systems.

Conclusion L3-1. Complete loss of hydraulic pressure to the aerosurfaces resulting from the breach in the left wing was the probable proximal cause for the vehicle loss of control.

Recommendation L3-2. Future vehicles should be designed with a separation of critical functions to the maximum extent possible and robust protection for individual functional components when separation is not practical.

Figure 2.1-7 shows the increasing angle-of-attack simulation. The figure shows the orbiter attitude at 1-second intervals, beginning at GMT 13:59:37 and ending at GMT 13:59:46. The white line in the figure is the reference trajectory.

⁸Ball, Robert E., *The Fundamentals of Aircraft Combat Survivability Analysis and Design*, Second Edition, AIAA, Reston, VA, 2003 ([The AIAA Textbook](http://www.aircraft-survivability.com/pages/books_frame.html)); http://www.aircraft-survivability.com/pages/books_frame.html.

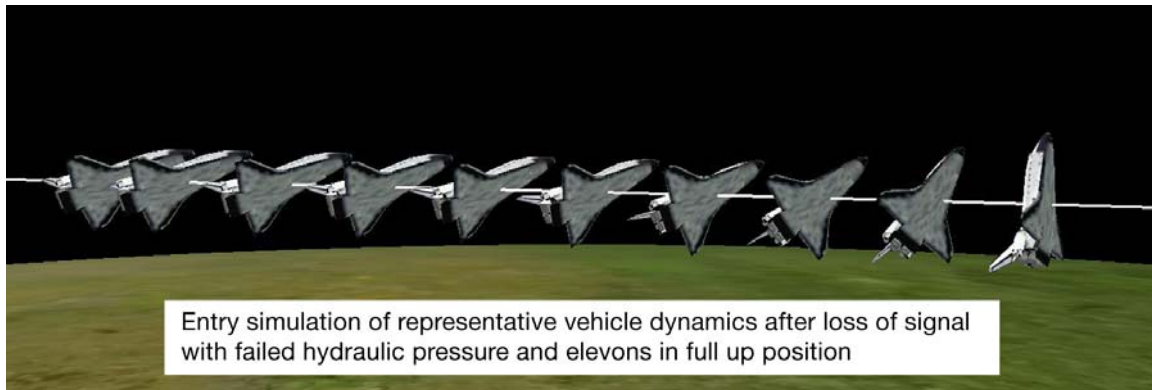


Figure 2.1-7. Sequence (1-second intervals) showing a simulation of orbiter loss of control pitch-up from GMT 13:59:37 to GMT 13:59:46. White line indicates vehicle trajectory relative to the ground.

Following LOC, the ability of the orbiter to generate lift was greatly reduced due to the uncontrolled changes in attitude. These changes in attitude also affected ballistic number, which is dependent on the cross-section of an object presented to the drag vector. Consequently, the ballistic number for the orbiter after LOC had to be estimated. This estimate was obtained by averaging ballistic numbers from a variety of attitudes.

The periodic loss of structure as the orbiter shed debris also affected the mass properties and the cross-section of the orbiter. Debris shedding events were not understood enough to model, so for the purposes of this assessment mass properties were held constant.

This second phase of the trajectory was termed the “High Drag Orbiter Phase.” The average ballistic number for the conditions between LOC and the last available GPC data (start of RGPC- 2, GMT 14:00:02.6) was estimated to be 41.7 psf. The motion of the orbiter was assumed to be benign enough that some lift was still generated, and this lift was incorporated into the trajectory. The drop in ballistic number as the orbiter changed attitude from the nominal orbiter ballistic number of 108 psf to a high drag condition of 41.7 psf would increase the deceleration of the orbiter from the nominal deceleration profile.

At the beginning of RGPC-2 and before the CE (orbiter breakup), the average ballistic number for this phase was still estimated to be 41.7 psf. However, the orbiter was assumed to be generating no lift, and only drag was incorporated into the trajectory. For this “No-lift Orbiter Phase,” it was predicted from simulations that the orbiter’s angle of attack was varying from 30 to 120 degrees and the damaged left wing was not producing lift. The angle of attack assumed for this phase of the simulation was 72 degrees because it was a mid-value angle of attack and closely corresponded with the last angle of attack data value that was recovered.

2.1.2 Forebody trajectory

The forebody trajectory analysis was initially performed by the Crew Survival Working Group (CSWG) and later updated by the SCSIT. Once again, the assumption was made that mass property changes were negligible and the ballistic number was averaged across a range of attitudes.

The “Forebody Phase” begins at GMT 14:00:23, which was an early assessment time of orbiter breakup during the initial investigation. The average ballistic number of 150 psf for the detached forebody was estimated by Johnson Space Center (JSC) Engineering immediately after the *Columbia* accident. This estimate was used in a ballistic analysis to generate debris search areas. This analysis was provided to the *Columbia* Accident Investigation Board (CAIB) and published in the CAIB Report.

Using more detailed information from ground-based video, the Image Science and Analysis Group (ISAG) determined that the orbiter breakup occurred at GMT 14:00:18.3.⁹ Later, higher-fidelity mass properties of the CM based on flight data were combined with a refined estimate of the geometry of the forebody to provide a more precise average ballistic number of 122 psf. Because ballistic analysis on many objects had already been conducted using the 150-psf reference trajectory, it was preferable not to change to the updated CE time and 122-psf reference trajectory for the additional ballistic analyses. A sensitivity study was conducted to determine how changing the reference trajectory average ballistic number from 150 psf to 122 psf would affect the release times. It was found that the release times only changed by 1 second. Since the overall error in ballistic release times was ± 5 seconds, this is not significant. Therefore, the original 150-psf forebody reference trajectory was used for the additional ballistic analyses. Figure 2.1-8 shows the two forebody reference trajectories. The dotted lines are the 122-psf trajectory parameters and the solid lines are the 150-psf trajectory parameters for an idealized forebody trajectory. The plot shows the differences in the CE times, loads, heat rates, altitudes, and equivalent velocity between the two trajectories. The trajectories were propagated out even past the CMCE, the time at which the forebody broke up, to enhance the evaluation of the differences.

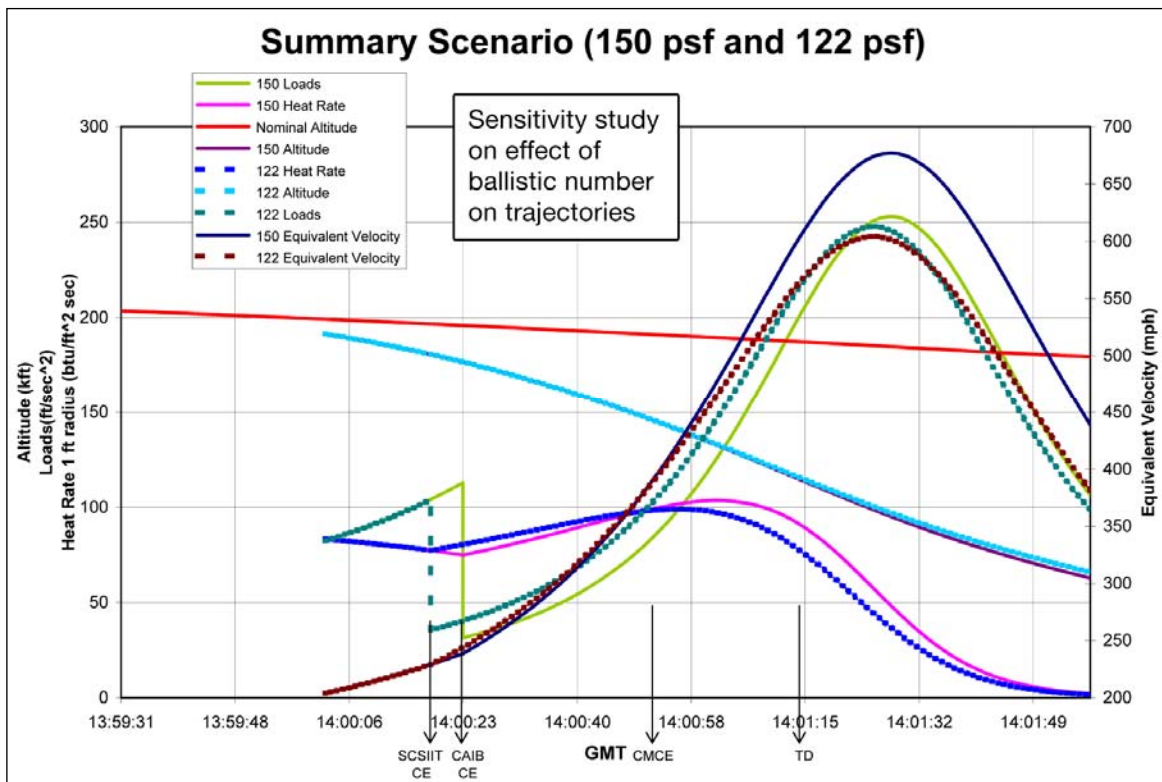


Figure 2.1-8. Comparison of 150-pounds-per-square-foot and 122-pounds-per-square-foot forebody projected trajectories.

The significance of this sudden change in ballistic number can also be seen in figure 2.1-8. As the ballistic number went from 41.7 psf to 150 psf, the deceleration dropped from approximately 3.3 G to approximately 1 G as experienced by the forebody. Figure 2.1-9 shows a more expanded view of this change in deceleration.

⁹Columbia Accident Investigation Board Report, Volume III, Appendix E.2, STS-107 Image Analysis Team Final Report, October 2003.

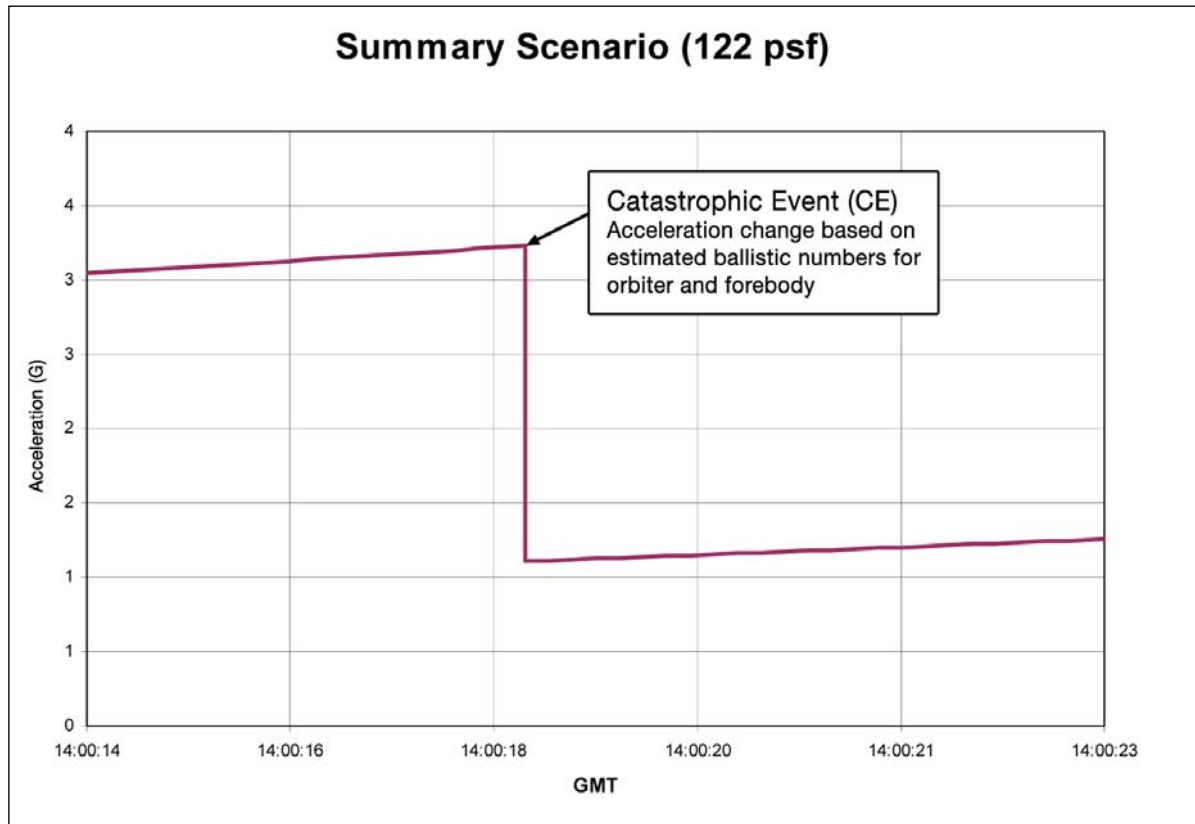


Figure 2.1-9. Estimated change in total G experienced by the forebody due to a change in ballistic number from the orbiter breakup.

In summary, the reference trajectory is divided into the following four phases:

1. “Nominal Orbiter Phase,” with an average ballistic number of 108 psf and aerodynamic data recovered from the vehicle. This phase starts 10 seconds before entry interface at 400,000 feet and lasts until LOC (GMT 13:43:59 to GMT 13:59:37).
2. “High Drag Orbiter Phase,” with an average ballistic number of 41.7 psf and incorporating some lift generation. This phase starts at LOC and lasts until the beginning of RGPC-2 (GMT 13:59:37 to GMT 14:00:02).
3. “No-lift Orbiter Phase,” with an average ballistic number of 41.7 psf and no lift generation (72-degree angle of attack assumed). This phase begins at the start of RGPC-2 and ends shortly after the beginning of the orbiter breakup at the CE (GMT 14:00:02 to GMT 14:00:23).
4. “Forebody Phase,” with an average ballistic number of 150 psf. This phase begins shortly after the CE and ends at the forebody breakup (GMT 14:00:23 to GMT 14:00:53).

2.1.3 Intact orbiter attitude dynamics through the Catastrophic Event

An entry simulation was developed to estimate the attitude dynamics of the orbiter and the resulting accelerations on the vehicle structure and crew from LOS to the CE. When the orbiter was designed, there were no requirements to assess catastrophic scenarios to understand how the orbiter might behave in an out-of-control scenario. Test data were available to verify aerodynamic coefficients for the orbiter in nominal

conditions, but for this investigation existing models had to be extrapolated beyond flight experience to understand the probable motion of the orbiter.

Recommendation L2-2. Prior to operational deployment of future crewed spacecraft, determine the vehicle dynamics, entry thermal and aerodynamic loads, and crew survival envelopes during a vehicle loss of control so that they may be adequately integrated into training programs.

The simulation used the vehicle’s preflight predicted mass properties. Changes in the c.g., moments of inertia, and mass due to the thermal damage were unknown and, therefore, not included. The aerodynamic characteristics determined for attitudes that were outside of the vehicle database were also based on the “undamaged” geometry. The initial conditions of the simulation were based on the downlinked GPC data at LOS including position, velocity, attitude, any alarm/warning-related data; and the recovered MADS/OEX recorder sensor data. The first set of RGPC data (RGPC-1) and the second set of RGPC data (RGPC-2) were used in an attempt to synchronize the simulation with the actual flight conditions. These RGPC data indicated that all hydraulic systems had failed by this point, which would result in the elevons free-floating, probably in the full-up position. The yaw rates during the RGPC-2 period exceeded the maximum value of the data scale (“pegged out”). All of the rates were high enough that they may have affected the inertial measurement units’ ability to maintain a reference, so the quality of acceleration, rate, or attitude data is unclear. However, the period of excessive rates was relatively short and it was the only data available. The MADS/OEX recorder pressure data from the lower right wing surface pressure transducers indicate large oscillations in the angle of attack 5 seconds after LOS. These MADS/OEX recorder pressure data were matched to the simulation and showed good agreement in terms of rates and attitude excursions. Even though this entry simulation used all the available data, damage to the wing and aerodynamic properties outside the database of experience could not be accounted for in this analysis. However, the results are representative of the attitudes, rates, and characteristic motion the vehicle probably experienced.

Figures 2.1-10 through 2.1-12 show the plots of the estimated orbiter angle of attack, roll angle, and sideslip angle from the start of the LOC period until the CE based on the simulation. The representative motion seen in these plots shows that the orbiter was oscillating around the velocity vector in all three axes.

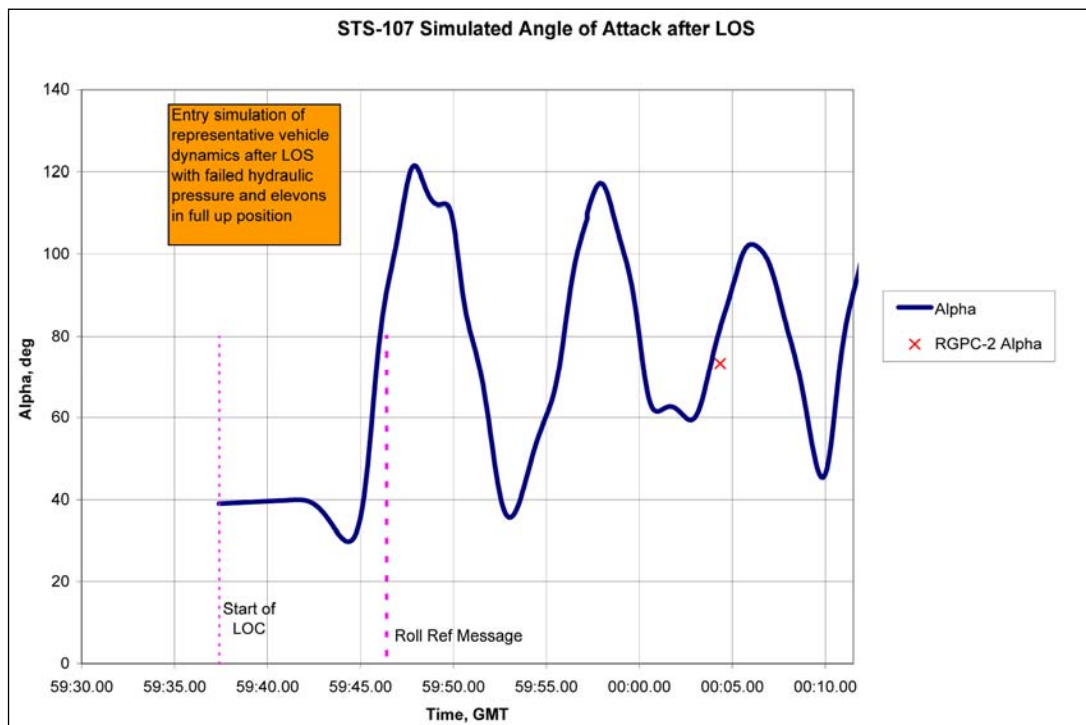


Figure 2.1-10. STS-107 simulated angle of attack after loss of signal. Red data indicate alpha condition recorded in the reconstructed general purpose computer-2 data.

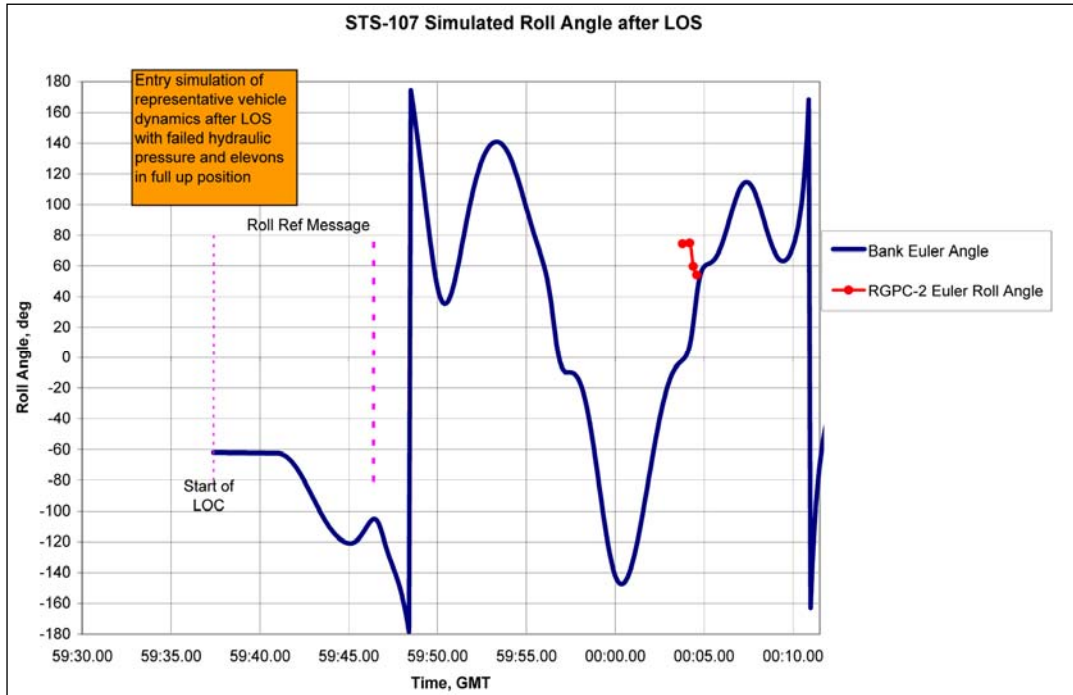


Figure 2.1-11. STS-107 simulated roll angle after loss of signal. Red data indicate roll conditions recorded in the reconstructed general purpose computer-2 data.

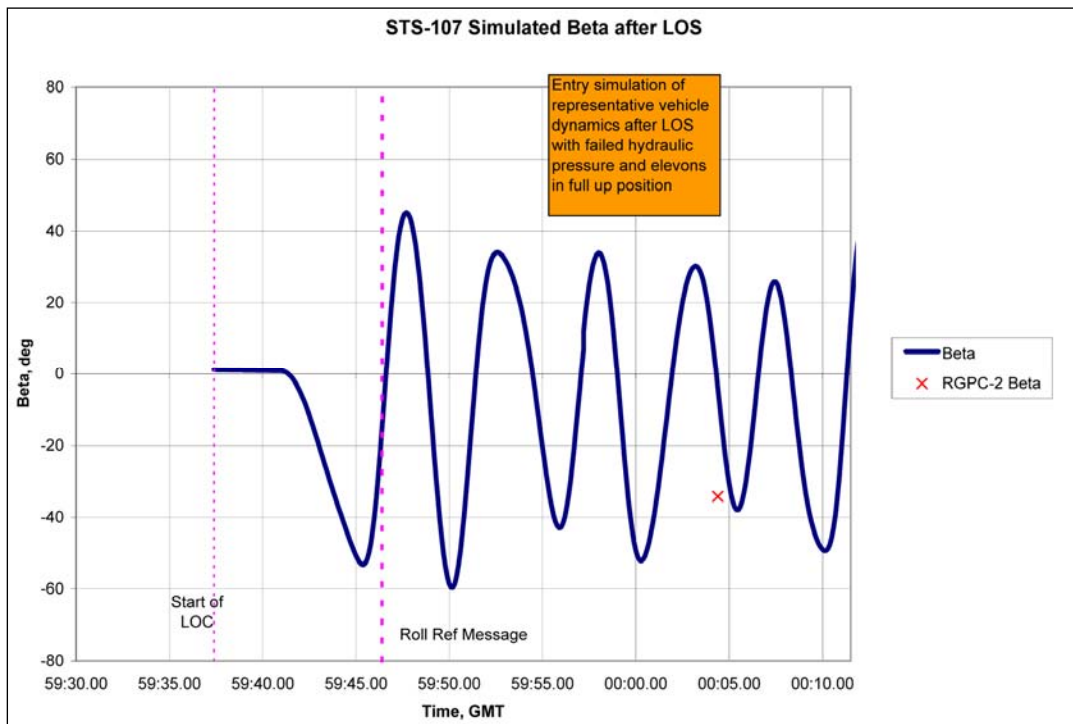


Figure 2.1-12. STS-107 simulated sideslip angle after loss of signal. Red data indicate beta condition recorded in the reconstructed general purpose computer-2 data.

Figure 2.1-13 is a second-by-second graphical depiction of the simulated motion of the orbiter during this period. The sequence begins at the start of the LOC period (GMT 13:59:37) and ends at the CE (GMT 14:00:18). The view is from a point in front of the orbiter’s direction of travel, looking backward along the velocity vector. The snapshot for GMT 14:00:04 shows the left wing departing intact. In reality, the left wing did not come off all at one time but was shedding debris over a period of time.



Figure 2.1-13. Entry simulation snapshot sequence. Times are in Greenwich Mean Time.

With the sequence viewed from a vantage point looking back up the velocity vector, it is apparent that the predominant orientation of the orbiter remained “belly into the wind” with large excursions in pitch, roll, and yaw. This motion can be characterized¹⁰ as a slow (30 to 40 degrees per second), highly oscillatory spin. As the simulation progresses in time, the rates and attitude excursions increase.

The entry simulation combined with trajectory data yielded the accelerations at the orbiter center of mass, the CM center of mass, and the x-links.¹¹ The total acceleration consists of the translational acceleration due to drag plus the rotational acceleration due to the rotation of the orbiter. The magnitude of the rotational acceleration is dependent on the distance from the center of rotation, and the direction of the load is always away from the center of rotation. The translational acceleration is always along the velocity vector as the orbiter decelerates due to aerodynamic drag. However, as the orbiter rotated, the direction of this deceleration load rotated with respect to the orbiter body axes. Sometimes the translational and rotational accelerations add together, other times they subtract from one another. The addition or subtraction of the translational and rotational accelerations depends upon the orientation of the orbiter at that particular time. Figures 2.1-14 and 2.1-15 show this concept.

Figure 2.1-14. Representation of resultant body axis loads imparted from aerodynamic drag in nominal entry attitude.

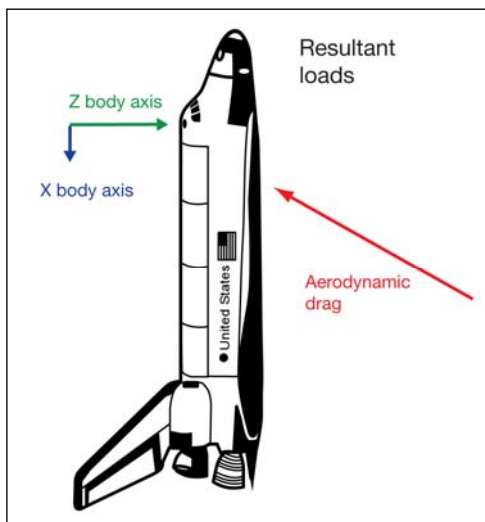
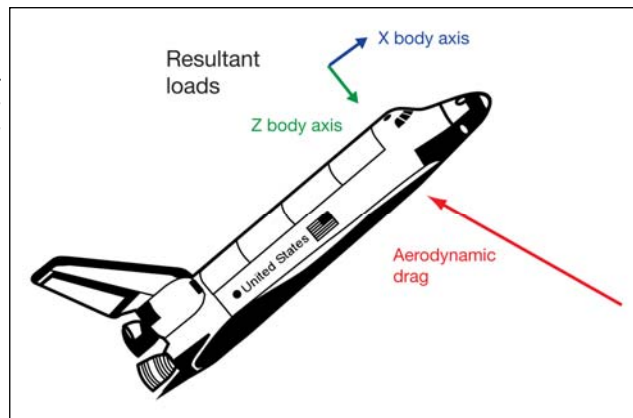


Figure 2.1-15. Representation of change in resultant body axis loads imparted from aerodynamic drag in off-nominal attitude.

¹⁰Flight Test Demonstration Requirements for Departure Resistance and Post-Departure Characteristics of Piloted Airplanes, Air Force MIL-F-83691B, Change 1, 5/31/96.

¹¹The x-links connect the crew module to the forward fuselage at the X₀ 582 ring frame bulkhead.

The accelerations are shown in figures 2.1-16 through 2.1-18. These figures show the accelerations due to rotational motion of the orbiter plus the translational accelerations due to atmospheric drag. There is one figure for each orbiter axis, and each figure shows the accelerations at the three different vehicle locations – at the orbiter center of mass, at the CM center of mass, and at the x-link location. Included in each figure is a pictorial that helps describe the effective motion of crew members that would result from these accelerations.

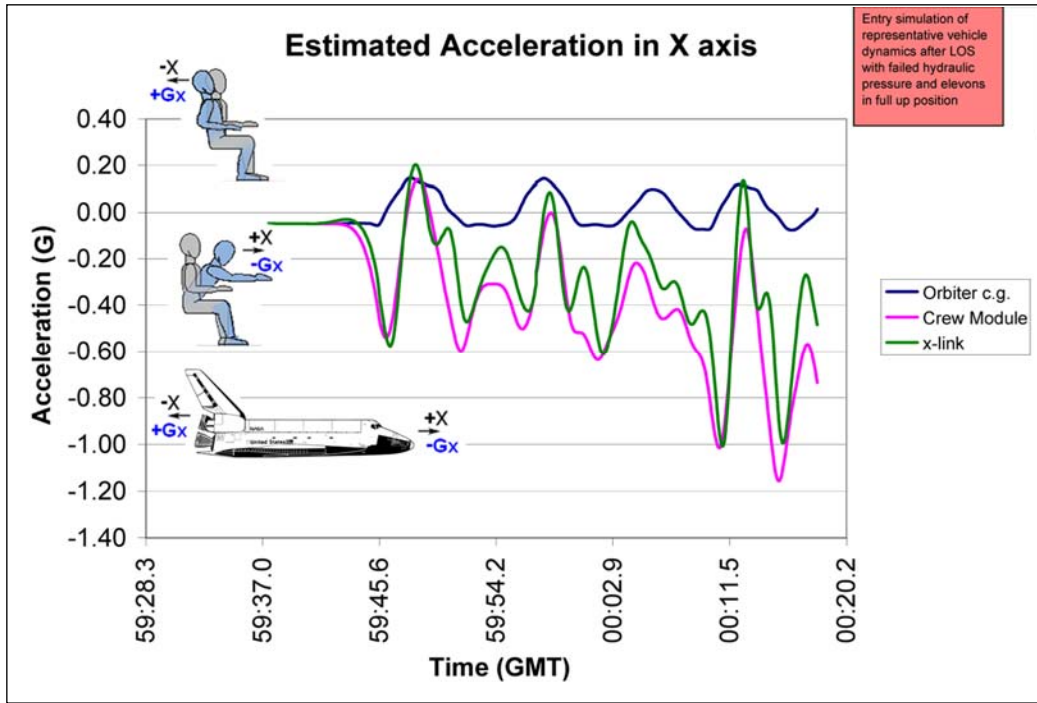


Figure 2.1-16. Estimated accelerations at the crew module in the X axis from the loss of signal to the Catastrophic Event.

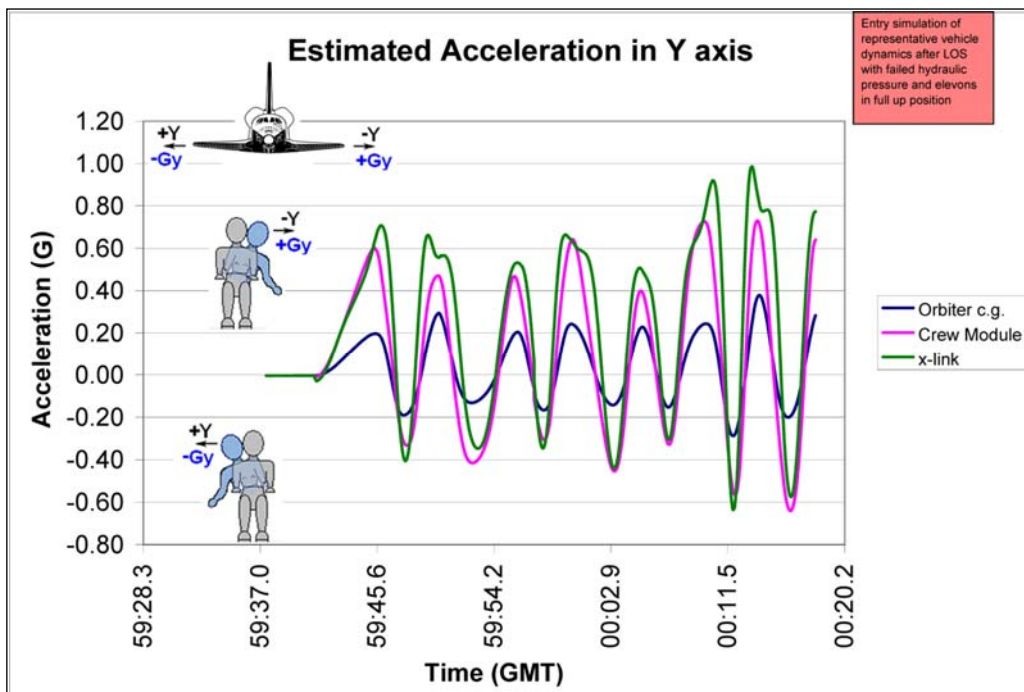


Figure 2.1-17. Estimated accelerations at the crew module in the Y axis from the loss of signal to the Catastrophic Event.

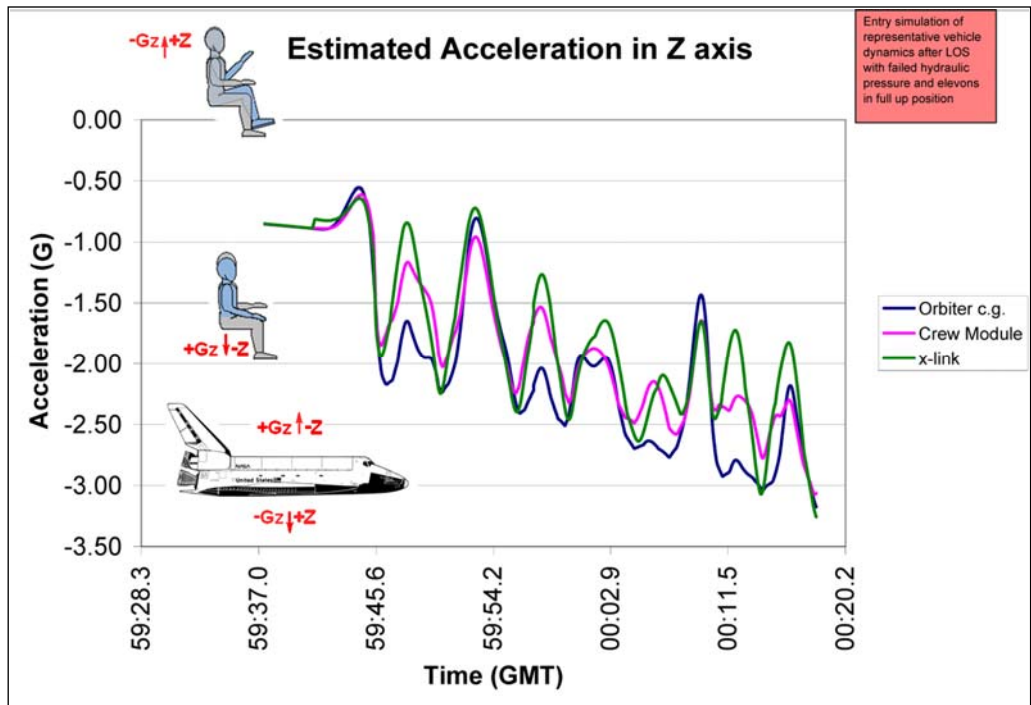


Figure 2.1-18. Estimated accelerations at the crew module in the orbiter Z axis from the loss of signal to the Catastrophic Event. [Note: Crew and orbiter Z axes have opposite convention]

As shown in the figures' pictorials, the motion experienced by the crew members inside the vehicle during the intact orbiter LOC time period is best represented by a swaying motion side-to-side, a pull forward in the seat, and a push down into the seat.

2.1.4 Post-Catastrophic Event attitude dynamics of the forebody

The SCSIT received anecdotal information that the *Challenger* CM was believed to have reached a stable attitude (“trimmed”) in a nose-into-the-wind condition. This belief was based on a video that shows a brief clear view of the CM in this orientation (figure 2.1-19), and the fact that the CM appeared to have impacted the water in a slightly nose-down condition.¹² As a result, the assumption upon which crew procedures are based (see Section 3.3) was that in an LOC/breakup scenario, the CM would trim nose-down after reaching terminal velocity. Although many types of data regarding the *Challenger* accident are available, they are almost entirely limited to information about the cause of the accident and are not related to crew survival. Relevant information was generally located by contacting personnel who worked at NASA at the time. No data could be found to support this anecdotal conclusion other than the video. Ground-based video of the forebody of *Columbia* implied that the forebody was rotating. Consequently, the SCSIT set out to assess the assumption that the *Columbia* forebody came to an aerodynamically stable attitude.

¹²Report of the Presidential Commission on the *Challenger* Accident, Volume III, Appendix O, NASA Search, Recovery and Reconstruction Task Force Team Report.



Figure 2.1-19. Video-capture showing Challenger crew module (circled in red) pointed nose into the direction of travel.

No telemetry, test data, or previous analysis existed to characterize the behavior of the CM or the forebody after separation from the rest of the orbiter. Therefore, the aerodynamic properties of the forebody had to be estimated and incorporated into an aerodynamic simulation to determine the forebody dynamics. The objective of this study was to examine the stability and possible trim attitudes of the free-flying CM and forebody [CM plus forward fuselage (FF) (figure 2.1-20)] from the CE to the CMCE. These data, when combined with the forebody trajectory aerodynamic drag data, provided the loads applied to the forebody during this phase. For simplicity, the initial conditions for altitude, velocity, and mass properties were held constant through out this 35 second period. The initial condition altitude was 176,790 feet with an initial velocity of Mach 14.4. These initial conditions were extrapolated from the last known vehicle state and projected through the simulation in the preceding section to the CE. The forebody mass properties were estimated using the evaluation of the orbiter breakup (see Section 2.2) and engineering judgment. This motion analysis was based solely on approximations and modeling. Therefore, the results should be considered indicators of general trends, and representative of the approximate accelerations and aerodynamic behavior that likely occurred.

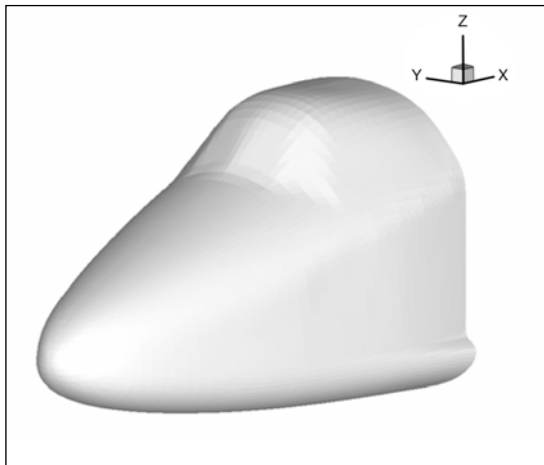


Figure 2.1-20. Forward fuselage/crew module (forebody) configuration.

Before any simulations were run, the pitch stability of the CM and the forebody was examined. This was a static, 3-axis uncoupled analysis. Plots of the pitching moment coefficient, C_m , vs. angle of attack showed two possible statically stable attitudes for the forebody at -100° and 125° angles of attack (CM stable attitudes were slightly different). Figure 2.1-21 shows the attitudes with the arrow indicating the direction of the wind.

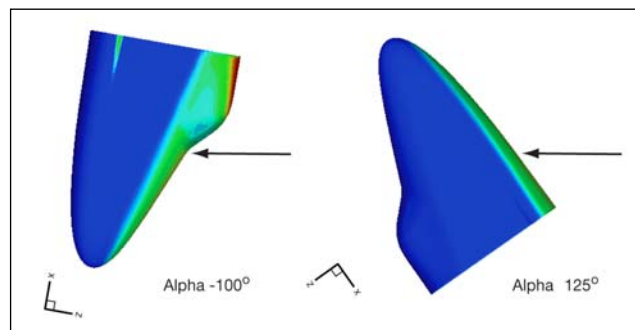


Figure 2.1-21. Pitch stable attitudes for the forebody (arrow shows direction of wind).

However, evaluation of the rolling and yawing moment coefficients, C_l and C_n showed that the statically stable attitudes in pitching moments (C_m) are not stable in either yaw or roll. Figure 2.1-22 shows the contour plot of all three moments across an alpha and a beta sweep. Locations where all three moments coincide would be stable in all three axes. Although at alpha approximately +50 degrees the moments appear very close to coinciding, close inspection showed that they do not.

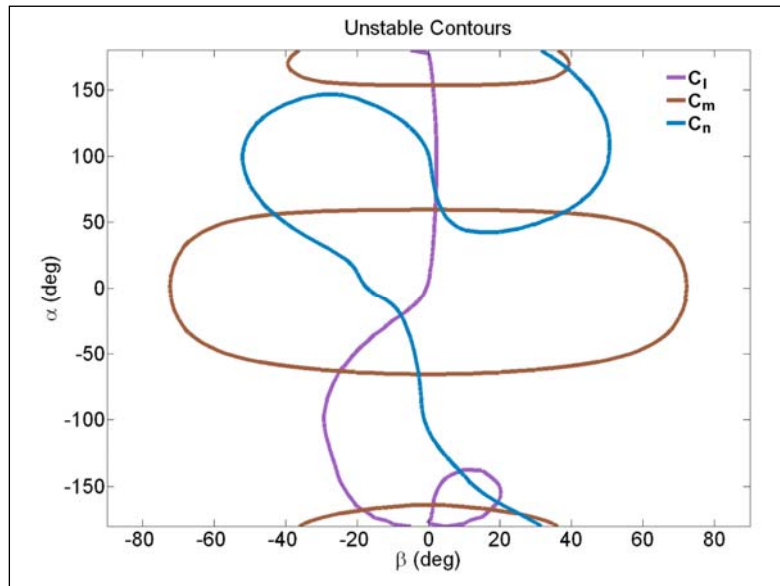


Figure 2.1-22. Contour plot of pitch, roll, and yaw moments for a crew module showing no stability due to slight offset in lateral center of gravity.

To verify this conclusion that the -100° and 125° angle-of-attack attitudes were not stable in the other axes, a forebody simulation 6-degree-of-freedom simulation was run. The initial attitude rates were zero, the initial angles of attack were set to the pitch trim points (-100° and 125°), and the sideslip angle was set to zero. In each case, after a few seconds the forebody began to rotate about the X axis with an increasing rate, and a “wobble” developed about the Y and Z axes. After evaluating the simulations, it was determined that the reason for the instability was a lateral offset of the c.g. The lateral c.g. limit for normal orbiter operations¹³ ranges from ± 1.0 in. to ± 1.5 in. maximum depending on the X_{cg} . The lateral c.g. for *Columbia*’s CM was 0.7 in. from the centerline. This is well within operating limits for the orbiter, but greater than zero.

The simulation was re-run with the lateral c.g. set to zero. Both the -100° and 125° angle-of-attack cases were stable when starting with no initial rates. However, when the simulation was initiated with any initial rate in any axis, the forebody became unstable. The forebody never reached a stable attitude when initialized in any other attitude than one of the statically stable angles of attack. Since the orbiter was rotating at the time of breakup, it is expected that the free-flying forebody would also be rotating upon separation from the orbiter. It is concluded that the *Columbia* forebody did not attain a stable attitude.

The team also assessed whether a free-flying CM (with no forward RCS compartment or gear well attached) would come to a stable attitude. This is the *Challenger* case. The analysis was performed using the same tools. The assessment showed that the CM alone would not stabilize either.

Finally, it was speculated that the trailing wires and cables from the CM or forebody may have provided some aerodynamic stability (similar to the tail on a kite). The cables were modeled as 10 stiff poles trailing behind the CM with a diameter of 1.5 in. (based on maximum wire bundle size), a length of 10 feet (figure 2.1-23),

¹³Flight and Ground System Specification, NSTS-07700, Volume X, Book I, Section 3.3.1.2.1.5 Orbiter – CG limits, November 10, 1998, p. 3-142.

and a mass of 2.43 lbs. per foot based on a bundle of 715 strands of 22-gauge wire. The resultant simulation showed no significant effect on stability for either the CM or the forebody. This is most likely because of the low mass of the cables compared to the forebody.

Modeling is subject to some inherent uncertainty regarding the actual motion dynamics. However, all analyses consistently showed a lack of stability.

Finding. The forebody and the CM of the orbiter are not aerodynamically stable in attitude with any initial rates or lateral center of gravity (c.g.) other than zero.

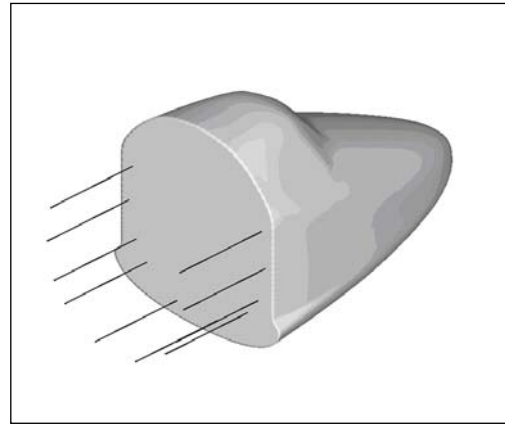


Figure 2.1-23. Modeled trailing wire configuration for forebody.

To determine the angular velocities and the accelerations at various locations in the forebody for the time period from the CE to the CMCE, two dynamic simulations were performed. Both cases used actual STS-107 c.g. conditions and an initial forebody attitude of $\alpha = 90$ degrees and $\beta = 10$ degrees. This attitude was extrapolated from the final attitude at the end of the LOC-to-CE simulation discussed earlier. Although the attitude of the forebody could be projected from the LOC simulation, the rates imparted to the forebody at the moment of separation cannot be determined. One case was run without any initial rotation rates, and one case was run with initial attitude rates. The initial attitude rates were extrapolated from the final rates from the LOC simulation and are -70 deg/sec in roll, -30 deg/sec in pitch, and 25 deg/sec in yaw. These rates assume that the forebody separated and maintained the same rates experienced by the intact orbiter at the moment of the CE. This is not likely, but the rates were assumed to be representative. Additionally, the shape of the forebody was held constant through the simulation, although it is likely that the forebody's shape and mass properties were changing due to debris shedding. The simulation is believed to address the dominant variables affecting the motion of the forebody. However, because of the many assumptions used, the simulations can only be considered representative of the type of motion that most probably occurred and not an exact determination of a specific attitude or rate at a specific time.

Figures 2.1-24 through 2.1-26 shows the forebody's angular velocity for each case.

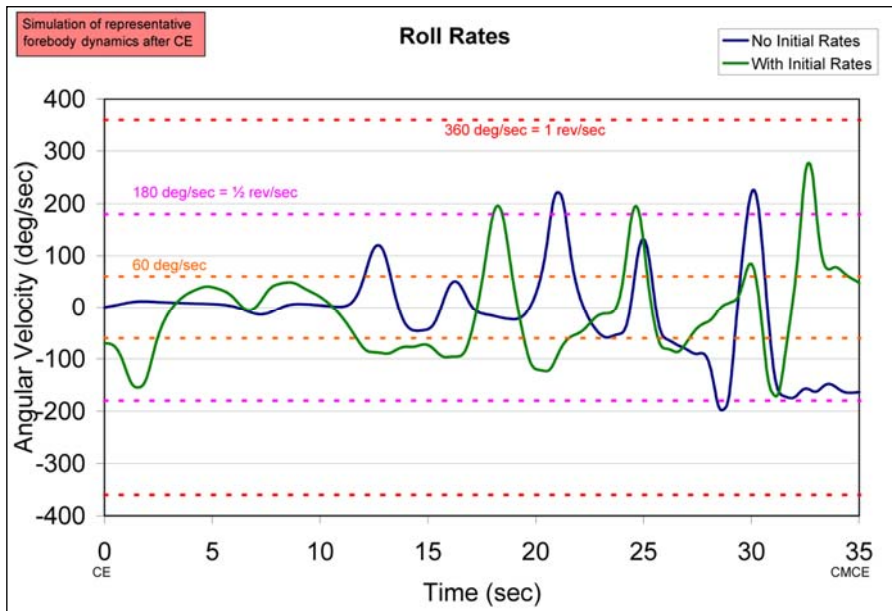


Figure 2.1-24. Free-flying forebody roll rates, with and without initial rates.

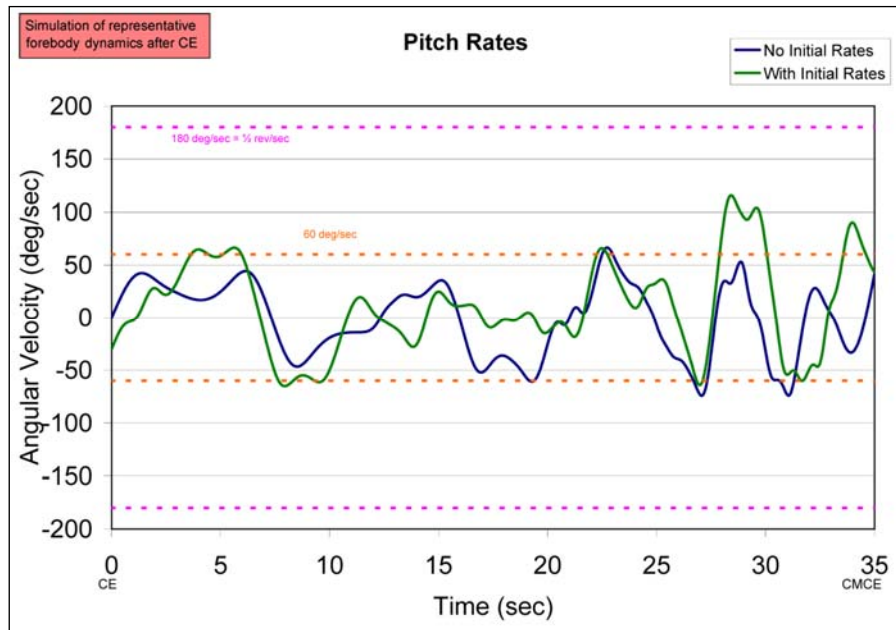


Figure 2.1-25. Free-flying forebody pitch rates, with and without initial rates.

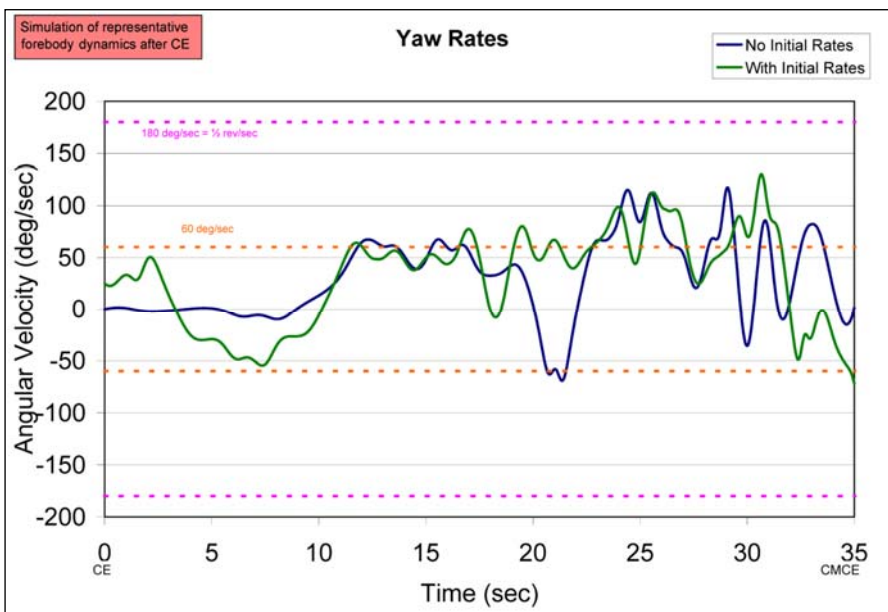


Figure 2.1-26. Free-flying forebody yaw rates, with and without initial rates.

To summarize the data shown above, the analysis shows that for the first 12 to 15 seconds of free-flying motion with no initial rates, the rotation rates remained extremely low. For the case with initial rates, they remained fairly low (<60 deg/sec, or ~0.17 rev/sec) as well. Following that period, with or without initial rates, the rotation rates climbed to as high as 0.5 rev/sec by the CMCE.

This dynamic attitude motion was combined with trajectory data in the same way as previously described for the out-of-control orbiter to determine accelerations at crew seat positions. Each seat was located at a different location from the forebody c.g., so there are slight differences for each location. Figure 2.1-27 shows a chart of the simulation accelerations from the CE to the CMCE for a representative seat position. The accelerations are given in units of G and represent *total* acceleration.

The increasing atmospheric drag experienced by the forebody is seen (figure 2.1-27) in the trend of increasing accelerations. The oscillations are due to the forebody rotation.

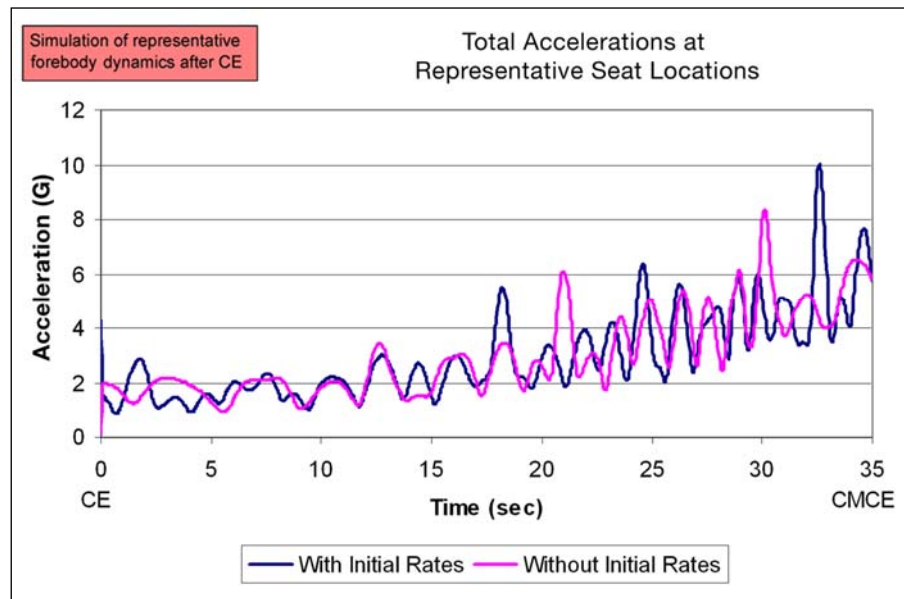


Figure 2.1-27. Accelerations at a representative seat location.

As the simulation progressed past 15 seconds, the increased rates and increasing aerodynamic drag resulted in higher accelerations at each crew position.

The conclusion of the forebody motion analysis was that the forebody was not in a stable attitude from the CE to the CMCE, but rotating about all three axes at a range from 0.1 to 0.5 rev/sec, with increasing rates and accelerations.

2.1.5 Relative motion comparison

In ground-based video of the mishap, it was noted that when the free-flying forebody could be identified, the image is periodically fluctuating in brightness. This suggested that the forebody was tumbling, which is consistent with the earlier motion analysis. It was not possible to determine the rate of rotation based on the brightening events because the forebody was irregularly shaped and rotating on more than one axis. Therefore, relative motion was selected as an alternate way of evaluating the motion of the forebody in the available video.

Relative motion analysis compares the rate of change of the movement of objects in the field of view (FOV) of a video. Rate of change can provide an estimation of relative motion experienced by the objects within a single frame of reference. Two relative motion analyses were performed. One applied to deceleration of the forebody during breakup (see Section 2.4). The other was a triangulation of relative motion of the forebody as compared to the main engines from two different ground-based videos between GMT 14:00:27.12 (9 seconds after the CE) to GMT 14:00:52.12 (just prior to the CMCE). This provided insight into the free-flying forebody motion for comparison to the aerodynamic analyses described above.

The basic assumption of the triangulation task was that the selected reference orbiter main engine had a known trajectory that was stable compared to the unknown relative position of the forebody. This is a reasonably good assumption because the engine ballistic number was quite high (> 200 psf) compared to the ballistic number of the forebody (~122 psf), and the engines were assumed to be relatively compact and

non-aerodynamic compared to the forebody. Any relative motion between the two trajectories in the video was assumed to be a result of motion of the forebody.

The orbiter engine trajectory was very well understood for several reasons. First, the impact was registered seismically, providing an exact impact time which in turn provided an excellent understanding of its ballistic trajectory. Second, the engines were visible throughout the video through separation and the end of the video, so there was positive identification of the engine. A reference trajectory for the engine was calculated with positions computed at 20-Hz intervals to provide the “known” point in the relative motion.

Two videos with known ground coordinates relative to the trajectory were selected. These videos were known as Hewitt and Mesquite (WFAA4, see Section 2.2, Table 2.2-1) based on the nearest town in Texas where they were recorded (see Section 2.2 and Chapter 4). The FOV was calculated and then trimmed and stabilized from analysis of the imagery, and details about the camera and location were provided by the original photographers. There were a few frames without the engines or the forebody in view; these were not used in the analysis.

An interactive tool was developed to solve for unknown 3-dimensional locations by using 2-dimensional image pairs. The output of this tool led to a reference-trajectory-relative, time-stamped motion path for the forebody.

Figure 2.1-28 provides a snapshot of the tool with known and unknown points selected on still images from the Hewitt and Mesquite videos. The cyan-magenta-yellow axes represent the known engine location specified in the reference trajectory. The red-green-blue axes, with red dot, depict the location of the triangulated CM.

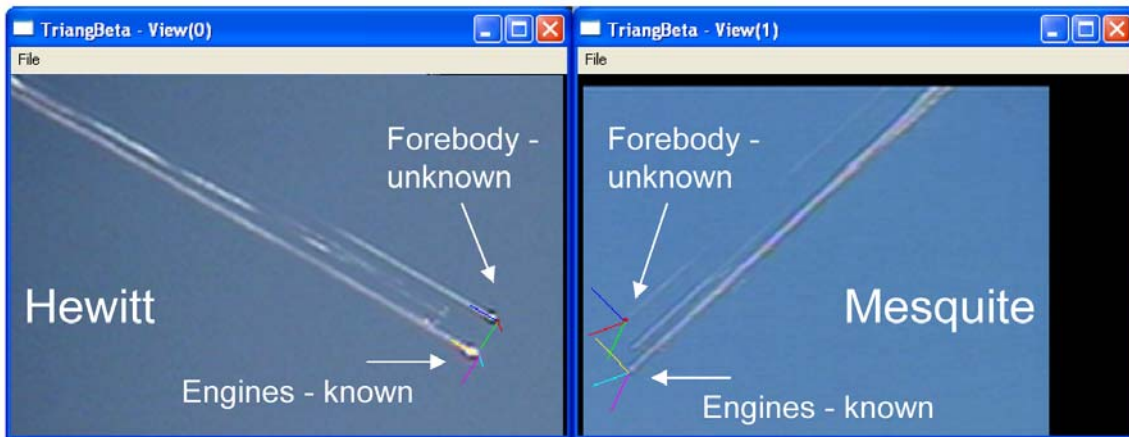


Figure 2.1-28. Depiction of the triangulation tool.

With these data, the relative motion in each axis were plotted (figure 2.1-29).

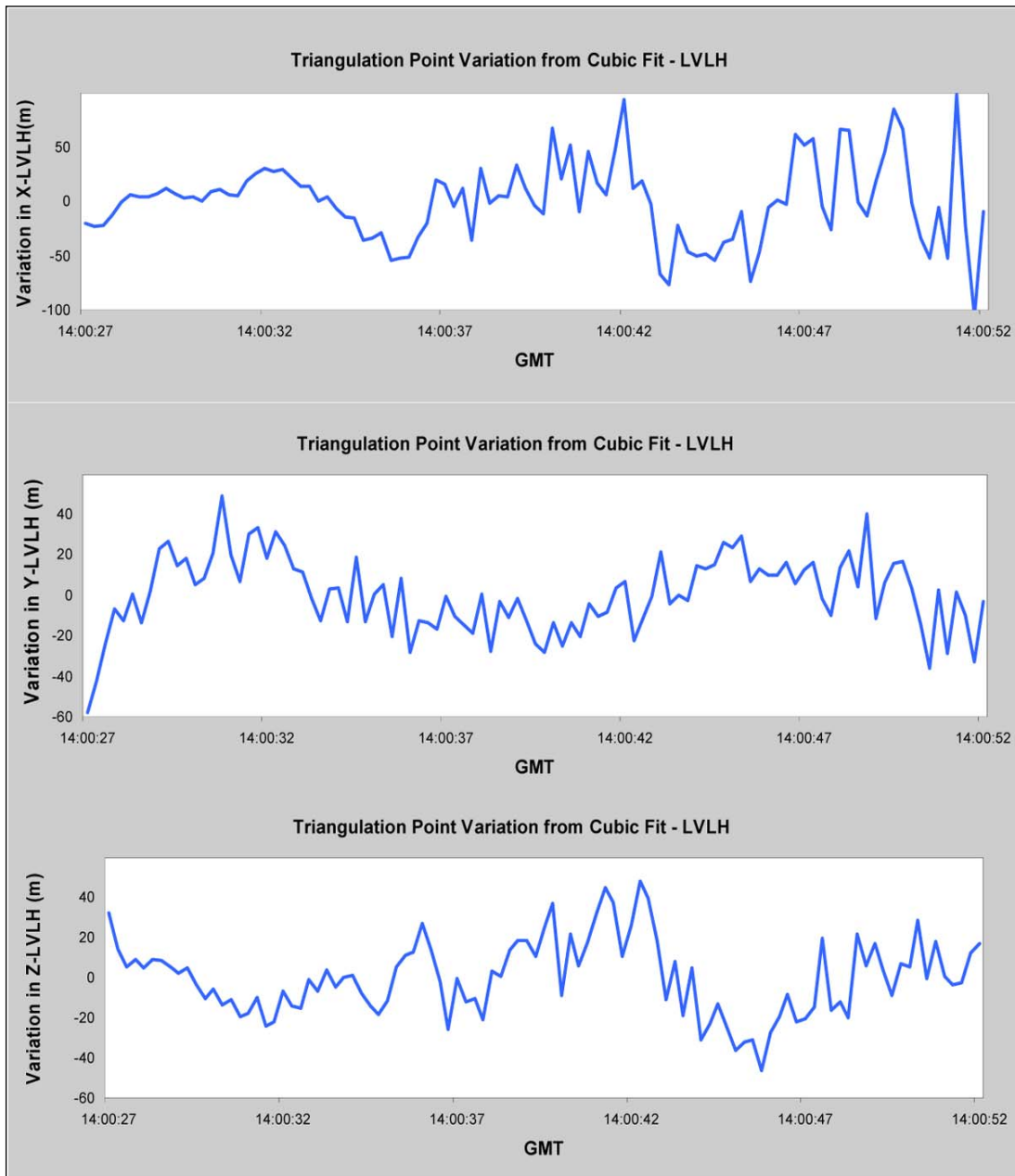


Figure 2.1-29. Relative motion between the forebody and the main engines.

These data essentially represent a wobble motion between the two objects. Since the main engines had a much higher ballistic number and a more compact shape, the wobble is assumed to be predominantly due to rotational motion of the forebody changing lift and trajectory properties slightly as the orientation to the drag vector changed.

A Fast-Fourier Transform analysis was performed on the X-, Y-, and Z-axis data to look for frequency of motion. The frequency of the wobble motion was assumed to correlate to the rotation rate in that axis (figure 2.1-30).

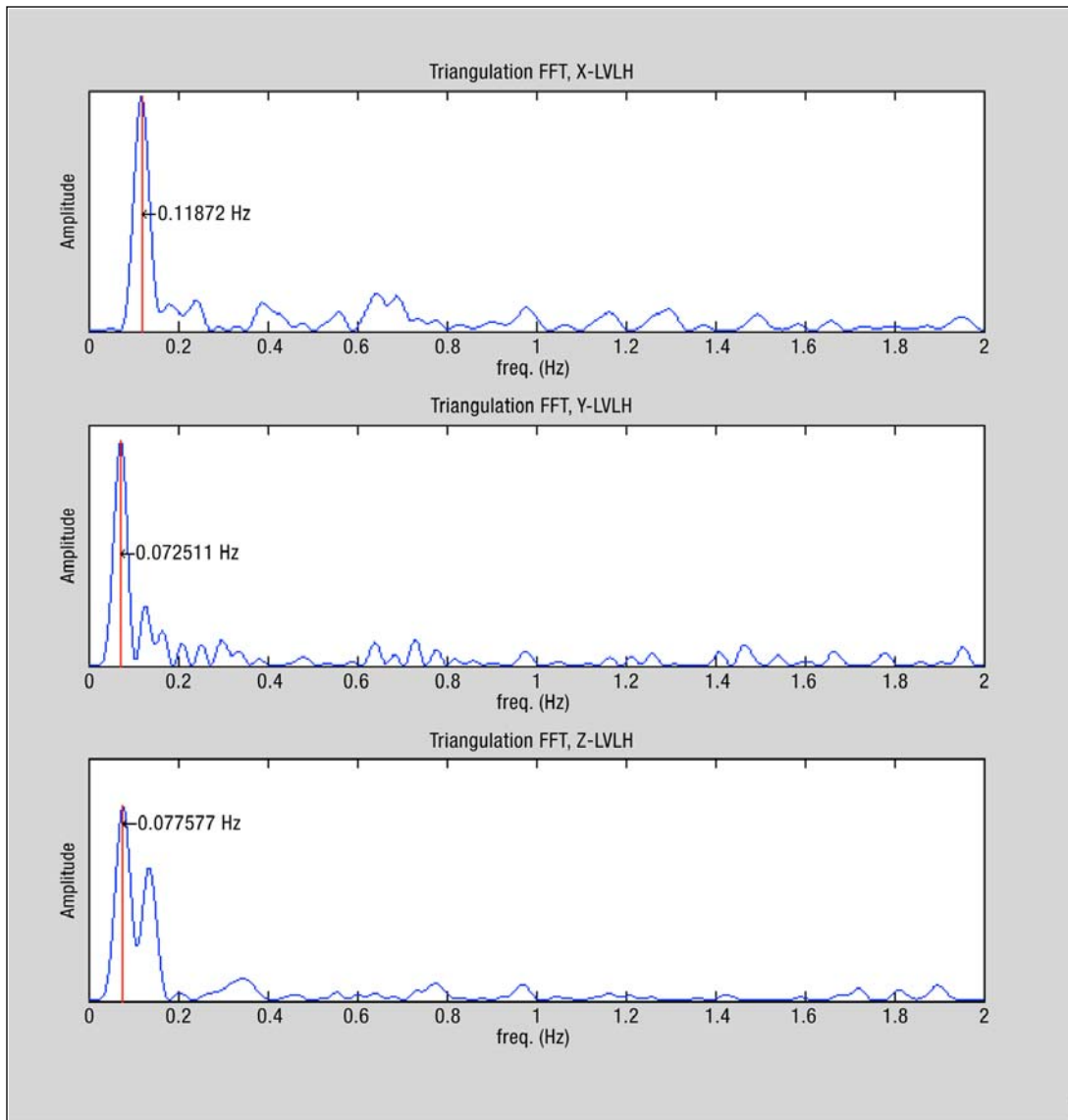


Figure 2.1-30. Fast-Fourier transform of relative motion in X, Y, and Z axes in hertz.

The results show a remarkable level of consistency in frequency of wobble motion in all three axes from approximately 0.07 to 0.12 Hz (cycles per second). This wobble cycle is assumed to reflect the rate of rotation in each axis in revolutions per second. The aerodynamic analysis predicted a rotation rate of approximately 0.1 to 0.5 rev/sec in multiple axes. The triangulation analysis thus provided support for the aerodynamic analysis in that the rotation rates are the same order of magnitude as found in the aerodynamic simulation.

Finding. Triangulation results suggest that the free-flying forebody rotated at approximately 0.1 rev/sec in a multi-axis motion.

Conclusion L2-1. Between orbiter breakup and the forebody breakup, the free-flying forebody was rotating about all three axes at approximately 0.1 rev/sec and did not trim into a specific attitude.

2.1.6 Thermal analyses introduction

Entry guidance and control is principally designed to dissipate the high energy that is associated with the orbital velocity of the vehicle, and arrive at the appropriate altitude and velocity conditions for landing, while managing vehicle heating during entry. The atmospheric entry from orbital velocities produces an extreme thermal and chemical environment. At the most fundamental level, this is due to transfer of the kinetic and potential energy of the entry vehicle into thermal and chemical energy in the atmosphere.

The Earth's atmosphere is composed primarily of molecular nitrogen (N_2) and oxygen (O_2), which comprise approximately 78% and 22% of air, respectively. At hypersonic entry speeds, a strong shock wave forms ahead of the vehicle. This shock wave compresses the ambient air to extreme pressures and temperatures. Hypersonic separation dynamics of debris and shock wave interactions at this altitude are not well understood but probably amplified the effects of entry heating.¹⁴ The temperature and pressure in the shock environment are sufficiently high that the air begins to react chemically. At orbital entry velocities, the primary chemical reactions that occur are dissociation of atoms into charged particles (plasma), dissociation of molecular species, and recombination of the resulting atoms. Molecular dissociation occurs when molecules separate into their constituent atomic species ($O_2 \rightarrow O+O$, $N_2 \rightarrow N+N$). Further, monatomic O and N may then combine to form nitric oxide ($N + O \rightarrow NO$). The amount of dissociation is a function of the vehicle's kinetic energy and the strength of the molecular bonds. Dissociation of atoms in charged particles (plasma) also occurs, but is reduced with altitude and Mach number. For the conditions of the *Columbia* mishap, plasma effects were not considered significant. For the case of the space shuttle orbiter at peak heating conditions, essentially all of the molecular O_2 and approximately 50% of the molecular N_2 are dissociated into atomic O and N in the region immediately behind the shock wave.

While the ambient atmosphere is composed of molecular N_2 and O_2 that may be quite cold, the flowfield around the entry vehicle is composed primarily of reacting molecular N_2 and O_2 , monatomic N and O, and NO, all at extreme temperatures. At the vehicle surface, the extreme temperature causes conductive heat transfer, a process in which thermal energy is conducted into the vehicle surface from the adjacent hot gas. Further, the presence of dissociated N and O atoms allows for two other heat transfer mechanisms – catalytic heating and oxidation heating. Both of these processes occur when exothermic reactions (atomic recombination and oxidization, respectively) occur at the vehicle surface. The thermal protection materials used on the orbiter are designed specifically to minimize the influence of these two phenomena and the conduction of the high temperatures into the vehicle's structure.

The efficiency by which energy is transferred from the hot, chemically-reactive shock layer gas into the vehicle is called the heat transfer coefficient. For the trajectory conditions that the orbiter experienced just before breakup, theoretical models predict less than 5% of the energy in the flow is actually transferred into the vehicle. The remainder of the energy is left in chemical and thermal modes in the wake of the vehicle. However, at off-design conditions (e.g., vehicle damage or off-nominal flight attitudes), substantially higher heat transfer coefficient values are possible, resulting in much higher energy (or heat) transfer into the vehicle.

In a nominal orbiter entry trajectory, the heating rates vary with time and location on the vehicle. The highest peak heating rate of about 60 British thermal unit (Btu)/ft²-sec occurs at the wing leading edge. Shock waves forming on different parts of the orbiter can intersect creating shock-shock interactions. These shock-shock interactions influence a vehicle's aerodynamics and increase the heat transfer rate and pressure where the interaction impinges on the vehicle's surface.

A thermal analysis was performed on the CM to understand the maximum survivable altitude for an orbiter breakup. Additionally, thermal analyses were performed to compare predicted entry heating to actual debris condition for several items. The purpose of these assessments was to understand the sequence of events and help verify ballistic release times. Analyses were performed on several specific items of debris, including a

¹⁴NASA TM X-1669, "Flight Experience with Shock Impingement and Interference Heating on the X-15-2 Research Airplane," October 1968, p. 7.

helmet, boot soles, a key piece of middeck floor, a laptop computer, the MADS/OEX recorder, the attach fittings of the CM to the FF, and a payload bay door (PLBD) roller.

Object Reentry Survival Analysis Tool (ORSAT) was used for these thermal analyses. ORSAT incorporates algorithms for trajectory simulation, atmospheres, aerodynamics, aeroheating, and thermal modeling, but its strength is its capability to combine all those algorithms into a time-efficient analysis. For one analysis, the ORSAT outputs were compared to two other models, Boundary Layer Integral Matrix Procedure-Kinetic (BLIMP-K) and Systems Improved Numerical Differencing Analyzer (SINDA).

Simulation and Optimization of Rocket Trajectories (SORT) was used to model the times of release from the reference trajectory for thermal and ballistic analyses. Snewt is a computer program that uses the modified Newtonian method to compute a surface pressure distribution and various aerodynamic coefficients. This was used to predict whether a debris item would stabilize in a given attitude during entry.

For more information on ORSAT, SORT, Snewt, BLIMP-K and SINDA, see Chapter 4.

2.1.6.1 Thermal analysis – crew module

The *Columbia* accident prompted a careful look at the question: What is the highest altitude at which an orbiter breakup can occur so that a bare-metal CM can reach the ground without being compromised thermally? The LOC/Breakup Cue Card procedure for crews is based on the estimate that the CM would survive aeroheating if separation took place below 280,000 feet during ascent. This estimate was obtained by a simple thermal analysis, for ascent only, which was performed after the *Challenger* accident.¹⁵ This analysis was based on the assumption that the CM would trim nose into the velocity vector. The thermal element clearly is the most important for entry, but can also play a role on ascent depending on the altitude and speed at the time of vehicle breakup. The team wanted to verify the results of the earlier analysis and to perform an analysis for entry aeroheating.

Obviously, the maximum crew survival altitude is more than just the thermal survival of the CM. Other considerations are the structural capability of the CM to withstand dynamic loads, the crew's ability to escape, and the capability of the existing crew escape equipment (CEE). See the sidebar "Maximum Survival Altitude of the Crew Module" on the following page for a discussion of these issues.

To accomplish the thermal analysis, proper heating rates and sufficient modeling of the CM were required. The heating rates were established by modeling the trajectory of the CM after it had separated from the rest of the vehicle. The initial state vector conditions were dictated by the trajectory profile used. Initially, three trajectory profiles were defined: a typical ascent trajectory; the STS-107 predicted entry from a 39-degree inclination orbit; and a typical International Space Station (ISS) mission entry from a 51.6-deg inclination orbit. Two different inclinations were chosen for entry because entries from higher inclination orbits have higher relative velocities and hotter temperatures. However, analysis showed that there was no detectable difference in the maximum survivable thermal altitudes between the two entry trajectories. Figure 2.1-31 displays the altitude vs. velocity for each of the three trajectory profiles. By design, the ascent trajectory has much lower velocities for a given altitude than the entry trajectories.

¹⁵ES34-87-47M, Crew Escape Thermal Response Study, May 1987.

Maximum Survivable Altitude of the Crew Module

A more detailed discussion of the maximum survivable altitude of the CM must address the structural and equipment capability of the CM as well as the thermal capability. The CM is relatively strong compared to other orbiter structures as it is designed to sustain a significant delta-pressure load against the vacuum conditions in space. Segments of the CM are also designed to withstand crash-landing loads in some axes of up to 20 G. However, the design intent is to have structure absorb enough of the loads so that crew members in their seats are able to egress, not necessarily to have the CM stay structurally intact. The bottom line is that it is not possible to know for certain what load conditions the CM is truly capable of withstanding. According to an estimation of forces on the Challenger CM immediately after the explosion, the Challenger CM likely experienced 16 G to 21 G¹⁶ at orbiter breakup and yet apparently maintained integrity all the way to water impact. Deceleration load spikes in a ballistic trajectory are highly dependent on the initial condition; the lower the velocity at the breakup, the flatter the load spike will be. At higher Mach numbers (generally higher altitudes in the profile) the load spike will be quite high as the change in ballistic number is exacerbated. Since each breakup scenario and resulting trajectory loads case would be different, it can only be said that the higher the altitude, the higher the loads will be, and that based on actual circumstances it may or may not be a factor in loss of CM integrity.

Rotational forces are yet another constraint to survival. First, they can increase the overall loads that are experienced by the structure and lead to structural breakup. Additionally, they can constrain the crew from moving to the hatch for a bailout. Analysis of loads for the Columbia mishap showed that rotational loads may be quite high for an unstable, rotating CM (possibly up to 3 G at the seats farthest from the CM c.g.). While it is possible for a restrained crew member to brace and maintain consciousness, this condition would hinder and likely prevent seat egress and bailout. Rotation rate will be dependent both on the initial conditions at the breakup and on the aerodynamic conditions at breakup. In general, at higher altitudes the vehicle will behave more like a spacecraft and less like an airplane. At higher altitudes, momentum and mass properties dominate rotation rate, and rates will take longer to increase. At lower altitudes, the aerodynamic coefficients affecting stability will begin to dominate, and rotation rates can ramp up quickly. In general, the crew should not assume that rotation rates will dampen out and should make every attempt to move to the hatch as quickly as possible for egress.

The final consideration is the capacity of the suit to support egress (see Section 3.2). The advanced crew escape suit (ACES) is rated to 100,000 feet. This rating is not a performance limit, it is a certification limit. However, no ultimate determination has been made on the maximum temperature and loads at which the suit can survive. Since each bailout situation would result in a different combination of heat and total airloads, it is not possible to pinpoint a specific altitude as a limit.

¹⁶JSC 22175, STS-51L, JSC Visual Data Analysis Sub-Team Report, Appendix D9, June 1986.

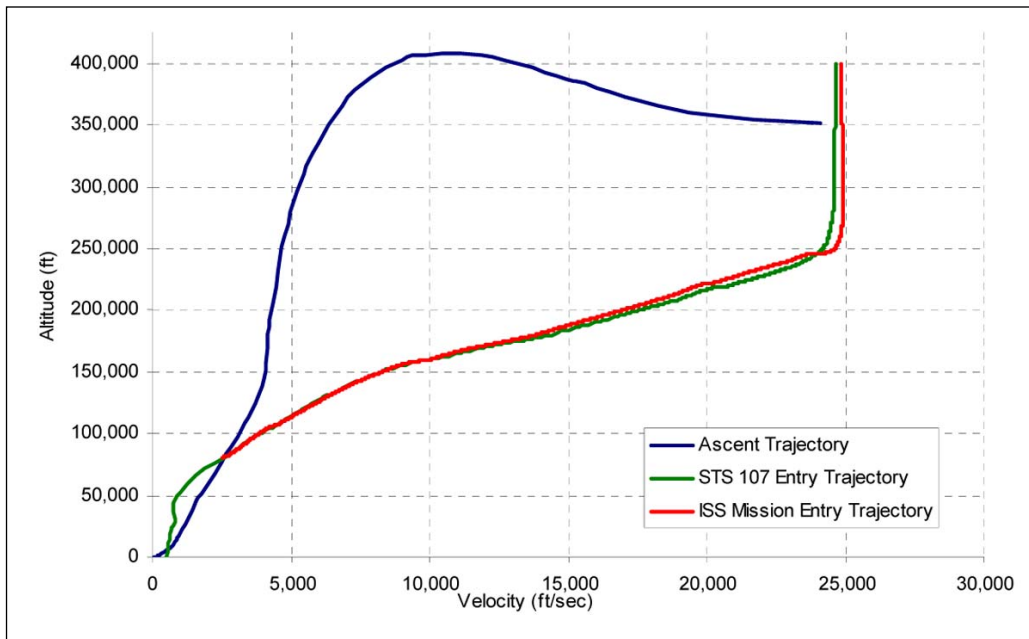


Figure 2.1-31. Altitude vs. velocity for selected trajectory profiles.

The analysis was conducted assuming that the CM was intact without any protection from the FF and accompanying Thermal Protection System (TPS). This was a conservative assessment. If the FF and accompanying TPS stays with the CM, it would provide some thermal protection for the CM. This appears to have happened for *Columbia*. However, predicting the exact level of protection provided by the TPS in various scenarios is impossible due to the infinitely variable configurations possible after a chaotic event such as a vehicle breakup. Additionally, the aft bulkhead of the CM is not protected by TPS. Overall, the assumption of no FF/TPS protection results in a conservative (worst-case) estimate of the thermal survival capability of the CM.

The orientation of the CM has a significant impact on the heating model. A stable orientation will result in a more rapid burn-through while a rotating object will distribute heat throughout the object and take longer to burn-through. The preceding motion simulations suggest a slow initial rotation with a gradual increase in rate. However, the *Challenger*-era analysis assumed a stable attitude. For the purposes of verification and comparison, both stable and rotating conditions were evaluated. The stable attitudes that were determined in the aerodynamic trim analysis were too complex to model, so the team selected two critical burn-through areas: the aft bulkhead and the forward bulkhead of the CM. These attitudes were defined as the selected bulkhead facing into the velocity vector, the worst-case thermal scenario. Because the post-*Challenger* analysis assumed a stable, nose-down attitude, the analysis assumed the forward bulkhead critical case.

The CM bulkheads have thin sections of skin supported by thicker webs. This complex geometry could not be modeled using the available thermal analysis tool (ORSAT) without substantial modification of the code. Simplifying assumptions were used to bound the problem and provide insight into relative behaviors.

This geometry has the potential for quicker burn-through due to the regions of thin skin, but it also has more mass (due to the thicker webs) that can absorb and distribute the heat away from the thin areas. It is assumed that the actual survivable altitudes would be bounded by analysis on optimistic and conservative cases. Due to these assumptions and constraints, the bulkheads were modeled as flat plates.

For the stable attitude cases, optimistic and conservative bulkhead thicknesses were used to bracket the results. For the optimistic (best-case) modeling, the thickness was established by averaging the entire mass of the bulkhead over the entire area. This optimistic approach produces a large thickness that will distribute heat better and results in higher survivable altitudes because the thicker skin takes longer to burn-through.

It should be noted that aluminum is a good conductor, and it is possible that the bulkhead area can shunt heat to the other areas of the CM, potentially making this “optimistic” estimate conservative. However, heat transport through complex shapes is poorly understood and extremely difficult to model, so it was not included in this analysis.

The conservative (worst-case) thickness for the forward bulkhead critical attitude was approximated by the thinnest portion of the bulkhead. The conservative thickness for the aft bulkhead critical attitude was more complex; it was an average of the thin skin sections of the bulkhead (not using the thickness of the webs). This approach results in lower survivable altitudes because the thinner skin will burn-through sooner. This conservative approach represents failure as a result of hole formation in the thinnest areas. This is conservative because structural failure in a thin individual location is not likely to cause total CM structural failure.

For the case of a spinning, non-stable CM, the CM was modeled as a cylinder. For this case, the skin thickness was averaged based on the mass and dimensions of the entire CM.

The next question was, at what temperature is failure expected to occur? Failure occurs as a result of both thermal and structural loads. There are three types of structural loads: translational loads from aerodynamic drag; rotational loads from vehicle rotation; and loads due to internal cabin pressure. The strength properties of aluminum (the principal structural constituent of the CM) are severely diminished as the temperature increases. Aluminum melts at about 900°F (482°C) to 1,100°F (593°C) depending on the alloy. However, at about 400°F (204°C), the strength of the aluminum begins to seriously degrade and the metal loses its ability to maintain structural integrity. Therefore, when the thermal analysis showed that the selected area on the CM reached 400°F (204°C), the CM was assumed to fail. Figure 2.1-32 shows the estimated strength vs. temperature for aluminum.

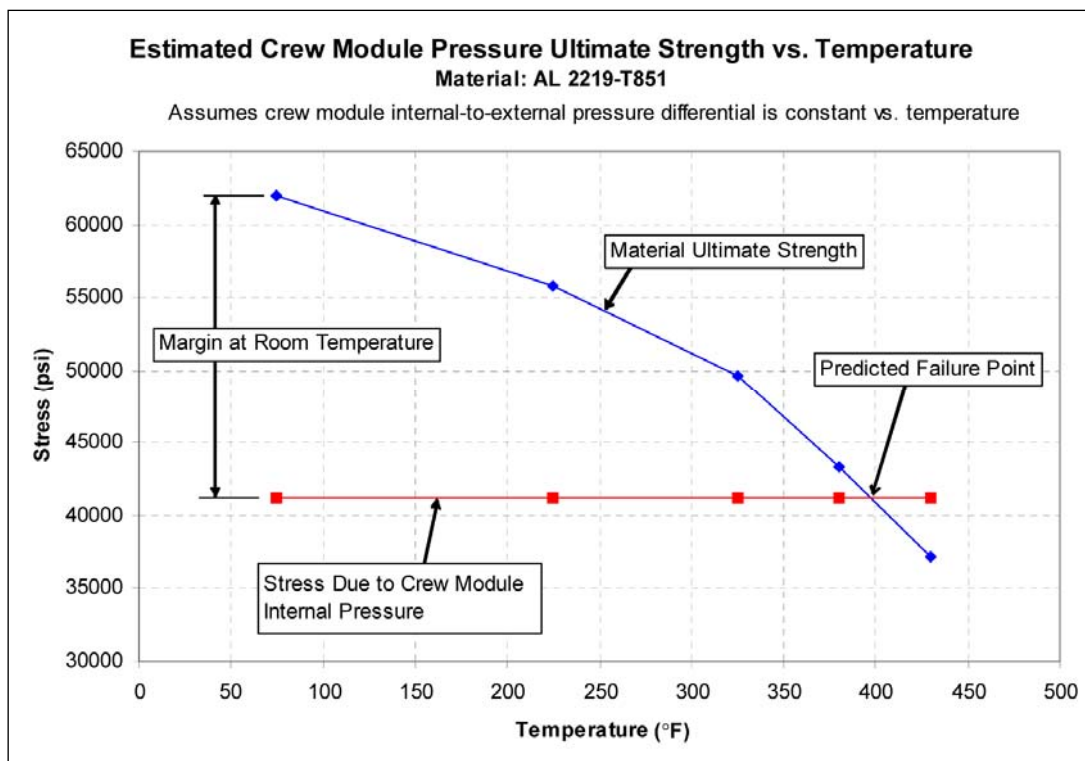


Figure 2.1-32. Crew module stress vs. temperature.

Table 2.1-1 shows the results of the analysis. The table is divided into the two different trajectory profiles: ascent and ISS mission entry. Under each trajectory is a listing of all the cases and the values for their respective ballistic number, skin thickness, and resulting maximum survivable CM altitude.

Table 2.1-1. Maximum Survivable Altitude of Crew Module

	Ballistic number (psf)	Thickness (in.)	Maximum Altitude (feet)
Ascent			
Aft bulkhead (optimistic)	88	0.34	>300,000
Aft bulkhead (conservative)	88	0.07	250,000
Fwd bulkhead (optimistic)	100	0.25	>300,000*
Fwd bulkhead (conservative)	100	0.03	120,000
Spinning	90	0.15	>300,000
ISS Mission Entry (51.6-deg inc)			
Aft bulkhead (optimistic)	88	0.34	160,000
Aft bulkhead (conservative)	88	0.07	130,000
Fwd bulkhead (optimistic)	100	0.25	140,000
Fwd bulkhead (conservative)	100	0.03	105,000
Spinning	90	0.15	150,000

*Correlates to the post-Challenger analysis case.

The analysis showed that the worst case is the forward bulkhead critical stable attitude (nose into the wind, and hole formation resulting in total structural failure). The stable attitude case was done only to compare to the earlier *Challenger* post-accident analysis, which concluded that 280,000 feet was the maximum thermal survivable altitude of the CM on ascent. However, the most relevant and realistic data come from the spinning case since the CM is not believed to have a stable aerodynamic trim condition. This analysis yielded a maximum thermal survivable breakup altitude that was greater than 300,000 feet on ascent and 150,000 feet on entry.

Finding. The estimate for maximum thermal survivability on ascent of 280,000 feet is a reasonable estimate.

Finding. The maximum thermal survivable breakup altitude for the CM on entry is approximately 150,000 feet.

As previously mentioned, this only provides the thermal element for the maximum survivable altitude for an orbiter breakup. See the sidebar, “Maximum Survival Altitude of the Crew Module,” for a more detailed discussion.

In summary, the shuttle CM could probably thermally survive a breakup up to 300,000 feet on ascent and below 150,000 feet during entry. Aerodynamic loads may cause rapid structural failure of the CM at lower altitudes. Rotational loads may prevent the crew from translating to the crew hatch. High loads may also result during crew separation if the Mach number is still high (particularly on entry). The ultimate survival limits (altitude, air speed, thermal load, etc.) of the ACES remain unknown.

Conclusion L3-3. The actual maximum survivable altitude for a breakup of the space shuttle is not known.

Recommendation L2-2. Prior to operational deployment of future crewed spacecraft, determine the vehicle dynamics, entry thermal and aerodynamic loads, and crew survival envelopes during a vehicle loss of control so that they may be adequately integrated into training programs.

2.1.6.2 Thermal analysis – helmet

A thermal analysis was performed on a helmet to compare with ballistic estimates of release time. ORSAT predicted that helmets released at GMT 14:01:03 would match the debris results when the thermal decomposition temperatures were used to assume how much of each material would remain (see Section 3.2). This coincides remarkably with the ballistic estimates from SORT, which showed helmet release times within ± 10 seconds of this time. This also coincides with the time range determined for the breakup of the forebody.

2.1.6.3 Thermal testing – boot soles

The geometry of the boot soles was too complex to model for ORSAT, especially because of the many alternatives for initial conditions. Boot soles of flight-like boots were thermally tested in an attempt to match the observed thermal damage (see Section 3.2). Test results could not be correlated directly to the debris observations, possibly because the test conditions did not sufficiently approximate the entry environment conditions.

2.1.6.4 Thermal analysis – lithium hydroxide stowage volume door

The lithium hydroxide (LiOH) stowage volume door was recovered with portions of the two seats still attached (figure 2.1-33). The LiOH door is located on the middeck floor with seats 6 and 7 attached to the door (figure 2.1-34). The condition of the door was markedly different from other segments of the middeck floor in that significant thermal erosion of the thinner areas had occurred (see Section 2.4). The hypothesis was formed that additional mass attached to this piece of debris resulted in higher heating. A thermal analysis was performed to determine whether the additional mass provided by the two seats and/or two crew members would result in the observed thermal damage.



Figure 2.1-33. Recovered lithium hydroxide door with some seat legs still attached.



Figure 2.1-34. Example of an intact lithium hydroxide door with seats 6 and 7 attached. [Crew Compartment Trainer]

Composed of aluminum 7075, the LiOH door is about 41 in. long and 28 in. wide, and has a mass of 41.6 lbs. Figures 2.1-35 and 2.1-38 show the upper surface and lower surface of the LiOH door. The thickness of the door varies and, in some cases, is as low as 0.05 in. The average thickness of the LiOH door is 0.39 in.

Photographs of the recovered LiOH door are shown in figures 2.1-36 and 2.1-38. The thermal failure corresponds to the thin sections of the door. Sections that are thicker show little or no thermal erosion. From observations of the material deposition patterns and the burn-throughs on the recovered door, the major thermal effects were directional, with flow impinging primarily on the bottom side (the side with the stiffeners). This is supported by the highly directional deposition on seats 6 and 7 (see Section 3.1).

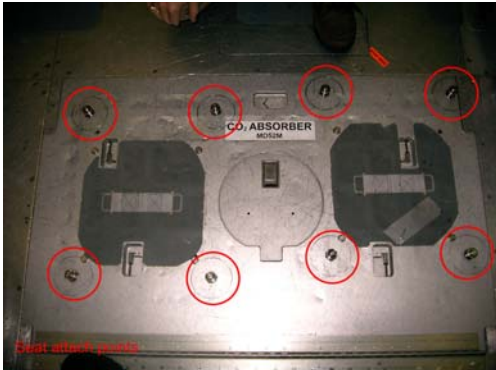


Figure 2.1-35. Upper surface of the lithium hydroxide door, facing the middeck (mockup).



Figure 2.1-36. Top surface of the recovered lithium hydroxide door, facing the middeck.



Figure 2.1-37. Lower surface of the lithium hydroxide door, facing the lower equipment bay (mockup).



Figure 2.1-38. Lower surface of the recovered lithium hydroxide door, facing the lower equipment bay.

SORT estimated that the release time occurred at GMT 14:00:59. Four configurations of the LiOH door were analyzed to capture the possible release geometries. Configuration 1 was the LiOH door re-entering by itself. Configuration 2 was the LiOH door with two empty seats attached. Configuration 3 was the LiOH door, the two seats, and a suited occupant seated in one of the seats. Configuration 4 was two suited occupants in the seats attached to the LiOH door. The possible pitch trim attitudes for these configurations were predicted using Snewt, and the results can be seen in figures 2.1-39 through 2.1-43. Untrimmed (tumbling) cases were also evaluated for each configuration to determine the sensitivity of thermal effects to attitude. All these configurations assume that the LiOH door (and the attached seats and crew members) was a single free-flying unit with no other CM structure attached.

The main difference among these configurations is the ballistic number. The ballistic number determines the trajectory, thus the velocity profile. The velocity, in turn, affects the heating rate. For objects with large ballistic numbers, the heating rate is greater than for objects with small ballistic numbers.

Since the minimum thickness of the door is 0.05 in., the door was initially modeled with this thickness to determine whether the aluminum would ablate. Ablation is defined as the amount of energy required for an object to reach its melting temperature *and* overcome its heat of fusion. An object demises when the heat of ablation has been reached; in other words, the object burns through. This is a lower threshold case than is realistic because the thicker areas of the door would act as a heat sink. If the 0.05-in. plate ablated, the thickness was increased to see at what plate thickness it would not ablate.

The door release time was also adjusted 5 and 10 seconds earlier than the estimated time predicted by SORT to see whether the release time had an impact on the results. The initial temperature in the analysis was 80°F (27°C) for all cases except one, where the initial temperature was increased to 200°F (93°C). This was done to determine the sensitivity to the initial conditions; for example, if the CM interior environment was heated significantly prior to breakup and release of the door. However, there is no evidence to suggest that this was the case.

Configuration 1 (Door alone)

The first configuration was a simple flat plate (representing the door) entering by itself. In this configuration, the door was modeled both for the tumbling case and entering normal to the flow fixed angle of attack of 90 deg (figure 2.1-39). This configuration has the smallest ballistic number, so it will receive less heat than the others. The ballistic number was 2.9 psf for the normal to flow case and 6.1 psf for the tumbling case.

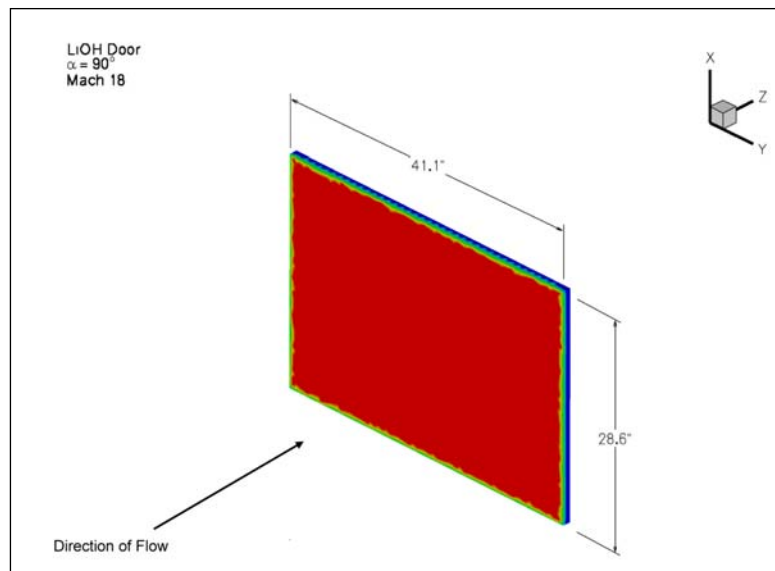


Figure 2.1-39. Aerodynamic model of the lithium hydroxide door exposed by itself at an angle of attack of 90 degrees. [Configuration 1]

For this first configuration, neither the tumbling nor the normal-to-flow case predicted that the aluminum melting temperature would be reached.

Configuration 2 (Door with two seats)

The second configuration was the door with empty seats. Since each of the seats has a mass of about 50 lbs., the total aerodynamic weight increased to 141 lbs. This includes the two seats (100 lbs.) plus the door (41 lbs.). In this configuration, the door and the seats were modeled for the tumbling case and also entering at fixed angles of attack, -92 deg or 96 deg (figures 2.1-40 and 2.1-41). This configuration has the second smallest ballistic number. The worst-case (highest) ballistic numbers for the non-tumbling and tumbling cases were 11.5 psf and 20.0 psf, respectively.

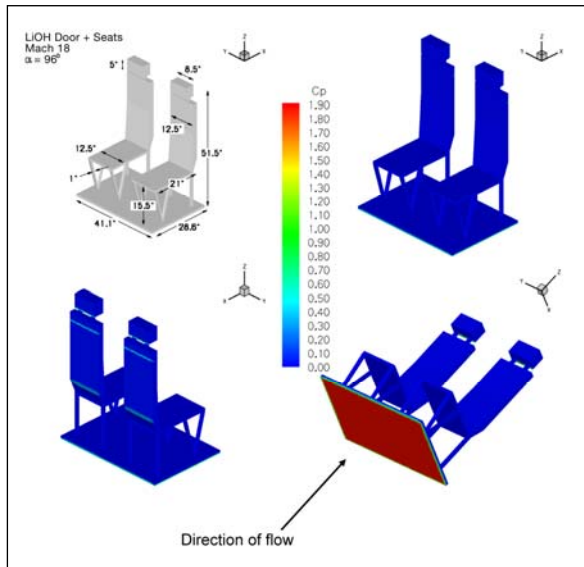


Figure 2.1-40. Pressure distribution of the lithium hydroxide door and seats at an angle of attack of 96 degrees. [Configuration 2]

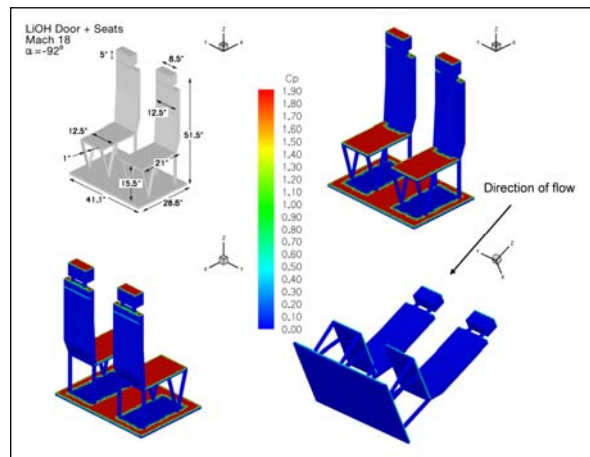


Figure 2.1-41. Pressure distribution of the lithium hydroxide door and seats at an angle of attack of -92 degrees. [Configuration 2]

The worst-case tumbling results showed that the melting temperature of the aluminum would be reached, but the estimated heating profile would not overcome the heat of fusion, so no burn-through was predicted.

is predicted to survive. Increasing the initial temperature to 200°F (93°C) for the 0.05-in.-thick plate case did not change the time predicted for the plate to demise.

The heat rates generated by ORSAT were compared to another model, BLIMP-K. The heat rates predicted by ORSAT were about 12% less than those predicted by BLIMP-K, but were generally comparable. A detailed thermal math model using the SINDA and ORSAT heating rates was constructed for a section of the door and confirmed the results predicted by the ORSAT. In this model, only the fourth configuration was predicted to demise.

For the GMT 14:00:59 estimated release time, the analysis implies the third and fourth configurations (door with one and two crew members, respectively) can produce the thermal damage observed on the recovered LiOH door. Since visual inspection of the recovered door suggests that the object was not tumbling, the stable fourth configuration is the most thermally viable solution. However, both the third and the fourth configurations are improbable because the thermal effects would have melted the seat straps and released the crew members. The surrounding debris was evaluated to determine whether the LiOH inside the compartment caught on fire. Significant portions of LiOH canisters were recovered as well as other items stored in the compartment. Both the canisters and the structures of the compartment were not seriously thermally damaged, which strongly suggests that a fire did not occur.

It is likely that the simplified nature of the assessment could not accurately model this complex object. As a result, the ORSAT analysis on the LiOH door was inconclusive.

2.1.6.5 Thermal analysis – payload and general support laptop computers

Some recovered debris items were identified as pieces from the crew’s payload and general support laptop computers, none of which were recovered intact. An analysis was performed to determine whether aerothermal heating could cause the destruction of a laptop after it was released from the CM or if it had to be pre-heated inside the CM. If the laptop had to be pre-heated, this analysis could give an indication of what the thermal environment was inside the CM before breakup.

The estimated maximum temperature from aeroheating alone was well above the temperature at which the battery will explode, likely fragmenting the laptop casing. No conclusion could be made about the thermal environment inside the CM before breakup from this analysis.

2.1.6.6 Thermal analysis – Modular Auxiliary Data System/orbiter experiment recorder

The OEX recorder, which was part of *Columbia*’s MADS, was found near Hemphill, Texas in near-perfect condition. Figure 2.1-44 shows the recovered OEX recorder. The data on the tape in this recorder were critical to the accident investigation, making the recorder one of the most important recovered items from *Columbia*.



Figure 2.1-44. Recovered orbiter experiment recorder from STS-107. [Columbia Reconstruction Database, debris item no. 54057]

Recommendation L3-3. Future spacecraft design should incorporate crashworthy, locatable data recorders for accident/incident flight reconstruction.

The rectangular shape of the box made it a good candidate for ballistic analysis providing a release time with high confidence. The box showed no signs of thermal erosion or exposure to high temperature environment. Text labels that have been imprinted on the box still remain. The data that were recovered from the recorder were recorded on magnetic tape that delaminates at 125°F (52°C). An analysis was performed to estimate the thermal damage that a free-flying OEX recorder would receive due to aerothermal heating after release from inside the CM.

The OEX recorder was located in the lower equipment bay (underneath the middeck floor) of the CM. It is loosely covered by a fiberglass shroud that channels cooler air over the recorder. The shroud is bolted over the OEX recorder but is not directly attached.

The OEX recorder case is composed of aluminum 6063. The thermal properties of aluminum 6061 were used in the analysis because the values were already in the ORSAT material database and the differences in thermal properties to aluminum 6063 were negligible. The shell thickness is 0.25 in. and the overall dimensions of the box are 19 in. long, 15.5 in. wide, and 5 in. high. The total weight of the box is 53.8 lbs.

Ballistic analysis produced an estimated release time of GMT 14:01:02. A state vector from SORT was used as a starting point in ORSAT to simulate the trajectory and heating rates of an entry from that time – altitude 131,780 feet, velocity 12,717 feet per second (fps), and flight path angle –6.3 deg. The initial temperature of the OEX recorder used was 80°F (27°C), however this may be a conservative assumption because the internal electronics of the OEX recorder cause the device to run at relatively high temperatures.

Figure 2.1-45 shows the surface temperature profile for the OEX trajectory. The surface temperature was predicted to reach 470°F (243°C). This is well below the melt temperature of the aluminum, 1,100°F (593°C). Aluminum structurally weakens at 400°F (204°C), and some deformation would be expected if the recorder achieved this temperature. However, there is no deformation of the aluminum casing.

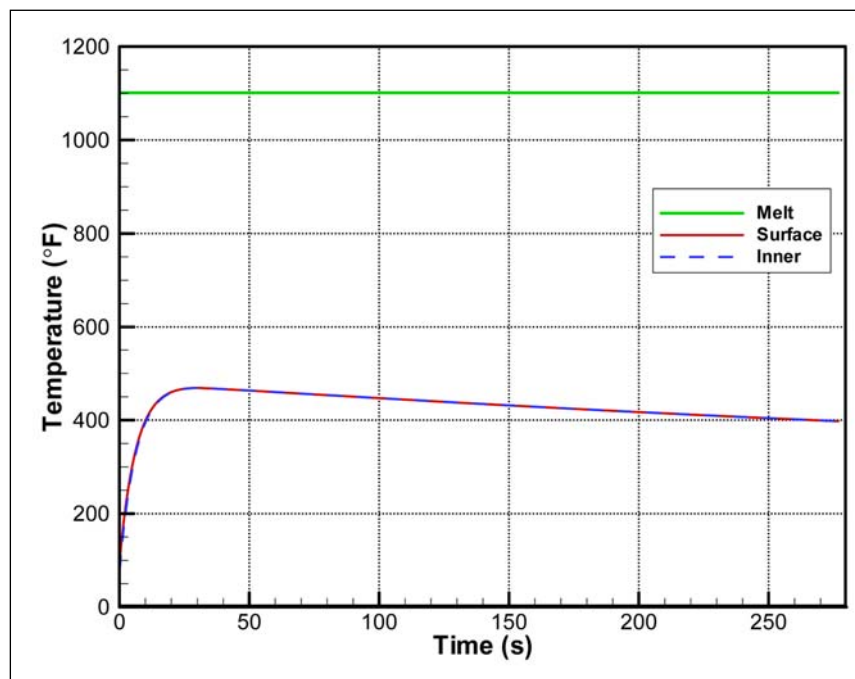


Figure 2.1-45. Temperature vs. time of the orbiter experiment recorder shell if released at GMT 14:01:02.

The lack of external thermal damage is quite noteworthy. Anodizing is still mostly present, as are the exterior labels. Exposed wires still have insulation. Finally, since aluminum is a good conductor it is expected that the internal wall temperature would have been close to the surface temperature. Since the recorder’s magnetic tape delaminates at 125°F (52°C), this also suggests that the aluminum may not have reached the predicted high temperature of 470°F (243°C).

The conclusion is that the OEX recorder was not released from the CM independently. If the temperatures reached as high as predicted, the magnetic tape would have delaminated and the casing would have likely been deformed. This analysis combined with the relatively pristine condition of the recorder seems to imply that something must have protected the recorder during entry before it was completely exposed to the aero-thermal heating environment. Ultimately, no conclusion can be made as to what ancillary structure or other mechanism protected the OEX, only that it was protected.

2.1.6.7 Thermal analysis – x-links

Examination of the recovered CM attachment fittings, known as the x-links, identified intriguing thermal damage. The two x-links attach the CM to the FF and the midbody and carry load in the orbiter X body axis (see Section 2.4 for diagrams of structure). While both x-links showed melting in the same relative locations, the starboard x-link displayed more thermal damage than the port x-link. Because the x-links are composed of Titanium 6Al-4V, which has a melt temperature of approximately 3,000°F (1,649°C), very high heating is required to create the damage that was observed on the recovered x-links. Analyses were performed to determine the thermal mechanism that could have caused this damage. Figure 2.1-46 shows a model of a pristine port and starboard x-link, while figure 2.1-47 shows the two recovered *Columbia* x-links placed side by side.

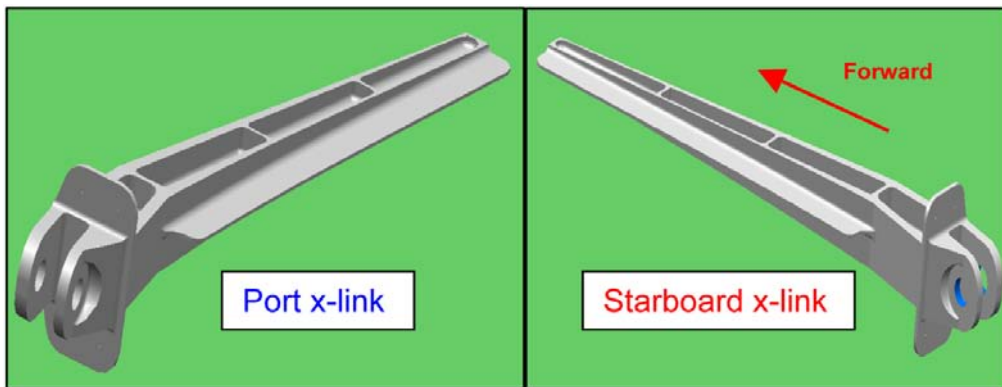


Figure 2.1-46. Drawings of pristine port and starboard x-links.

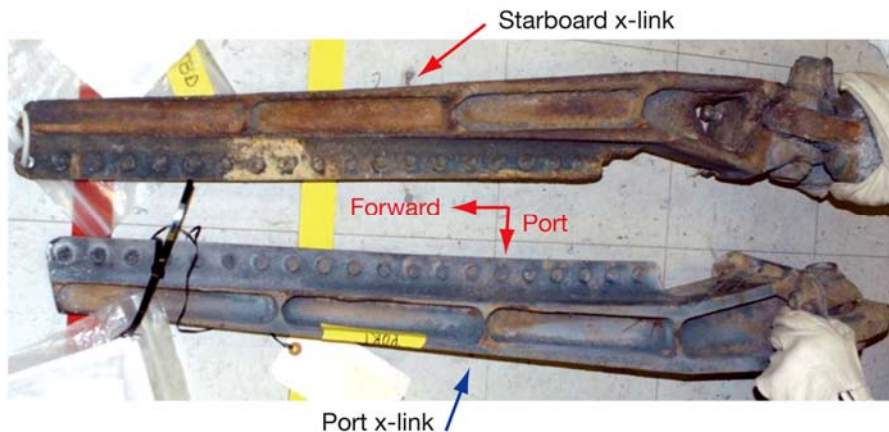


Figure 2.1-47. Comparison of port and starboard x-links recovered from Columbia. [Columbia Reconstruction Database, debris item no. 1678, and Columbia Reconstruction Database, debris item no. 1765]

The heating experienced by the starboard x-link was severe enough to melt away the top flange and to burn a hole through the 0.25-in.-thick web. Figure 2.1-48 shows another comparison of the two x-links with a better viewing angle to see the flange damage. Figure 2.1-49 shows a close-up view of the starboard x-link where a hole has been melted through the web.

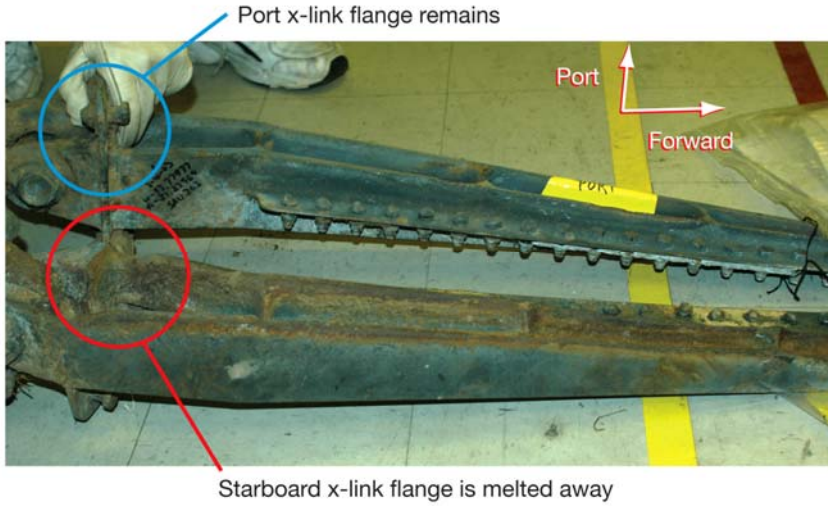


Figure 2.1-48. Comparison of port and starboard x-link flanges. [Columbia Reconstruction Database, debris item no. 1678 (top) and Columbia Reconstruction Database debris item no. 1765 (bottom)]



Figure 2.1-49. Close-up of the hole in the starboard x-link. [Columbia Reconstruction Database, debris item no. 1765]

At first it was assumed that the x-links received the thermal damage from entry heating as independent free-flying objects. For the ORSAT analysis, an x-link was modeled as a simple box (38 × 3 × 1.2 in.) at a stable attitude with a mass of 22 lbs. It was assumed the x-link broke off the orbiter at 200,000 feet with a relative velocity of 17,145 fps and a flight path angle of -0.68 deg. Based on debris field analysis, the actual separation was likely at a lower altitude and Mach number with lower resultant heat rates, making this assessment conservative.

The ORSAT analysis predicted that entry heating would not be sufficient to cause the damage seen. Also, a free-flying x-link was not predicted to stabilize in one attitude; a tumbling x-link would diffuse the heat better and also not result in the directional heating seen. The similar melting patterns on the two x-links suggests that they were in the same relative orientation at the time the thermal event occurred, presumably still in place attaching the CM to the FF. This led to a more detailed analysis to understand what heat rate would be required to show the damage seen.

The amount of heat to completely melt an object is known as the heat of ablation. The heat of ablation per mass has two components, which are additive: latent heat and sensible heat. Latent heat is the amount of energy in the form of heat released or absorbed by a substance during a phase transition (such as from solid to liquid). The latent heat per mass for titanium is 187 Btu per pound of mass (Btu/lbm). Sensible heat is potential energy in the form of thermal energy or heat for an object. The amount of sensible heat per mass required to raise the temperature of titanium to its melting temperature can be determined by integrating the plot from the initial temperature to the final temperature (figure 2.1-50). Data did not extend beyond 1,600°F (871°C).

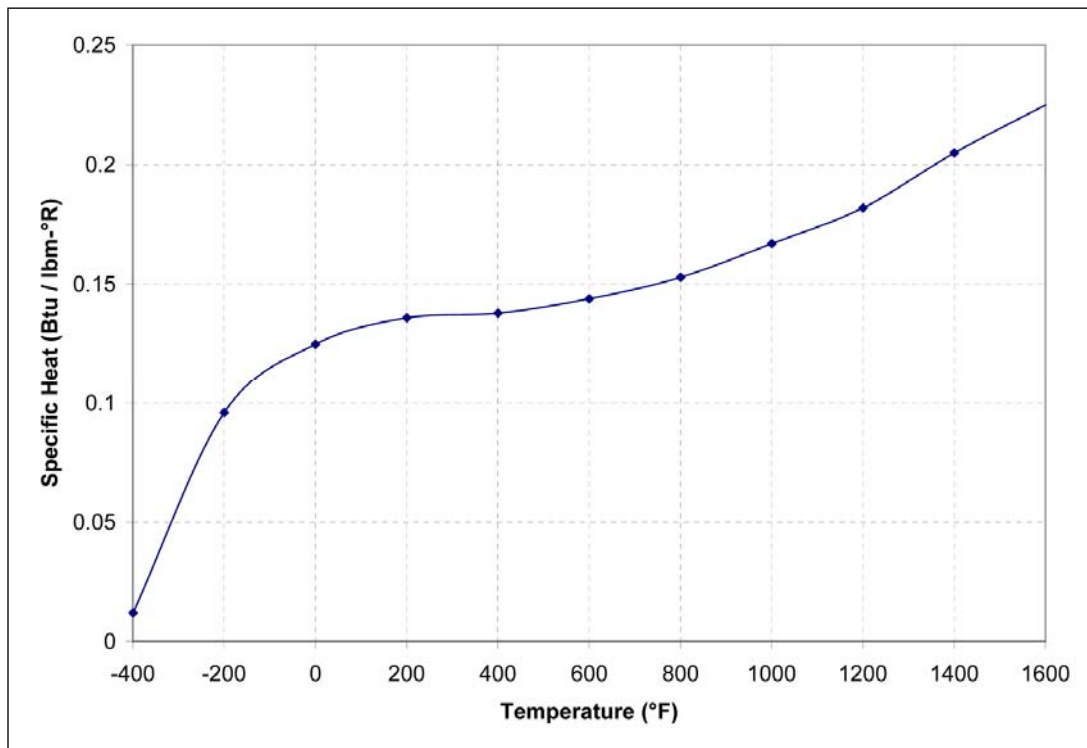


Figure 2.1-50. Specific heat of titanium vs. temperature.¹⁷

Assuming an initial temperature of 80°F (27°C) and that the specific heat at 1,600°F (871°C) does not change until the melting temperature is reached, the amount of sensible heat required to reach the melting temperature of titanium is 564 Btu/lbm, or 750 Btu/lbm to completely ablate the material. It is possible that

¹⁷Thermal Protection Materials, NASA Reference Publication 1289, December 1992.

the x-link was pre-heated by earlier exposure to entry heating as the forebody rotated. The maximum pre-heating considered reasonable was 400°F (204°C), the temperature at which the surrounding aluminum structure would begin to soften and likely release the x-link. If the x-link was pre-heated to 400°F (204°C), the amount of sensible heat per mass required to reach the melting temperature is reduced to 521 Btu/lbm and the heat of ablation per mass is reduced to 710 Btu/lbm.

Knowing the heat of ablation per unit of mass allows a first-order estimate of the required heating that must be applied to cause that burn-through hole in the starboard x-link. The dimensions of the burn-through area are 2 in. by 2 in. and the thickness of the x-link in that area is 0.25 in.

The required heating rates to cause the burn-through hole as a function of time for initial temperatures of 80°F (27°C) and 400°F (204°C) are shown in figure 2.1-51. It can be seen that the heat rates are extremely high for either case, and increase exponentially as the time required to cause the hole decreases. For comparison, figure 2.1-51 also shows the heating rate from entry aeroheating for an x-link exposed at 200,000 feet (dark blue line). This shows that the x-links would have to be exposed to sustained directional entry heating for more than 25 seconds to result in the thermal damage received.

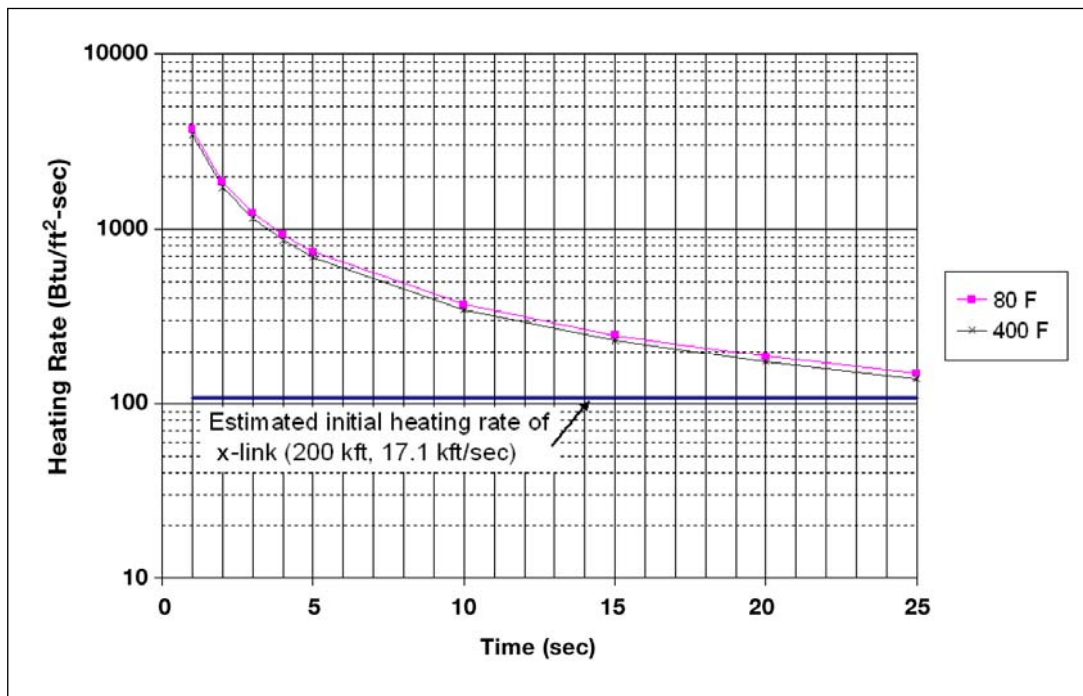


Figure 2.1-51. Heating rates required to ablate a titanium hole of 0.25 inch in depth.

The question now became how such severe and similar directional heating of the two titanium x-links occurred in a short time span without melting the surrounding material, which had lower melting temperatures. Because the forebody was not likely to stabilize at a given attitude, there would be very brief durations of exposure as the x-link happened to pass through the velocity vector as the free-flying forebody rotated. The longest reasonable duration for the rotating forebody to experience peak heating was felt to be less than 3 seconds and possibly as short as 1 second. To melt a hole in 3 seconds, the required heat rate is about 1,350 Btu/ft²-sec. To melt a hole in 1 second, the required heat rate is over 3,900 Btu/ft²-sec. These values are an order of magnitude higher than the estimated peak heating due to aeroheating of 110 Btu/ft²-sec.

Finding. Thermal analyses predicted that entry aeroheating alone was insufficient by an order of magnitude to produce the observed thermal damage on the x-links. Therefore, the x-links must have experienced other heating mechanism(s) in addition to normal entry heating.

This was a very surprising result, and led the team to research other heating mechanisms. Two thermal mechanisms, shock-shock interaction and titanium oxidation/combustion, could generate the observed thermal damage either separately or in tandem. Both of these mechanisms are discussed in detail in Section 2.1.7.

2.1.6.8 Thermal analysis – payload bay door roller

Another instance of the thermal erosion of high-temperature materials was seen in the PLBD rollers, which contain notable amounts of titanium. Initially, the interest in the PLBD rollers resulted from a search of possible sources for the titanium deposition that was found on the overhead windows (see Section 2.4).¹⁸ A search for forward structures containing titanium showed that the nearest source of titanium material to the windows was the forward PLBD rollers. These rollers are made of aluminum, titanium, and an Inconel sleeve, and the PLBDs rest on them when the doors are closed. The forward rollers are attached to the top of X_o 582 ring frame bulkhead in close proximity to the windows on which the titanium depositions were found (figure 2.1-52). Several recovered rollers from this location showed pronounced erosion of the exposed titanium surfaces, and one roller was recovered with only part of the Inconel sleeve remaining; all titanium and aluminum inner structures were missing (figure 2.1-53). Table 2.1-2 shows the material properties of stainless steel (A286), Inconel 718, aluminum 2000 series, and titanium 6Al-4V. As shown, the Inconel and aluminum alloys used in the rollers both have lower melting temperatures than the titanium alloy.

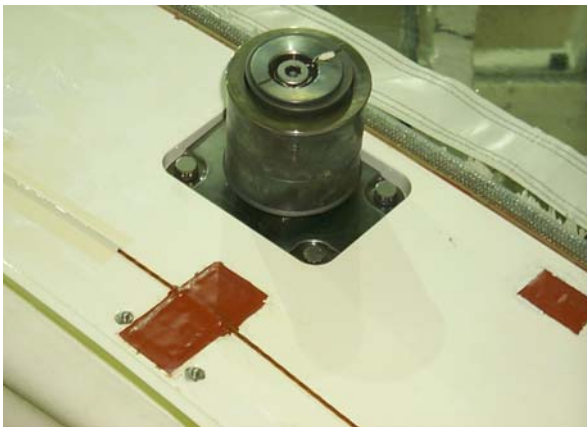


Figure 2.1-52. Payload bay door roller showing inner material and Inconel sleeve.



Figure 2.1-53. Recovered payload cylinder bay door roller with inner material absent and Inconel sleeve remaining. [Columbia Reconstruction Database, debris item no. 10914]

Table 2.1-2. Material Properties Important to Thermal Analyses

Material	Melting Temperature (°F)	Melting Temperature (°C)
A 286 (stainless steel)	2,500	1,371
Inconel 718	2,368	1,298
Aluminum 2024	1,081	583
Titanium-6Al-4V	3,037	1,669

A computational fluid dynamics (CFD) thermal analysis of the rollers was performed to determine the flow field environment and temperature at the face of a roller for an orientation with the front of the roller facing directly into the direction of travel. Figure 2.1-54 shows the predicted heating rate and temperature distribution along the PLBD roller at Mach = 10.5.

¹⁸J. D. Olivas, L. Hulse, B. Mayeaux, S. McDanel, P. Melroy, G. Morgan, Z. Rhaman, L. Schaschl, T. Wallace, and C. Zapata, *Examination of OV-102 Thermal Pane Window Debris – Final Report*, KSC-MSL-2008-0178 (in press).

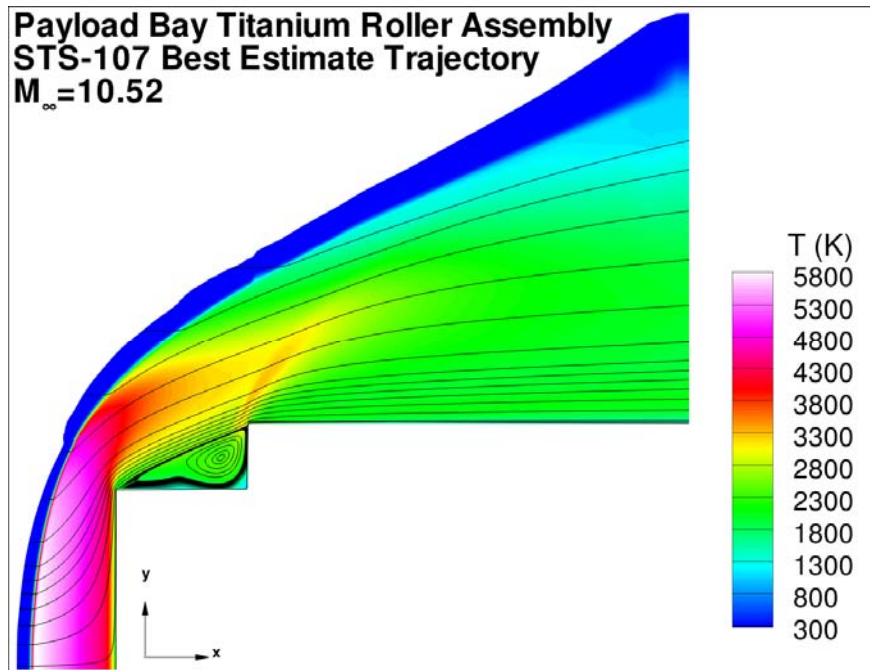


Figure 2.1-54. Computational fluid dynamics analysis of heating at the tip of the payload bay door roller for orthogonal geometry into the direction of travel at $M = 10.5$.

It can be seen from figure 2.1-54 that for Mach numbers greater than 10, the possibility exists that radiative equilibrium surface temperatures in excess of the melting temperature of titanium ($\sim 3,000^{\circ}\text{F}$) ($1,662^{\circ}\text{C}$) can be achieved. Ablation then could occur by pressure forcing away the molten titanium on the surface.

When ORSAT was used to analyze the case of the titanium rollers, the calculated heating rates across the front face compared very well to the results from the CFD case, given the same assumptions regarding geometric orientation and free-stream conditions (figure 2.1-55) for Mach 7.5 to 10.5.

In figure 2.1-55, the heating rate increases along the front face from the center to the edge because the flow is accelerating around the corner of the front face of the roller. The first spike comes from the flow going over the edge of the inner cylinder, and the second spike comes from the flow over the (outer) sleeve cylinder. If a boundary with grid representing the payload bay forward wall had been used in the CFD analysis, it may possibly have shown a shock-shock interaction that might account for the hole found in the surrounding X, 582 ring frame bulkhead structure on either side of the roller.

The next question was whether the observed amount of material loss was reasonable for the timeframe. As mentioned before, heating only occurs when the object is facing into the direction of travel, yet it is not believed that the forebody stabilized in a specific attitude. Additionally, the nature of the window deposition indicates that the titanium and titanium/aluminum deposition event was continuous and not cyclical. Therefore, the entire titanium/titanium aluminum ablation event had to occur in a relatively short period of time. Given an attitude change of approximately 36 deg/sec (0.1 rev/sec), the maximum duration of heating considered reasonable was about 3 seconds. In any attitude other than directly into the velocity vector, heating is less but is still present. Therefore, the CFD analysis only showed the peak heat was possible. It seems probable that some additional mechanism would be required to deeply erode the rollers.

The analysis of the x-links (see previous section) also suggests that there might be mechanisms other than simple entry aeroheating at work. The first mechanism evaluated was shock-shock interaction.

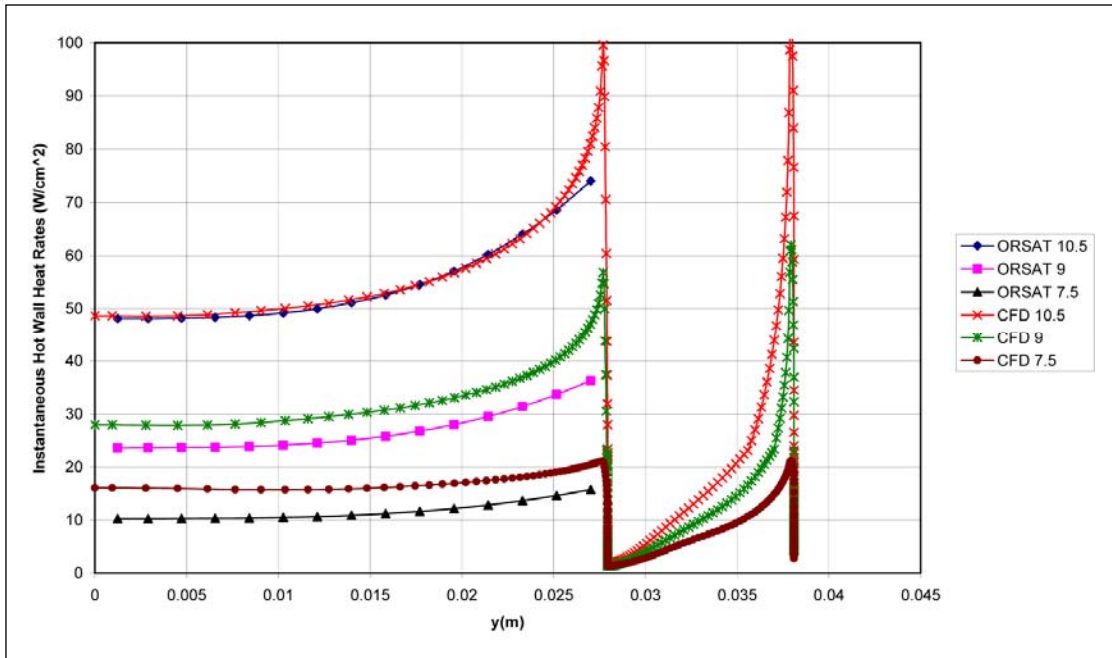


Figure 2.1-55. Comparison of the object reentry survival analysis tool and computational fluid dynamics heating rates for the front face of the payload bay roller for various Mach numbers. Y axis is radial distance from the center of the roller.

2.1.7 Shock-shock interaction and combustion

Shock-shock interaction occurs when two shock waves intersect. Figure 2.1-56 shows an example of one interaction on the orbiter leading edge.

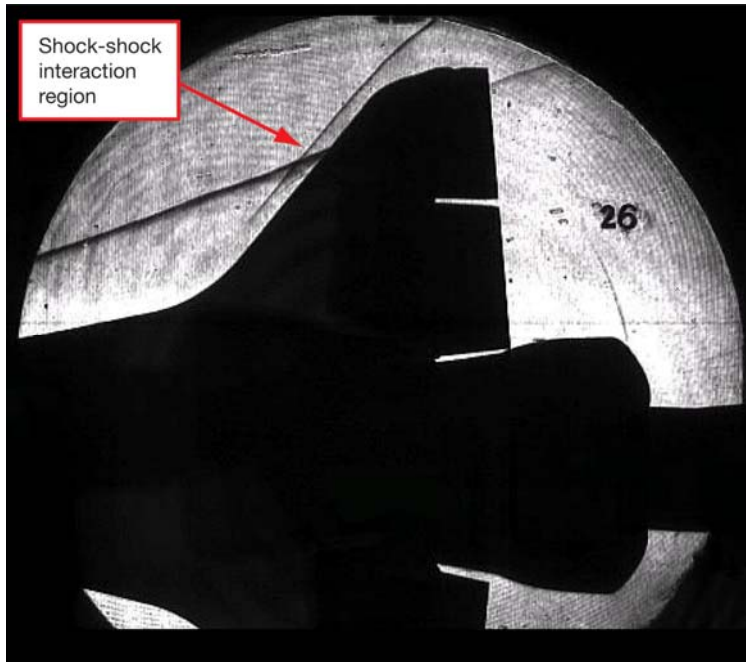


Figure 2.1-56. Schlieren photograph of the orbiter showing a shock-shock interaction region for nominal entry.¹⁹

¹⁹This profile was taken from orbiter aerothermodynamic heating tests at the Calspan-University of Buffalo Research Center, shock tunnel facility at Buffalo, New York at a Mach number of 10.

These shock-shock interactions influence a vehicle's aerodynamics and increase the heat transfer rate and pressure where the interaction impinges on the vehicle's surface. There are six types of shock-shock interactions.²⁰ These types are defined by where the incident and bow shock waves intersect, the strength of the incident shock, and the angle on the blunt leading edge surface with respect to the impinging shear layer. Shock-shock interaction was examined to determine whether it could explain the thermal damage observed on the x-links and PLBD rollers.

The best candidate for the extreme heat rates is called a Type IV shock-shock interaction. Type IV shock wave interference can cause stagnation rates to be amplified by a factor of 38 for a Mach number of 16, which is slightly higher than the Mach number at orbiter breakup. This amplification factor could increase the baseline heating rate to almost 4,000 W/cm², so it would only take about 1 second to burn-through the titanium. These Type IV shock wave interference scenarios cause a jet that is very small and will result in highly localized heating.

Type IV shock waves are highly dependent on geometry relative to the airflow. Due to the chaotic nature of the vehicle breakup, it was not considered reasonable to attempt to determine the precise geometry for the PLBD rollers or the x-links that would result in a Type IV shock wave. However, experts did determine that there was no reason to rule out shock-shock interactions based on geometry.²¹

Therefore, theoretically a shock-shock interaction can help explain the type of damage seen on the rollers and starboard x-link. However, two questions still remained. The first was the original mass loss rate question from the PLBD rollers. The second question was why surrounding materials with lower melt temperatures, such as aluminum and the Inconel roller sleeves, remained relatively intact in such an intense environment. The aluminum condition could be explained by the fact that it has much greater thermal conductivity than titanium. With sufficient mass, it is capable of withstanding higher heating rates because it can create a more effective heat sink. Since most of the CM is made of aluminum, the aluminum portions of the structure may have been very effective at shunting heat away from locally exposed regions during a period of high localized heat exposure. However, the thermal conductivity of Inconel is much lower, closer to that of titanium, and the relative lack of damage to the Inconel cannot be explained by heat shunting. This introduced the possibility that the titanium may have reacted differently chemically to the environment than the other materials around it.

Crystallographic assessment by the JSC Materials and Processing Office, the JSC Astromaterials Research Office, the Kennedy Space Center (KSC) Failure Analysis and Materials Evaluation Branch, and the White Sands Test Facility on the nature of the oxide formation on the window indicated that deposition occurred at a temperature that was well above the melt temperature of the titanium alloy. The crystallographic and microscopic work further indicated that the oxide species were fluid once deposited on the windows and did not experience solidification during transportation from the source to the deposition site. These additional clues further implied some significant secondary mechanism.²²

One important difference between titanium and the other materials is that titanium is highly reactive with O₂. In fact, titanium is often used as an igniter or a promoter, much like magnesium. Oxidation is an exothermic reaction, and the chemical reactions that occur can introduce heat into the material through bulk material conversion from a molten metallic state to an oxidized state. This could explain why the Inconel (which is not particularly reactive in terrestrial O₂ environments) did not thermally erode, although the melt temperature is more than 600°F (316°C) lower than that of titanium (Table 2.1-2), and why the titanium alloyed material reacted and deposited on the windows earlier than other materials.

It is very difficult to predict the combustion process of metals with the analytical tools used for this investigation. The ORSAT code used for much of the aerothermal analysis in this study does have a

²⁰Barry Edney, "Anomalous Heat Transfer and Pressure Distributions on Blunt Bodies at Hypersonic Speeds in the Presence of an Impinging Shock," The Aeronautical Research Institute of Sweden, 1968.

²¹Allan Wieting, "Shock-Shock Wave Interference Heating Possibilities," March 2007.

²²J. D. Olivas, M. C. Wright, R. Christoffersen, D. M. Cone, and S. J. McDanel, *Crystallographic oxide phase identification of char deposits obtained from space shuttle Columbia window debris*, Acta Materialia, 2008 (in press).

primitive function for determining oxidation, so the phenomenon is not unforeseen. However, there are many limitations to the model. The ORSAT function only accounts for the mass loss of the material as it is consumed by oxidation, not by a combustion reaction. ORSAT accounts for this by creating an additional component of heat that is formed by the reaction of the metal and molecular O₂. During vehicle deceleration from high Mach numbers, O₂ is dissociated into its monatomic form (O) which is much more chemically reactive than molecular O₂. A literature search and survey of major testing facilities proved that investigation into the effects of high enthalpy-low pressure environments on bare titanium has been very limited in the past.²³

The shock-shock interaction discussed previously was not easy to test. However, simple experiments could be conducted, using an arc-jet facility, to understand whether titanium combustion could have occurred in the *Columbia* entry environment.

A selection of enthalpy-pressure test points was chosen based on the predicted trajectory and ballistic number of *Columbia* and the free-flying forebody. A series of tests was conducted at the Boeing St. Louis Large Core Arc Tunnel (LCAT) plasma arc facility.²⁴ This testing showed that in some higher enthalpy conditions the titanium test article eroded within a few seconds and exhibited behavior that is characterized as combustion. Although mass loss rates are not known, this type of oxidation can become a sustained reaction and does not necessarily require the continued exposure to heating to continue.

An analysis was done using ORSAT to see whether the model could account for the thermal effects seen in the arc-jet test without combustion. In lower enthalpy cases, the model matched arc-jet test results very well. However, at the higher enthalpy cases, there were incongruities that could not be accounted for by entry heating alone.²⁵ The conclusion was that titanium combustion was possible for the *Columbia* entry environment. This appears to be the first documented characterization of this material physical property.

Additionally, the arc-jet test team noted that geometry also appeared to play a possible role in the initiation of oxidation. This provides the intriguing possibility that momentary shock-shock interactions, which might not erode titanium significantly on their own, may have acted as a trigger for oxidation, combustion, and heavy erosion.

The fact that combustion was only seen at higher enthalpies and pressures suggests that if oxidation occurred, it was most likely when the forebody was still intact as the smaller individual objects are not likely to generate the heat required. The fact that the rollers deposited material on the windows combined with the similar directional heating on both x-links implies structural integrity of the forebody, which is consistent with this conclusion.

In conclusion, some of the thermal mechanisms experienced during the *Columbia* entry were different from those of a nominal entry, implying the possibility of shock-shock impingement, titanium oxidation, or a combination of both effects resulting in rapid and selective melting of titanium prior to the aluminum around it.

Conclusion A13-1. Titanium may oxidize and combust in entry heating conditions dependent on enthalpy, pressure, and geometry.

Conclusion A13-2. The heating from a Type IV shock-shock impingement and titanium combustion (in some combination) likely resulted in the damage seen by the forward payload bay door rollers and the x-links.

²³William Rochelle, "Survey of Titanium Testing at NASA, DOE, and DOD Test Facilities," ESCG-4380-06-AFD-MEMO-0011, April 20, 2006.

²⁴J. D. Olivas, B. Mayeaux, P. Melroy, and D. Cone, Study of Ti Alloy Combustion Susceptibility in Simulated Entry Environments, AIAA, 2008 (in press).

²⁵W. Rochelle, J. Marichalar, M. Larin, A. Dobrinsky, J. Dobarco-Otero, and Ries Smith, "Comparison of LCAT Arc-Jet Titanium Plate Test Data with Aerothermal Predictions," ESCG-4380-07-AFD-MEMO-0012, April 20, 2007.

Recommendation A13. Studies should be performed to further characterize the material behavior of titanium in entry environments to better understand optimal space applications of this material.

2.1.8 Synopsis of motion and thermal analyses

In summary, the motion and thermal analyses of the vehicle and forebody produced significant results and findings. The loads experienced by the intact orbiter and the free-flying forebody were estimated based on a reference trajectory and attitude analyses. The forebody and CM of the orbiter are not expected to trim into a single aerodynamic attitude upon breakup of the vehicle. Thermal analyses results were multifaceted. In some cases, thermal models showed good agreement with debris condition, such as for the crew helmets. In other cases, geometry and protection from other structure proved too complex to model accurately. Further research is warranted to investigate other thermal mechanisms (shock interaction, combustion) to provide greater understanding of aerothermal effects on entry.

2.2 Orbiter Breakup Sequence

This section discusses the breakup sequence of the orbiter following the LOC. The CAIB concluded that the orbiter was shedding debris throughout entry.¹ LOS occurred at GMT 13:59:32. RGPC on-board data indicate that the Freon coolant loops in the PLBDs were still intact at GMT 14:00:04.8, indicating that the radiators and PLBDs were still intact. After GMT 14:00:04.8, no GPC data could be recovered. The on-board MADS/OEX recorder was powered until GMT 14:00:18, the time known as the CE. Based on video analysis, at GMT 14:00:18 the orbiter was no longer intact.² At this point in the entry, the orbiter was estimated to be at an altitude of 181,000 feet and traveling at Mach 15.

The SCSIIT relied upon analysis of ground-based video, analysis of debris recovery locations, ballistic analysis, and structural analysis to reconstruct the sequence of events experienced by *Columbia*. This section provides the framework for the sequence of structural failure and covers large-scale events that are related to orbiter structure and the separation of the forebody from the intact orbiter. Section 2.4 discusses events specifically related to the forebody breakup. These sections overlap in certain areas. Detailed description of the analysis techniques are contained in this section and are not repeated in Section 2.4.

The orbiter breakup sequence discussion is presented by type of analysis. The first is the *video analysis*. Analysis of ground-based videos consisted of reviewing all ground-based video of *Columbia*'s entry. Ground-based video analysis allowed a time-tag to be assigned to specific visual events that were seen in ground-based video. Considerable elements of the analysis were performed for the CAIB³ although the SCSIIT performed additional analysis. On-board video is discussed in Sections 3.2 and 3.4.

The next analysis presented is the *ballistic analysis*, which used ground location, size, shape, and mass of recovered debris items. As an individual piece of debris was shed, it took on a unique ballistic trajectory based on its ballistic number (see Appendix). Heavier items with larger ballistic numbers travel farther downrange (in this case, east), while lighter items with smaller ballistic numbers decelerate quickly and achieve terminal velocity, traveling essentially straight down to the ground. Therefore, comparing the impact location alone of any one piece of debris relative to another will not provide information about the time or sequence of release; a detailed ballistic analysis comparing their trajectories is required. The modeled debris was iteratively connected to the reference trajectory (see Section 2.1) until the calculated ground impact longitude matched the actual recovered longitude of the item. This is a lengthy process and is heavily dependent on understanding the aerodynamic characteristics of the object in question. It is easiest to do this analysis on simple shapes, such as spheres and boxes. As a result, only select items have ballistic assessments. Conducting ballistics analysis on several debris items that came from the same general zone on the orbiter (such as the right wing, or aftbody) could provide a general release time for that specific structure. These times can be correlated with video events to produce a time-based breakup sequence.

The team elected to perform ballistics only on key items of debris and *cluster analysis* on the remaining objects. Cluster analysis assumes that when the recovery locations of a large number of debris items from the same structural element (e.g. tail, wings, payload bay, CM) are considered, the debris will have a similar range of ballistic numbers. Evaluating the centroid of clusters of structural elements *relative* to each other can provide a relative sequencing of key events. Specifically, because the centroid of the cluster for one

¹*Columbia* Accident Investigation Board Report, Volume I, August 2003, p 12.

²*Columbia* Accident Investigation Board Report, Volume II, Appendix D.7, Working Scenario, October 2003, p. 209.

³*Columbia* Accident Investigation Board Report, Volume III, Appendix E.2, STS-107 Image Analysis Team Final Report, October 2003.

structural element X is west of the centroid of recovered debris from structural element Y, X was released before Y. Cluster analysis of the debris field consisted of plotting the latitude and longitude of recovered debris items that originated from a specific location (such as one of the wings) on the orbiter, identifying the centroid of the debris cluster, and comparing that to the cluster centroid of items from a different source (such as the other wing). A cluster identifies a ground recovery zone or “footprint” of debris from a specific source.

The conclusion was that comparing the locations of these clusters does, in most cases, produce accurate results of *relative* sequencing. It does not provide a time-based sequence. The relative sequence may not exactly coincide with the ballistically determined time-based sequence, which is considered more accurate. The inherent uncertainty contained in the ballistic time sequence due to the reference trajectory assumptions is an error range of ± 5 seconds. Other errors in the ballistic release times include the effects of cascading failures and the effects of aerodynamic lift, both of which bias release times later than the actual release time.

The *Columbia* Reconstruction Database (CRD) was critical to both the ballistic and the cluster analyses because it contains the records for ground recovery locations. When items were recovered in the field, typically their Global Positioning System (GPS) latitude and longitude were recorded. All recovered debris (approximately 84,000 pieces, or 39% of the orbiter⁴) were entered into the CRD, which is located at KSC. For details regarding the debris collection and processing, reference the *CAIB* Report, Volume II, Appendixes D.10 and D.11, and the Reconstruction Report.

Finally, *structural analysis* was based upon detailed engineering knowledge of the orbiter and forebody structures compared to the condition of the recovered debris. Given the knowledge gained from the video analysis, ballistic analysis, and subsequent cluster analyses, the overall structural analysis provided the most likely scenarios for failure modes of the orbiter.

The following is a summary of findings, conclusions, and recommendations from this section:

Finding. Ground-based video was a vital resource of data for understanding the accident, especially after telemetry was no longer available.

Recommendation A11. All video segments within a compilation should be categorized and summarized. All videos should be re-reviewed once the investigation has progressed to the point that a timeline has been established to verify that all relevant video data are being used.

Conclusion L3-2. The breakup of both *Challenger* and *Columbia* resulted in most of the X_o 582 ring frame bulkhead remaining with the crew module or forebody.

Recommendation L3-1. Future vehicles should incorporate a design analysis for breakup to help guide design toward the most graceful degradation of the integrated vehicle systems and structure to maximize crew survival.

2.2.1 Ground-based video analysis

There was no NASA ground-based video imagery of the entry and breakup of *Columbia*. Shortly after the *Columbia* accident, NASA issued a request to the public to submit any photographic stills or videos taken of the vehicle’s launch and entry that might aid in the mishap investigation. More than 170 videos and 1,500 stills as well as verbal accounts of the entry were submitted by the public to NASA. Most submitted video data had a variety of limitations for analysis, e.g., changing zoom factors and poor tracking. However, these videos were invaluable and contributed significantly to an understanding of the events of the last few minutes of *Columbia* and the crew.

⁴STS-107 *Columbia* Reconstruction Report, NSTS-60501, June 2003, p. 143.

The ISAG generated a master timeline that was comprised of two timelines; a “western” and an “eastern” timeline.⁵ The western timeline spans the orbiter’s trajectory from off the coast of California to New Mexico. A 2-minute-and-12-second gap in ground-based imagery coverage occurred as *Columbia* traveled from south of Santa Fe, New Mexico to Palo Pinto (just west of Dallas, Texas), GMT 13:57:31 to GMT 13:59:43. Video from the eastern timeline ends in Louisiana, where the engine powerheads impacted the ground.

Late in the SCSIT investigation, the team discovered an additional video that provided useful information that had not been included in previous analyses because it was not classified as important initially. After the mishap timeline had been established, it was more evident that this video provided unique data for an important timeframe. This video, which is referred to as NBC (National Broadcasting Corporation) (EOC2-4-0076-B), adds several seconds of good-quality imagery to the eastern timeline and begins at GMT 13:59:32.5 (± 1 second), just after LOS at GMT 13:59:32. The gap in video coverage was reduced by 11 seconds. More importantly, this video provided insight into the LOC. The vantage point of the NBC video is directly under the flight path of the orbiter. Unfortunately, when the forebody separates after the CE, its trajectory is above other debris pieces, so this video adds little additional information after the CE.

Video frames shown in this section are taken from various videos that capture several events. Each frame represents 1/29.95 of a second. The frames shown come from compressed video; the frames are not representative of the higher-quality frames that were used for evaluation. The “times” shown in the frames reflect the time code synchronization protocol of the Society of Motion Picture and Television Engineers (SMPTE), not GMT times. Even in the few videos where the GMT code is displayed, the time is only as accurate as the time to which the camera was set. The GMT times reported below the video frames shown in this report have been time-synchronized and should be accurate to within approximately 1 second. The one exception is the Apache video. The source of Apache was a military helicopter and the time was GPS-based and, therefore, highly accurate (<0.3 second).

Errors associated with video event times are impacted by the magnification of the FOV, resolution, and viewing geometry. These factors can introduce some error into the timing. A combination of error sources can lead to an accuracy of ± 1 second for defined events within a single video or between videos, although the actual error may be better or worse by up to an additional 1 second. This is more accurate than the ballistic trajectory times, which have a minimum error of ± 5 seconds. As a result, the video analysis was used to determine the timing of key events.

Finding. Ground-based video was a vital resource of data for understanding the accident, especially after telemetry was no longer available.

Recommendation A11. All video segments within a compilation should be categorized and summarized. All videos should be re-reviewed once the investigation has progressed to the point that a timeline has been established to verify that all relevant video data are being used.

2.2.1.1 Significant events seen in the video

Eastern timeline video coverage starts at GMT 13:39:32.5, immediately after LOS. There are four significant events for which there is video coverage: LOC, CE, CMCE, and Total Dispersion (TD). The CMCE and TD are discussed in Section 2.4. Significant debris shedding events are visible throughout the timeline.

Although SMPTE times that are seen in the frames are video-specific relative tape times, they can be correlated to GMT times if a visual event can be synchronized to a known GMT. The bright “dot” seen in the videos is the envelope of hot gases surrounding the orbiter during entry. Both the “dot” and the trail left by the orbiter are typical and expected visual signatures during entry. The apparent “star” around the orbiter is a lens flare, a common image effect due to the orbiter’s brightness and the lens system of a camera. This “star” is seen in most videos.

⁵*Columbia* Accident Investigation Board Report, Volume III, Appendix E.2, STS-107 Image Analysis Team Final Report, October 2003.

Loss of control

Figure 2.2-1 is the first frame of video for the eastern timeline. Figure 2.2-2 shows GMT 13:59:37, 135 frames (4.5 seconds) after figure 2.2-1. Figure 2.2-3, which shows 13 frames (approximately 0.5 second) after figure 2.2-2, correlates to LOC at GMT 13:59:37. The width of the trail increases at this time, which likely indicates a change in the flight condition. In addition to the change in the width of the trail, the trail appears to pulse or “corkscrew” over a period of less than 1 second (figure 2.2-4). This is consistent with the motion analysis, which suggests that the orbiter went into a flat spin.

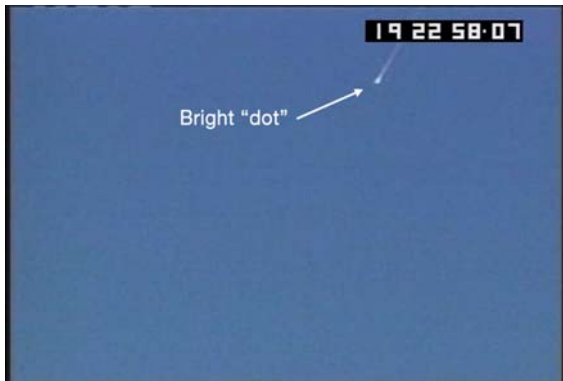


Figure 2.2-1. First frame of video of the Eastern timeline, GMT 13:59:32.5.



Figure 2.2-2. GMT 13:59:37.00.

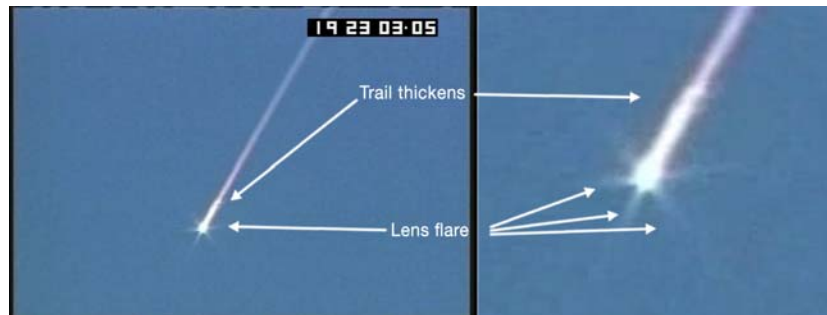


Figure 2.2-3. GMT 13:59:37.43, 13 frames after figure 2.2-2. Right image is a zoomed view of the left image.



Figure 2.2-4. GMT 13:59:37.80.

Catastrophic Event

The second significant event that is seen in video is the CE. Figure 2.2-5 shows the CE; there is no change in magnification between frames. The video of the CE is a distinct visual event in which the orbiter envelope brightens significantly and the trail width doubles. Additionally, some color change to orange is evident just prior to the CE. The color change is not readily visible in the still image frames that are taken from the video. In videos of the *Challenger* accident, an orange color was also seen in the videos and was assumed to be hydrazine, the material that is contained in the Orbital Maneuvering System (OMS) pods and RCS tanks. It is unknown whether the orange color seen in *Columbia*'s trail correlates to OMS or RCS tanks, or to some other cause.

Shortly after the brightening event and color change, a split trail is seen (figure 2.2-6). This strongly supports that the orbiter broke into multiple pieces at the time of the CE. The NBC video shows that the orbiter has an intermittent split trail prior to the CE. Prior to the CE, the split trails are tied to the separation of pieces of debris, and a singular main body trail continues after the separation of the debris. The split trail seen after the CE is constant; it does not dissipate and does not resolve back to a singular trail (figure 2.2-7).

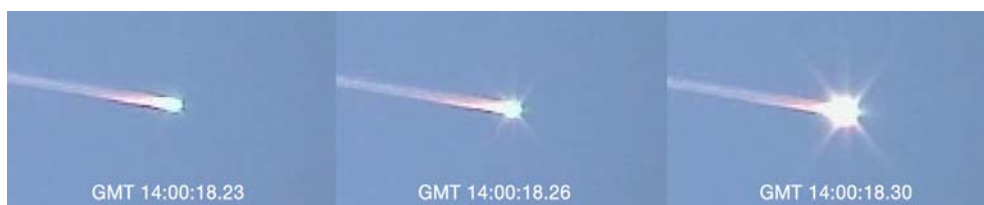


Figure 2.2-5. The Catastrophic Event is depicted in these three frames of video that cover 0.1 second. There is no change in the magnification/zoom factor. The third frame represents GMT 14:00:18.3.



Figure 2.2-6. Split trail after the Catastrophic Event. [GMT 14:00:18.6]



Figure 2.2-7. Persistence of the split trail 23 seconds after the Catastrophic Event. [GMT 14:00:41.1]

Due to camera effects of saturation of pixels, magnification settings, distance to the orbiter, and angle of view of the orbiter, visual separation of the major pieces of the orbiter is not identifiable until 8 seconds after the CE. The visual separation of the orbiter into separate identifiable pieces is first made evident by the appearance of a second “star” beside the first “star.” Figure 2.2-8 uses reversed color (“inverted”) images of the orbiter to more readily show the “star” (lens flares). The dark lines on the images are shown in an effort to illustrate the lens flares.

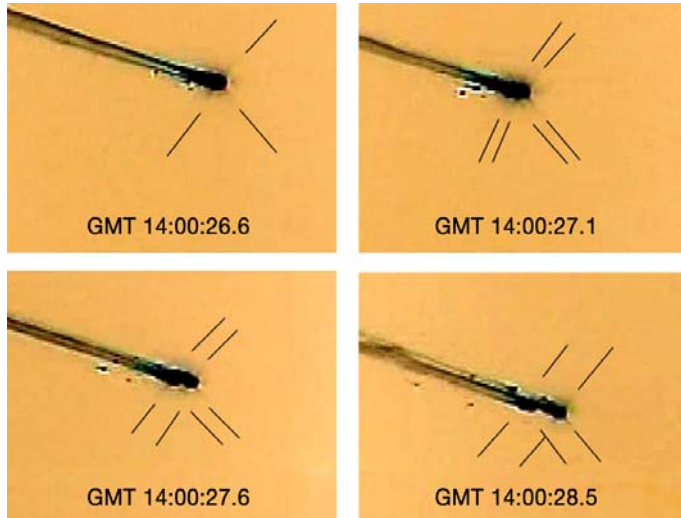


Figure 2.2-8. Color-inverted video images of the start of the double star event (GMT 14:00:26.6). Black lines have been added to more clearly identify the two separate objects.

The forebody breakup was identified at GMT 14:00:53 (see Section 2.4).

Other Major Structure Identification

Once the key events had been identified, an effort was made to tie specific debris shedding events with specific recovered debris. In particular, the team wanted to identify the forebody in the video. Heavier objects have a higher ballistic number and slower deceleration than lighter objects. Heavy objects, therefore, would be visible longer than other objects and could possibly be identified by their distinct trajectory in the video compared to other objects. The aftbody is the heaviest part of the orbiter, followed by the CM. The next heaviest item was SPACEHAB, which was located in the payload bay.

Six entry videos were found to offer the most information for debris shedding identification (Table 2.2-1). Videos are referred to by the name listed in the table. Figure 2.2-9 shows the debris tree created from these videos. The end time for a debris piece generally indicates when the object left the FOV of the video rather than the object breaking into pieces too small to be seen by the camera.

Table 2.2-1. Videos Used to Create the Debris Tree in Figure 2.2-9

Reference EOC No.	City in Texas	Name	Latitude	Longitude
EOC2-4-0024	Arlington	Arlington	32.7	-97.1
EOC2-4-0209-B	Hewitt	Hewitt	31.4	-97.2
EOC2-4-0221-4	Mesquite	WFAA4/Mesquite	32.8	-96.6
EOC2-4-0221-3	Fairpark	WFAA3	32.8	-96.7
MIT-DVCAM	Fort Hood	Apache	31.2	-97.6
EOC2-4-0077	Burleson	NBC	32.5	-97.3

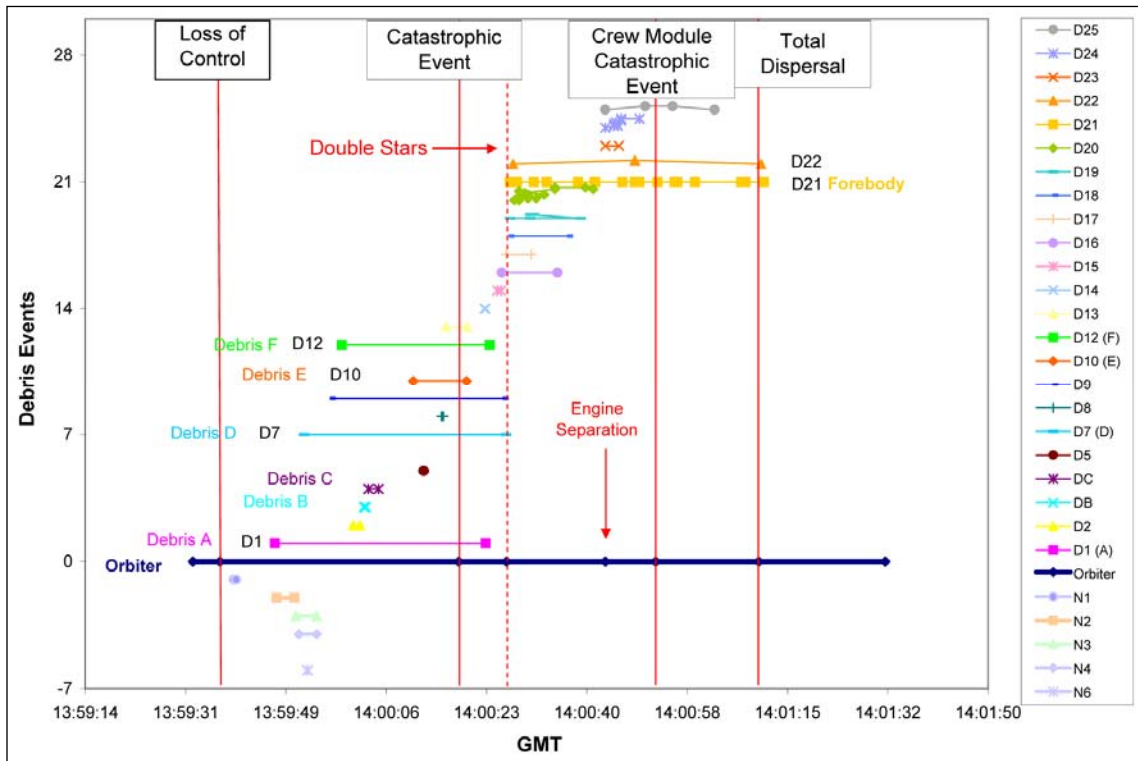


Figure 2.2-9. Debris tree.

The points that are labeled Debris A, B, etc. are the names that correlate to the master timeline provided to the CAIB.⁶ These were the starting point for the SCSiIT video analysis. When other videos were reviewed, they received a different numbering system. For example, debris shedding events that were identified in Hewitt were labeled D1, D2, D3, etc. In the NBC video, debris events were labeled N1, N2, N3, etc. When an object could be positively correlated with the originally identified debris events (A, B, C, etc), they were merged into that line, showing the full range across all videos for how long a specific debris object was visible in any video. If an object could not be clearly correlated with another video, it was kept separate in the debris tree and labeled accordingly.

The points that are seen on the various horizontal lines typically represent a significant piece separating from that debris piece. In some cases, these significant pieces are graphed with the parent piece. All the major events are marked on the timeline. Debris D through F and Debris 8 through 12 might have some overlap as objects but, due to different angles, were difficult to correlate.

Two pieces of debris (Debris A and, shortly afterward, Debris D) are seen in the NBC video (and some other videos) well before the CE. Debris A “flashes,” brightening and completely disappearing repeatedly, which is suggestive of tumbling. At times, the track and movement of the piece possibly suggests that it generates lift. At one point, the single flashing debris disappears and multiple smaller flashing debris appear, suggesting that Debris A broke into pieces. Debris D, however, paces the orbiter, suggesting that it is an object with significant mass and a high ballistic number. Given that the left wing and OMS pod were known to be structurally degrading in this timeframe, Debris A may possibly be the left OMS pod cover or a piece of the left wing, and Debris D may possibly be the left OMS pod, which is fairly heavy and substantial.

⁶Columbia Accident Investigation Board Report, Volume III, Appendix E.2, STS-107 Image Analysis Team Final Report, October 2003.

The aftbody is a part of the line labeled “orbiter” in the figure, since it was traced back to the intact orbiter and was the most persistent piece of the orbiter after the CE. It was easily identifiable because the engines separate from it late in the video.

Debris item 21 (D21) is identified as the forebody. This identification is based upon the mass of the forebody and trajectory in the video. Ballistic and debris field evidence later confirmed this assessment.

The points seen on the debris item 21 line represent all events that could be correlated to more than one video. Because of various camera viewing angles, correlation of debris pieces was difficult. Cross-correlation with three other videos showed that brightening events could be seen in many videos while few specific debris events could be cross-correlated.

The last time at which the main engines visually appeared to be a single unit is GMT 14:00:50.6; this is defined as the starting point for engine separation. Figure 2.2-10 shows the engines at GMT 14:00:53, the three pieces below the forebody which are circled in green. Their separation is already well under way. Considering that visual separation of the orbiter pieces after the CE took about 10 seconds, the actual time of separation of the engine components from one another may have been



Figure 2.2-10. Clear visual separation of the three main engines.

much earlier than GMT 14:00:50.6. Available data do not allow for a more accurate time of separation.

In summary, specific debris shedding events were very difficult to tie to specific recovered debris with a few exceptions. The forebody was positively identified, as was the aft section/engines. Debris A is possibly the left OMS pod cover. Debris D is possibly the left OMS pod. Debris D22 is suspected to be the SPACEHAB. The sequence, as derived from the video analysis, is presented in Table 2.2-2. It should be noted that the OMS pod time represents a time at which the debris piece is already clearly separated from the orbiter. The actual separation time could not be identified. Both forebody and (potentially) SPACEHAB are identified as separating from the rest of the orbiter at the CE. The times shown below indicate the video-based time of structural breakup.

Table 2.2-2. Orbiter Breakup Event Sequence and Times Determined by Video

Event	GMT
LOC	13:59:37
OMS pod cover	13:59:46
OMS pod	13:59:51
Orbiter breakup (CE)	14:00:18
SPACEHAB breakup (D22)	14:00:48
Main engines separate	14:00:50
Forebody breakup (D21)	14:00:53

2.2.2 Ballistic analysis

Ballistic analyses were conducted on selected recovered debris objects to help define the orbiter breakup sequence. The ballistic analysis determined an object’s approximate time of release from the vehicle given certain initial conditions. It should be noted that this type of analysis does not account for serial (cascading) debris events where a large object is released on its own trajectory and the object then breaks up into multiple smaller objects. Therefore, assessing an individual object has inherent uncertainty. For objects that left the vehicle in almost the same configuration as they were recovered (i.e., an individual item of crew equipment), the ballistic numbers and times of release have a higher confidence level. However, conducting ballistics

analysis on several debris items from a specific zone of origin on the orbiter can provide a general release time for that specific structure.

The process is called “ballistic analysis” because all the objects are assumed to become ballistic upon release. The trajectory of a ballistic object is unique to the properties of that object and is not controlled by power or directional steering. A good example would be a ball fired from a cannon. The cannonball’s trajectory is determined by the forces acting on it: its momentum (mass \times velocity), the drag from the atmosphere, Earth’s gravity, and winds (figure 2.2-11).

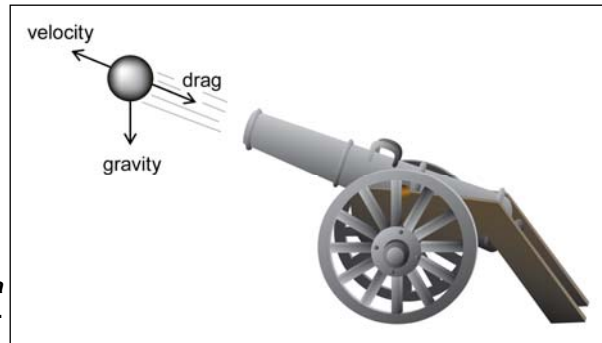


Figure 2.2-11. A cannonball is an example of a ballistic object.

The modeling tools used in the ballistic analysis were Snewt and SORT (see Chapter 4).

Objects were selected for ballistic analysis based upon weight, shape, original location on the orbiter, and possible relevance to the breakup sequence. For each debris object, a reference area, reference length, and c.g. location were specified. The c.g. location of some analyzed debris items was already known. For others, the c.g. location was measured from the debris recovered, or the c.g. location was estimated. The aerodynamic coefficients were generated at different orientations through an alpha (angle-of-attack) and beta (sideslip angle) sweep or at a significant number of random orientations. The ballistic number can be determined using aerodynamic coefficients. It is possible to average the ballistic number of the various orientations to come up with an average ballistic number. The more “regularly” shaped the object is (sphere, cube, rectangular prism, flat plate, etc.), the more precisely the average ballistic number can be computed. For most of the objects analyzed, the average ballistic number was used because it was assumed that the objects were tumbling and, therefore, were constantly changing their orientation. Very few objects had directional thermal erosion, indicating that they had aerodynamically trimmed in a specific orientation. For these objects, the ballistic number for that orientation was used. The average ballistic number assumption can introduce errors in both directions for release time because the actual ballistic number may have been either larger or smaller than the assumed average.

After the aerodynamic coefficients were calculated, the object’s approximate release time could be determined. As previously stated, there is an error bar of ± 5 seconds in release times due to the uncertainty in the reference trajectory used as a baseline for the item to be released from.

Release times for large structures were determined using the estimated release time of their subcomponents. However, these estimated times do not take into consideration cascading failures of these large objects. The recovered debris objects were separated into categories of large orbiter structure, such as left wing, OMS pod, forward bulkhead, aft bulkhead, etc. Each category of objects recovered on the ground made a cluster along the ground track. It was first thought that objects in the westernmost part of a given cluster would have the lower ballistic numbers, and objects to the east would have the larger ballistic numbers. However, it was found from examining the database of recovered items that each debris cluster included many low-ballistic-numbered objects, meaning that cascading failure was common. Items may in fact be part of a larger object that separated earlier, for which a trajectory is not known. Only the trajectory of the individual item can be computed. Cascading events generally result in calculated release times for individual items that are later than the actual release times.

Another key assumption in the ballistic analysis was that the analyzed objects did not have lift. To determine whether an object could have generated lift, the shape and especially the orientation of the object during flight has to be known. Since that knowledge was not available, drag-only or ballistic flight was assumed. In general, an object with lift will travel a greater downrange distance than that same object on a purely ballistic trajectory, causing an error in release time that is biased to a later time than actual release.

Since cascading failures and lift would send an object farther downrange (east) than expected from a simple ballistic trajectory, a decision was made to use items from the westernmost (earliest) edge of each cluster and to use easily modeled items (such as flat plates) when possible to estimate the release time of the large orbiter structure. A conscious effort was made to choose items such as structural skin rather than tiles or reinforced carbon-carbon (RCC), which were continually shed during the entire entry. If three or more debris items were found that gave the same estimated release time, confidence was increased that the large orbiter structure came off at that time. The estimated time of release of large structures is referred to as the major structural release time.

For further information on ballistics, see Appendix A.

2.2.2.1 Major structural release times

The estimated release time is the calculated time at which an object was released from the reference trajectory, given the previous assumptions and conditions. Table 2.2-3 shows the estimated release times for large orbiter structures. After the CE, the vehicle was no longer intact and was in at least three major pieces (forebody, midbody/right wing, and aftbody). Some of the subsequent release times reflect separation from those major pieces, not the intact orbiter.

Table 2.2-3. Release Times of Large Structures

Major Structural Release Time (GMT)	Vehicle Structure	Time of Release (GMT) and Debris Object Number ⁷
13:59:48	Left OMS Pod (skin, structure, honeycomb)	13:59:48 (78899)
		13:59:57 (85446)
		14:00:16 (84132)
14:00:04	Left Wing (RCC, upper and lower wing skin)	14:00:02 (70391)
		14:00:05 (81331)
		14:00:05 (11525)
CE		
14:00:26	Midbody Fuselage	14:00:20 (82427)
		14:00:33 (82172)
		14:00:35 (38315)
14:00:27	Right Wing (RCC, skin, structure)	14:00:24 (68702)
		14:00:26 (24508)
		14:00:28 (8172)
		14:00:30 (49833)
14:00:31	SPACEHAB	14:00:29 (65045)
		14:00:33 (7641)
		14:00:57 (22900)

⁷The debris object numbers are the numbers that are assigned to each recovered object when its recovered location, description, weight, dimensions, etc. was entered into the *Columbia* Reconstruction Database for tracking and identification.

Table 2.2-3. Release Times of Large Structures (Continued)

Major Structural Release Time (GMT)	Vehicle Structure	Time of Release (GMT) and Debris Object Number ⁸
14:00:34	Vertical Tail (structure, drag chute panel)	14:00:26 (26078) 14:00:27 (77800) 14:00:38 (85279) 14:00:39 (1633) 14:00:40 (45837) 14:00:48 (52092)
14:00:34	Aft Fuselage (Carrier Panel, structure)	14:00:32 (43091) 14:00:33 (31308) 14:00:36 (79178)
14:00:36	Internal Airlock soft stowage items	14:00:36 (65900) 14:00:36 (31297)
14:00:43	Tunnel Adapter structure	14:00:42 (64966) 14:00:44 (69606)
14:00:54	Aftbody forward bulkhead (X _o 1307)	14:00:52 (12877) 14:00:52 (83678) 14:00:53 (14559) 14:00:57 (64156)

Large structural pieces, such as the left OMS pod or left wing, were not released from the orbiter at a single time as is implied by the major structural release time. The objects in this section should not be considered as being released from a single complete orbiter, but from (at minimum) three separate objects. Table 2.2-4 compares the sequence suggested by video against the sequence suggested by ballistic assessment.

Table 2.2-4. Comparison of Video and Ballistic Sequence

Video Sequence (relative)	Ballistic Sequence (time-based)
OMS Pod	OMS Pod
	Left Wing
Forebody/Midbody/Aftbody (CE)	Midbody
	Right Wing
SPACEHAB	SPACEHAB
	Vertical Tail
	Aftbody
Main Engines	Main Engines
Forebody	Forebody

The differences between the two sequences can be explained by cascading events where major portions of the vehicle, such as the aftbody and the forebody, remained intact for some time. One conclusion from this comparison is that the relatively lighter components making up the midbody, including the wings and payload bay, disintegrated fairly rapidly and as individual objects while the aftbody, SPACEHAB, and the forebody maintained some integrity.

⁸The debris object numbers are the numbers that are assigned to each recovered object when its recovered location, description, weight, dimensions, etc. was entered into the *Columbia* Reconstruction Database for tracking and identification.

2.2.3 Cluster analysis

This section addresses the cluster analysis that shows how the pattern of recovered debris aided in understanding the sequence of the orbiter breakup.

An evaluation of the debris field was conducted to match debris sources (orbiter structural zone) with debris recovery locations. In all cases for the debris maps that follow, the orbiter travels from approximately the upper left corner (northwest) to approximately the lower right corner (southeast). Although debris was seen falling away from *Columbia* in ground-based video as far west in its trajectory as off the coast of California, the farthest west confirmed *Columbia* debris was recovered in Texas.

The location of debris on the ground is influenced by when the debris separated from the orbiter and how far the object traveled downrange. As a general rule, heavier objects travel farther downrange (to the east, in this case) than lighter items of similar shape and size. In addition, wind effects and, possibly, lateral forces exerted during orbiter breakup had some effect as evidenced by the lateral dispersion of objects.

The center of a large debris group was considered reasonably accurate for relative sequencing, with ballistics allowing for refinement and correction, if needed. Cascading debris failures and lift generation will result in biasing the debris cluster farther east (artificially elongated at the trailing end) and greater lateral spread for the same reasons as the effects on the ballistics analysis. Wind, which at the time of the mishap was prevailing from the southwest, can also affect the debris field cluster shape and centroid.

However, cross-referencing ballistic release times across a range of clusters showed that as few as five objects in a debris group can allow some conclusions to be drawn *if the objects have approximately the same range of ballistic numbers*. When five or more items were available to determine a cluster, there was fairly high confidence in comparing that cluster to another.

Knowledge of the topographic conditions was important in some instances, where water hazards or thick brush interfered with debris recovery efforts. Some graphs show that fewer debris items were recovered in certain areas, suggesting a decrease of debris when, in fact, the debris field thinning is related to field conditions and obstacles that impeded the ability to locate the debris items.

2.2.3.1 Debris clusters

The orbiter is made up of multiple structural elements (figure 2.2-12). The recovery location data of the debris were divided into many of these structural elements to determine the apparent sequence in which the orbiter failed.

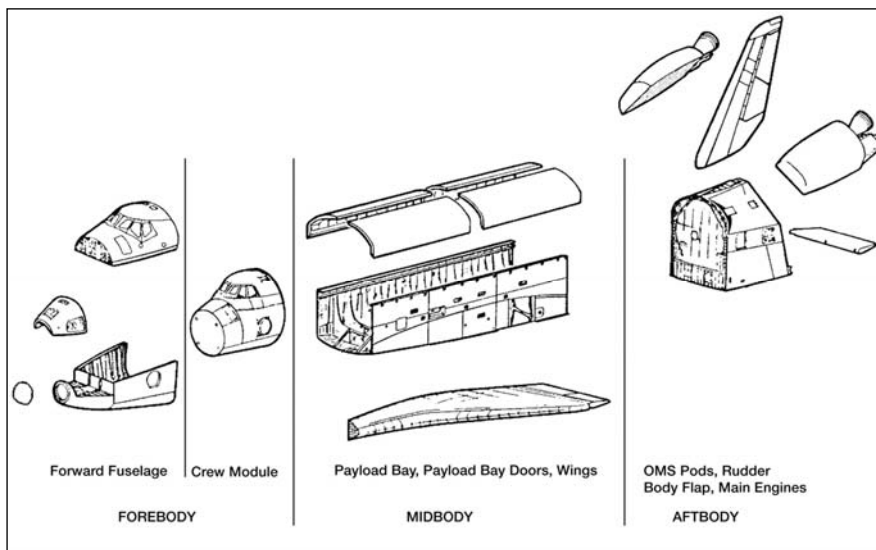


Figure 2.2-12. Depiction of the orbiter forebody, midbody, and aftbody elements.

First, recovered debris longitude data were sorted by respective structural sources. Then, each item became a data point placed into longitude “bins,” each having a range of 0.5 degree. Each bin was then graphed by what percent of the recovered debris fell into what longitude bin. The numbers of debris items in a group ranged from fewer than 100 into the thousands. One bias introduced is that the data were not corrected for these differences in total number when comparing datasets; only the percent of the total recovered from that zone is compared. It is unknown how this difference affects the data overall.

Details of each debris field cluster are presented in the following sections.

Wings

Figure 2.2-12 identifies where the wing structure is in relationship to the other orbiter structural components. TPS tile is included in these figures, as some tile adhered to structure and it was not easily possible to separate out individual tiles. Figure 2.2-13 shows a ground debris map that is similar to that produced in the CAIB Report, Volume I, p. 75; however, figure 2.2-13 shows all the debris for the wings whereas the CAIB map shows only the RCC panels. As the CAIB reported, the left wing failed before the right wing. This is implied in figure 2.2-14 as well. Overlay mapping of debris at their correct latitudes and longitudes prevents easy recognition of their actual ground footprints. The bars shown on the map and in later ground debris maps represent the main cluster of the debris. If coverage extends beyond the map shown, an arrow indicates that the footprint continues off the map. The bar shown above each histogram indicates the longitude range covered by the overlay mapping.

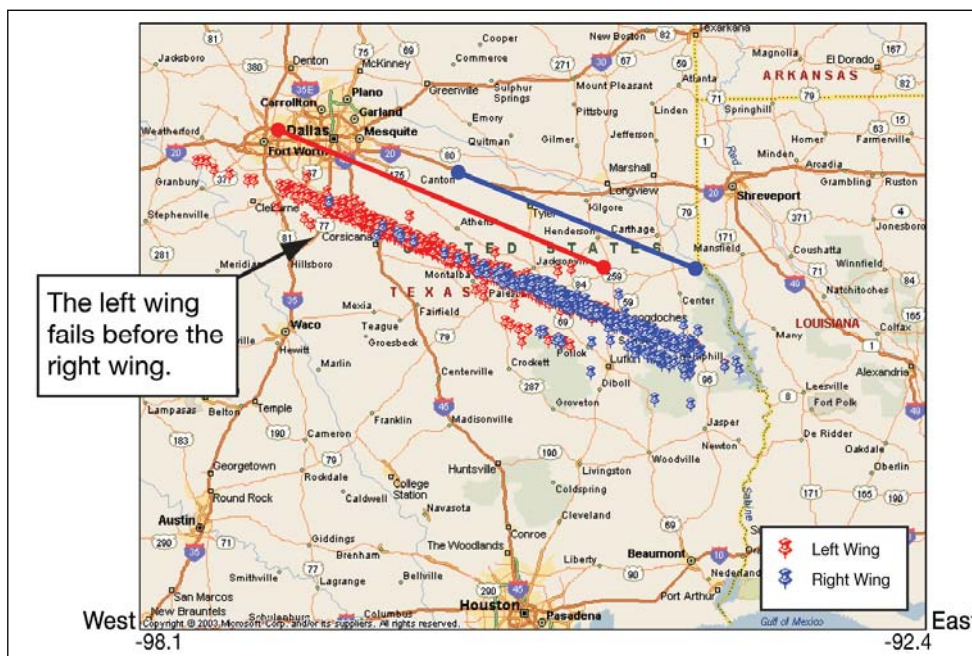


Figure 2.2-13. Debris field of the left and right wings.

Tail (vertical stabilizer)

Figure 2.2-14 illustrates the debris of the tail section in relation to the wing debris. The bulk of the tail debris impacted west of the bulk of the right wing debris. Figure 2.2-15, which is a histogram of longitude vs. the number of debris items, shows this as well. The lines above the histogram indicate the approximate area of the histogram that the debris map covers. Figure 2.2-15 suggests that the tail possibly began to depart between the left wing and the right wing.

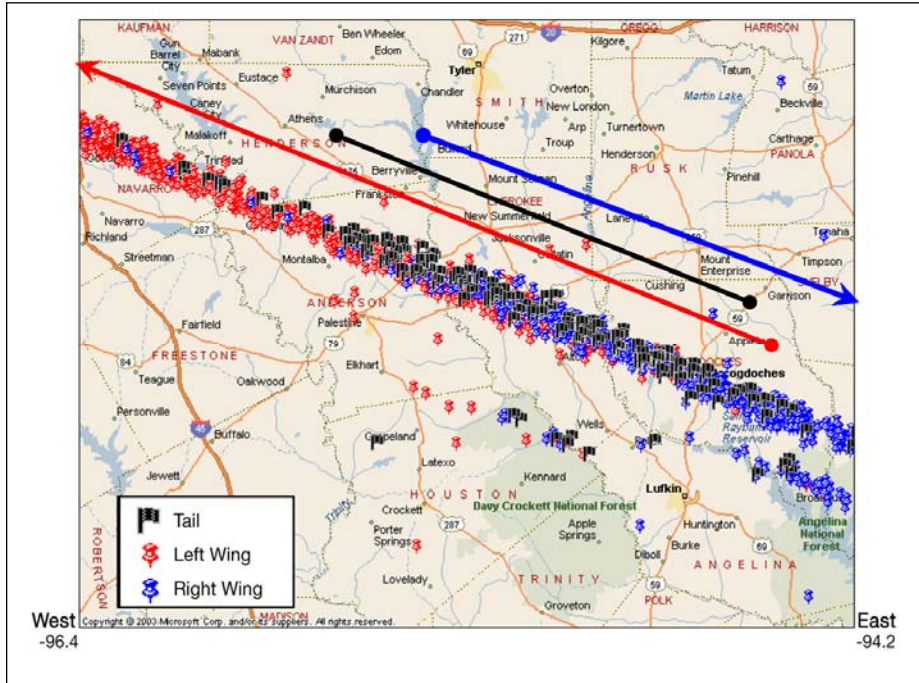


Figure 2.2-14. Partial debris field of the left wing, right wing, and tail.

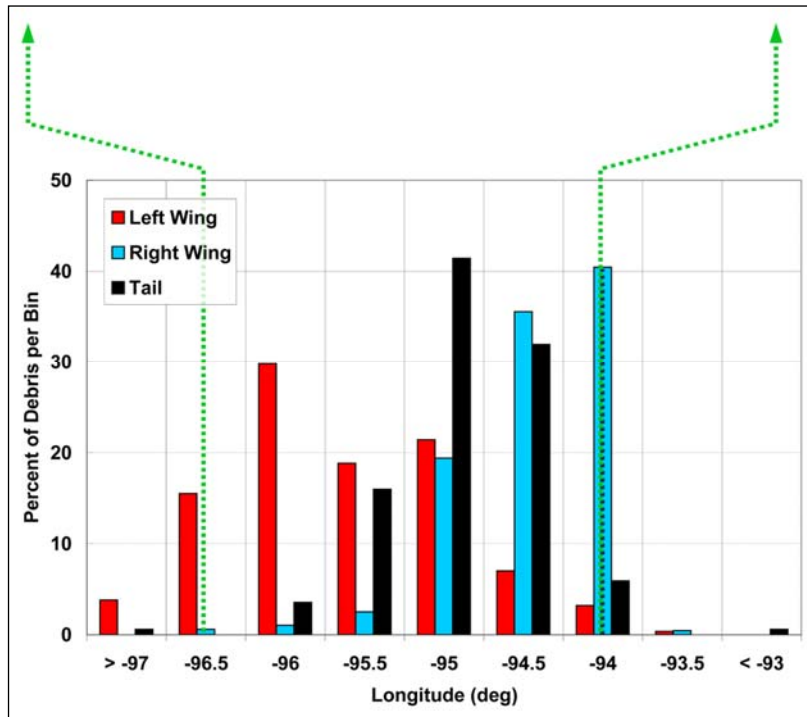


Figure 2.2-15. Histogram of the left wing, right wing, and tail debris. The green dotted lines are the projection onto the histogram of the longitude range shown in the map.

Midbody

Figure 2.2-12 identifies where the midbody is related to the other orbiter structural components. The midbody consisted of the mid fuselage, payload bay, and PLBDs (SPACEHAB is not included in this chart). The midbody began losing structure and shedding objects after the left wing but prior to the tail (figures 2.2-16 and 2.2-17). The midbody debris shown is comprised predominantly of PLBD structure, although pieces of the midbody are scattered throughout the entire debris field.

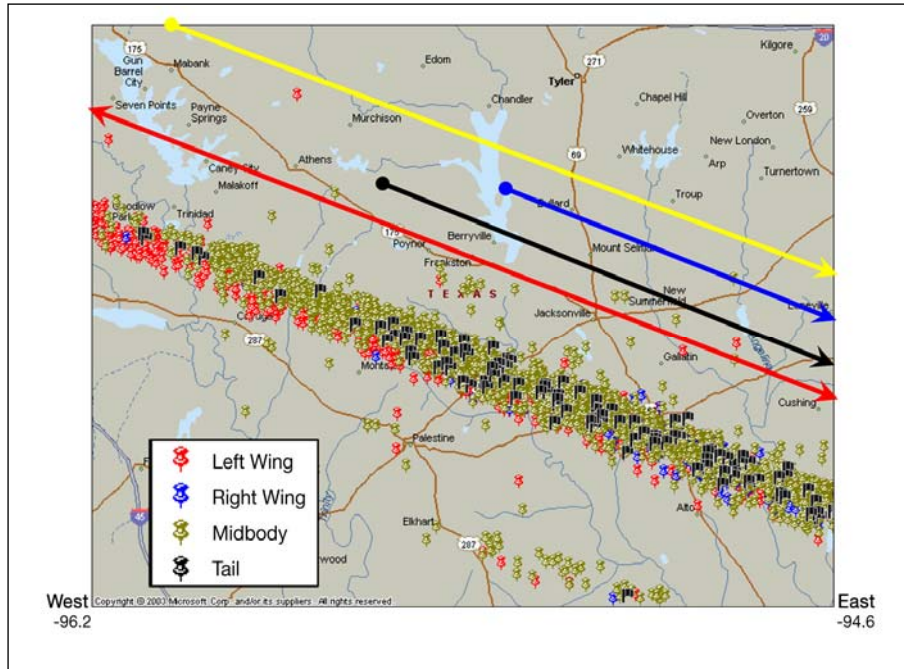


Figure 2.2-16. Partial debris field of the left wing, right wing, midbody, and tail.

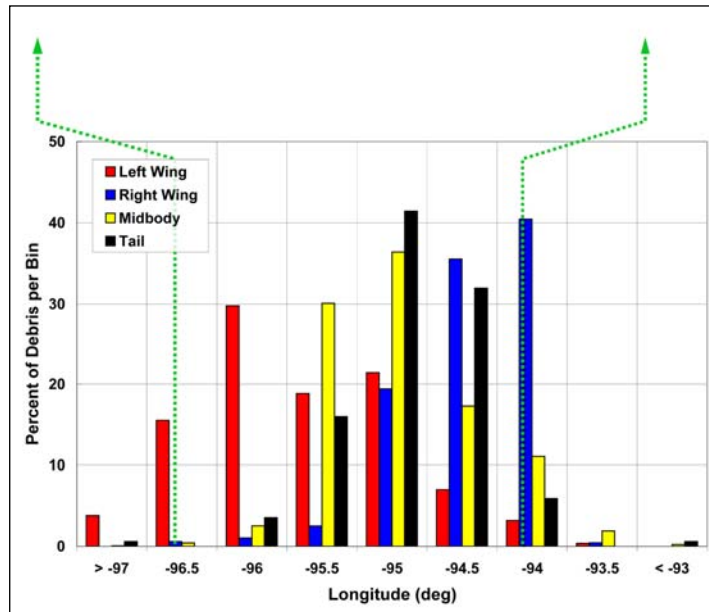


Figure 2.2-17. Histogram of the percentage of debris found vs. longitude for the left wing, right wing, midbody, and tail. The green dotted lines are the projection onto the histogram of the longitude range shown in the map.

Figure 2.2-18 shows the on-ground sequence of the midbody structural debris with right (starboard) and left (port) midbody origins marked where known. Beside the chart is a schematic of the midbody with some positions marked in X_o coordinates for reference. The X_o terminology refers to the X position in inches in the orbiter coordinate frame, where the X axis runs the length of the orbiter from fore to aft in the orbiter X-axis measurements. The nose of the orbiter is at X_o 236" as the coordinate system extends beyond the nose. X_o 582" is the demarcation between the forebody and the midbody. The port lower wing chine and midbody floor skin stretches from X_o 582" to X_o 807" (just forward of the SPACEHAB location). The wing attachment region spans X_o 807" to X_o 1365". The error bars shown on some pieces indicate the range of X_o positions that a piece of debris covered or could originate from, if the range was noted in the database.

The westernmost piece of ground debris from the midbody structure with a known X_o location was a port location just aft of SPACEHAB. However, this appears to be an outlier data point. Figure 2.2-18 indicates that based upon recovered midbody structure, the midbody first suffered a major failure ranging from about X_o 582" to X_o 919".

The next grouping of debris predominantly originates from X_o 776" (towards the aft of SPACEHAB) to aft of the Fast Reaction Experiments Enabling Science, Technology, Applications, and Research (FREESTAR) payload near X_o 1124", although there are a few pieces near the forebody bulkhead (X_o 582").

The final cluster is from the aft region of the midbody. As debris originating from near the midbody aft bulkhead (X_o 1307") appears farthest east in the debris field, this suggests that some midbody payload bay structure remained attached to the aftbody.

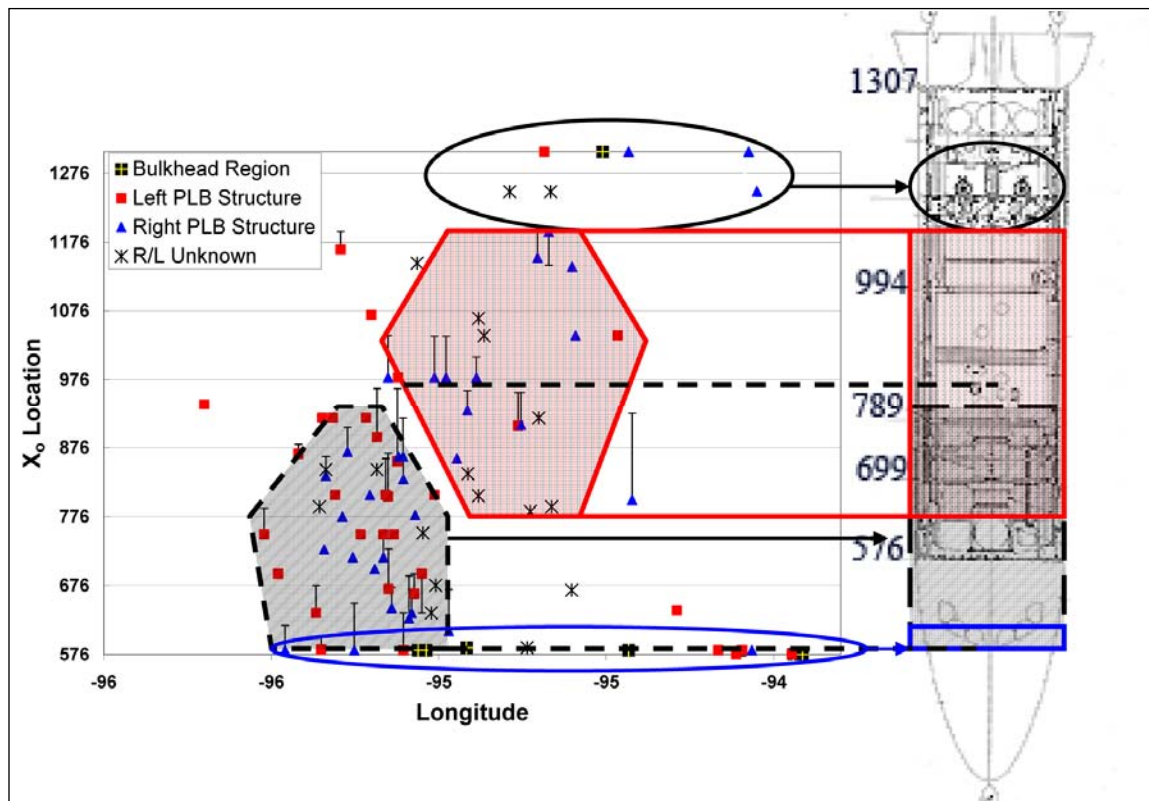


Figure 2.2-18. Longitude vs. the X_o origin of the structural debris of the mid fuselage. To the right is a drawing of the mid fuselage with key X_o positions marked.

The data in figure 2.2-18 cannot be used to determine a port or starboard initiation of breakup of the midbody. Size of individual items was also examined with the assumption that ballistic numbers of objects of roughly the same size and shape will land in the order in which they separate from the orbiter. The number

of objects is small, so this may be an invalid assumption. For smaller-sized midbody debris ($\leq 500 \text{ in}^2$), port debris appears west of starboard debris. For larger-sized debris ($\geq 1000 \text{ in}^2$), starboard debris appears west of port debris. Overall, it is indeterminate whether the port or starboard side failed first based upon ground debris.

SPACEHAB debris was also evaluated (not shown here). SPACEHAB structural debris is concentrated near the forebody debris field, suggesting that the element maintained structural integrity for some period of time as did the forebody.

The midbody *structural* debris (vs. objects contained within the midbody such as SPACEHAB) and the right wing debris fields increase in density at the same time. As shown above, the port and starboard midbody structural debris originating from the same X_o locations begin appearing in the same longitude range (95.5 to 95W). However, in the next longitude range sector (95 to 94.5W), predominantly starboard pieces were recovered. This is the same longitude range sector where the largest number of right wing debris items was recovered. This suggests that a portion of midbody structure and right wing may possibly have initially remained together as a unit when *Columbia* experienced the CE.

Aftbody

The midbody ground debris analysis indicates that at least some of the midbody may have remained with the aftbody. As observed on video, the main engines (the heaviest individual components of the orbiter, with a correspondingly high ballistic number) remained a cohesive unit until GMT 14:00:50.6. Aftbody shedding did occur throughout the period following the CE. Main engine pieces, which were among the easternmost debris objects recovered in the debris field, were found in Fort Polk, Louisiana. Figures 2.2-19 and 2.2-20 show the distribution of the debris field of the aftbody and the left and right wings relative to each other.

Forebody

The forebody breakup sequence is discussed in Section 2.4. The forebody is composed of the FF, CM, nose cap, nose landing gear, and forward RCS.

The debris field shows that the CM and FF failed at nearly the same time, with their debris footprints overlaid on one another. This supports that the forebody remained an integral unit until structural failure, which began at the CMCE. The debris field showed that about 87% of the forebody structural debris appears suddenly; degradation may have occurred, but it was minor until the start of total forebody structural failure. Video corroborates this, showing only minor intermittent debris loss from the forebody until its failure.

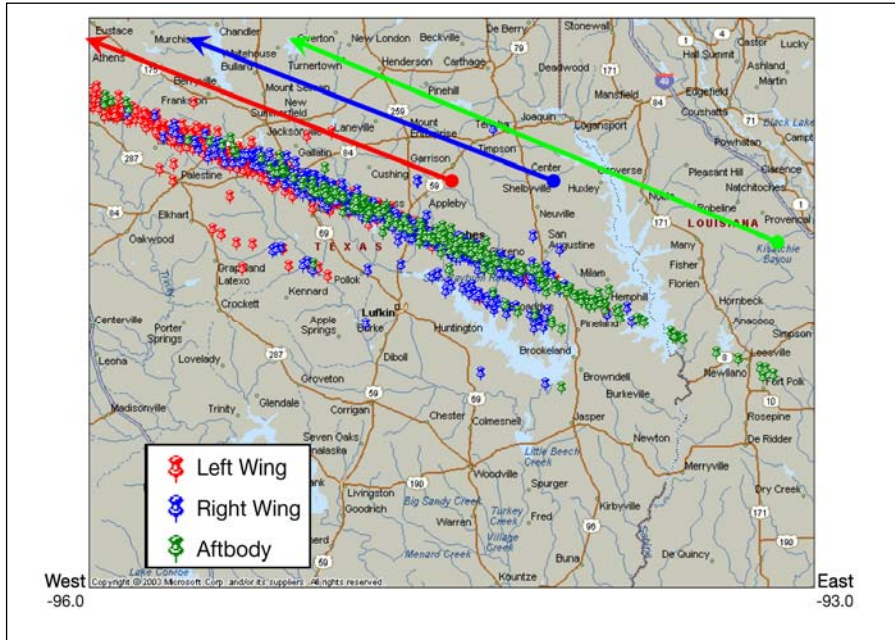


Figure 2.2-19. Partial debris field of the left wing, right wing, and aftbody.

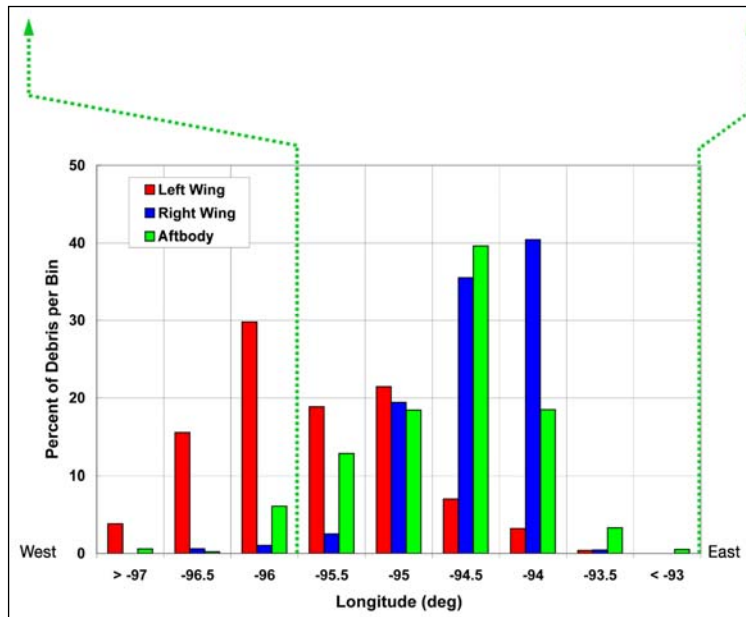


Figure 2.2-20. Histogram of debris of the wings and aftbody (including orbiter main engines). The green dotted lines are the projection onto the histogram of the longitude range shown in the map.

In summary, figure 2.2-21 shows an overall assessment of debris clusters. The westernmost longitude bin of each group that exceeded 30% of the recovered debris group is referenced with an arrow; the label above the bin identifies the debris group. It was observed that when the number of recovered debris items from one orbiter structural zone reached approximately 30%, the next group began to appear in rapidly increasing numbers. The significance of this observation is not known. It may be an artifact of data processing, or it may be characteristic of a cascade effect of structural breakup. This is a topic that may warrant further research and investigation.

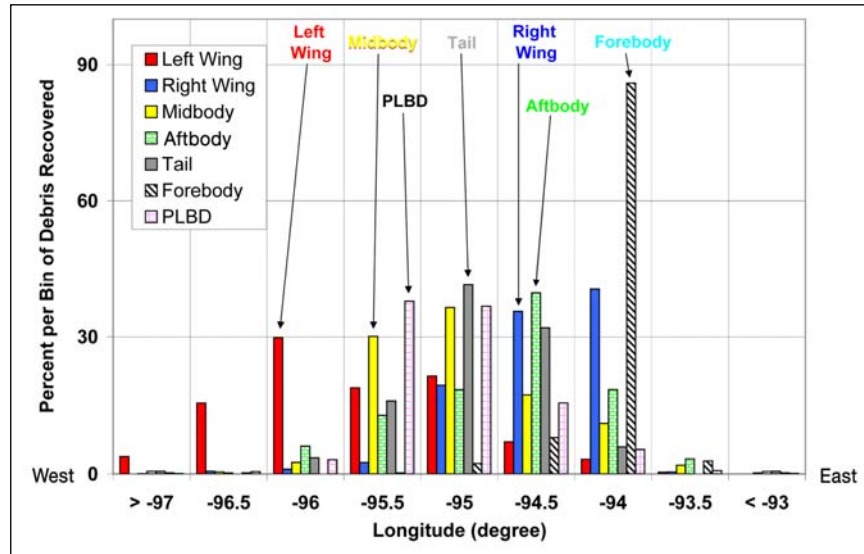


Figure 2.2-21. Histogram of the relative order of the major debris groups recovered.

Cluster analyses show that following the left wing, midbody items (predominantly PLBD pieces) departed the vehicle. The tail, the right wing, and the aftbody shed a significant number of pieces, followed by SPACEHAB and the forebody. Table 2.2-5 shows a comparison of sequencing from cluster analysis compared to video and ballistic analyses.

Table 2.2-5. Comparison of Orbiter Breakup Sequence from Video, Ballistic, and Cluster Analysis

Video Sequence (relative)	Ballistic Sequence (time-based)	Cluster Sequence (relative)
OMS Pod or Left Wing	OMS Pod	Left Wing
	Left Wing	
Forebody/Midbody/Aftbody separation (CE)	Midbody/PLBDs	Midbody
	Right Wing	Vertical Tail
SPACEHAB	SPACEHAB	
	Vertical Tail	Right Wing
	Aftbody breakup	Aftbody breakup
Main Engines separation	Main Engines separate	
Forebody breakup	Forebody breakup	SPACEHAB/Forebody breakup

This relative sequence of cluster-based groups does not match the ballistics reported time-based sequence (Table 2.2-3) of a few debris groups. Specifically, ballistics shows the tail failing before the right wing. This is probably the result of a cascading failure. Based on video, ballistic, and cluster analysis, the conclusion was that the left OMS pod and left wing departed first. It is possible that the PLBDs departed next. At the CE, the orbiter appeared to separate into three main components: forebody, midbody including the right wing, and aftbody. The midbody/right wing and aftbody failed in cascade following the primary breakup event. The forebody failed last.

2.2.4 Structural analysis

2.2.4.1 Background

This section provides a discussion of an analysis and scenario for the orbiter breakup. In addition to the data presented in previous sections, this analysis also draws on the orbiter’s design strengths and weaknesses.

This structural assessment predominantly focuses on events leading up to the CE and the forebody release at the CE, since that was the area of most interest to the team. Little to no assessment was done by the SCSIT structures team on the wings or aftbody since they were not considered relevant enough to this study to warrant the resources.

There are difficulties in understanding and supporting the various theories concerning the orbiter vehicle breakup. Except for the left wing, the vehicle was essentially structurally intact with most systems functioning normally at the time of the last telemetry received (GMT 14:00:05). No recorded on-board data were recovered after GMT 14:00:19, 1 second after the orbiter breakup began. Ground-based video footage does not provide adequate detail to determine the exact sequence of events other than as previously outlined.

Some background regarding the orbiter structure is necessary for this discussion. Orbiter structure is mainly constructed of aluminum components such as riveted skins and stringers, integrally machined plates, honeycomb sandwich panels, frames, bulkheads, and trusses. The exceptions are the OMS pod skins and PLBDs, which are made from graphite epoxy honeycomb sandwich panels, and the aft fuselage thrust structure, which is diffusion-bonded titanium that is reinforced with a boron-epoxy laminate. The payload bay is bounded by a forward bulkhead, the X_o 582 ring frame bulkhead (adjacent to the aft bulkhead of the CM), and an aft bulkhead (located at X_o 1307).

As detailed in figure 2.2-22, the FF is a semi-monocoque structure consisting of aluminum (2024) skins, stringers, longerons, bulkheads, and frames. Its structural purpose is to withstand the loads from the nose landing gear, CM, aerodynamic loads, and CM venting pressure. It also supports the associated portion of the TPS. The forward RCS is considered an integral part of the FF. The FF skin panels were designed primarily based on stiffness requirements to minimize local skin deflection to avoid the cracking or loss of the thermal protection tiles.

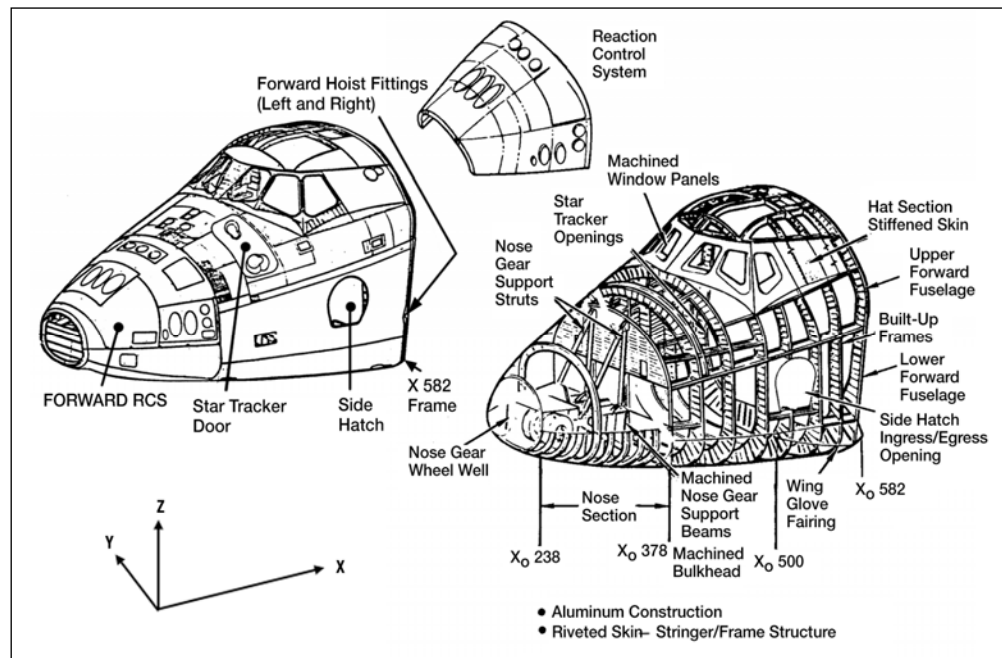


Figure 2.2-22. Forward fuselage structure.

The CM is an airtight pressurized compartment that is constructed from welded aluminum panels (2219 aluminum alloys) with integral stringers, frames, and longerons. It is enclosed and protected by the FF skin panels and the TPS. It is supported and suspended inside the FF by a combination of fittings and linkages.

The CM is supported within the FF at four main attach points made of titanium (figures 2.2-23 and 2.2-24). Side links provide secondary stabilization but do not provide significant structural support. Two major attach points are at the aft end of the flight deck floor level. These links support loading in the X (longitudinal) direction. They also carry 52% of the Z (vertical) direction loading and 34% of the Y (lateral) direction loading. Because these two links carry loads in the X, Y, and Z directions, they are called xyz links, but are generally referred to simply as “x-links.” The x-links bridge the boundary of the X_o 576 bulkhead (aft bulkhead of the CM) and the X_o 582 ring frame bulkhead (the forward bulkhead of the midbody (figure 2.2-25)). The x-links physically connect the CM, the FF, and the midbody structure.

The other links are the z-link and y-links. The z-link (vertical load reaction) is on the centerline of the CM forward bulkhead. The y-links (lateral load reaction) are on the lower portion of the X_o 576 bulkhead; they attach to the X_o 582 ring frame bulkhead. These attach fittings are designed to crash requirements to 9 G in -X (within a 30-deg cone), and ±3 G in the Y and Z axes.

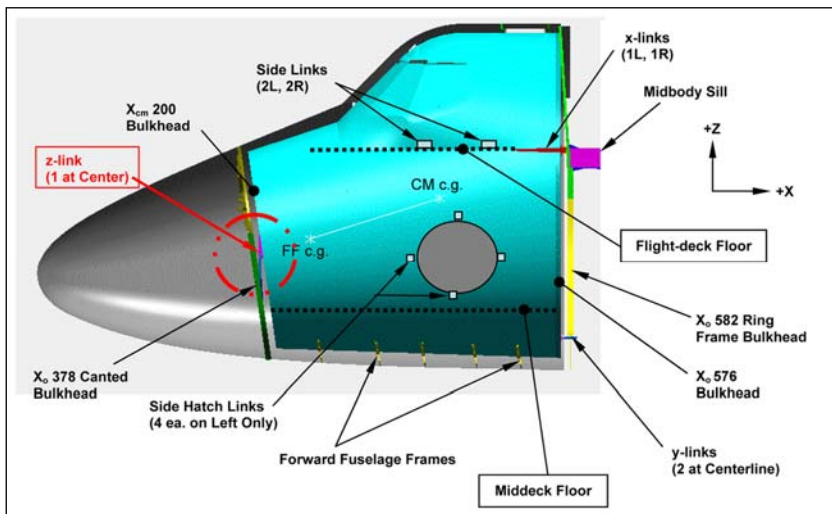


Figure 2.2-23. Thirteen links to the crew module inside the forward fuselage.

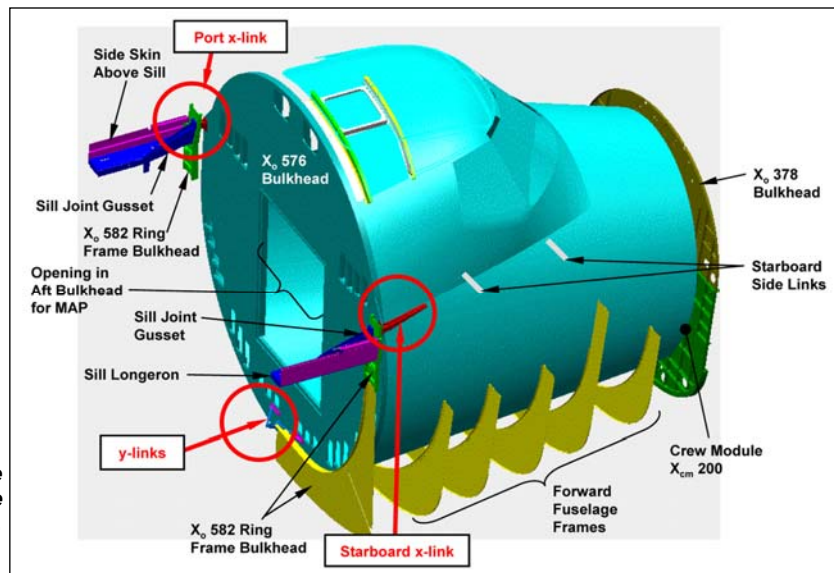


Figure 2.2-24. Crew module support links, starboard-side view.

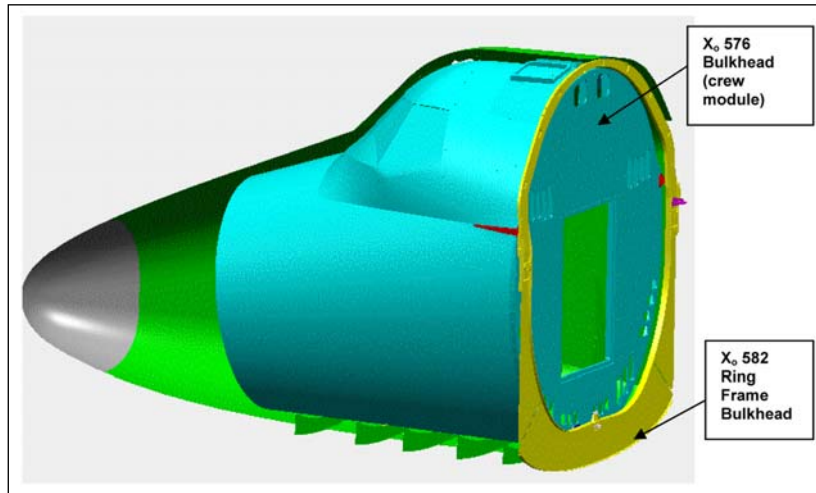


Figure 2.2-25. Picture of the X₀ 576 bulkhead and the X₀ 582 ring frame bulkhead relative to each other.

2.2.4.2 Forebody structure prior to the Catastrophic Event

It is unlikely that any part of the FF experienced major structural failures under the estimated loading before the CE. A motion analysis was performed to compute loads at key locations after the LOC of the orbiter (see Section 2.1). Figure 2.2-26 shows that the estimated G loading at the CM increased to slightly more than 3 G just prior to the CE. Acceleration along the vehicle's Z axis (G_z) is the major component. This analysis assumed intact PLBDs. Loss of the doors may have increased loads in unknown ways such that the motion may have been affected. Assuming that the PLBDs were still intact, the results indicated that inertial loads were within the orbiter vehicle design limits.

Stress analysis also shows that it is unlikely that any of the major CM support links failed before the CE. Even if the temperature at the titanium links were elevated to about 600°F (316°C), the links still would have a high margin of safety before failure.

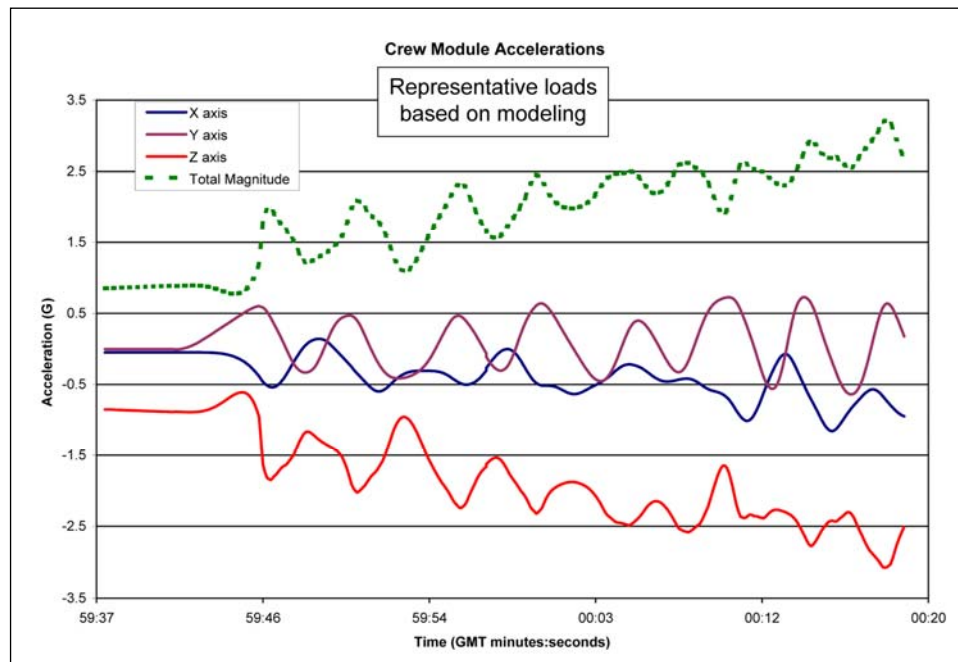


Figure 2.2-26. Resultant acceleration (G) vs. time prior to the Catastrophic Event in the orbiter coordinate frame.

There was no evidence from the ballistic or debris cluster analysis that the forebody suffered any major breach before it separated from the midbody. Figure 2.2-21 (in the debris cluster assessment section) shows that forebody debris does not begin to appear in the debris field until other midbody debris is present in large quantities.

Most of the FF debris components that were recovered west of the main forebody debris field were TPS fragments and external items such as star tracker doors that came from the forward section of the FF, probably due to warping of the skin and aerodynamic loads as the forebody rotated (figure 2.2-27). Approximately 87% of the remaining FF structural debris has the same footprint as the CM debris footprint. This implies that the significant FF structural breakup occurred nearly coincidental with the CM shell breakup.

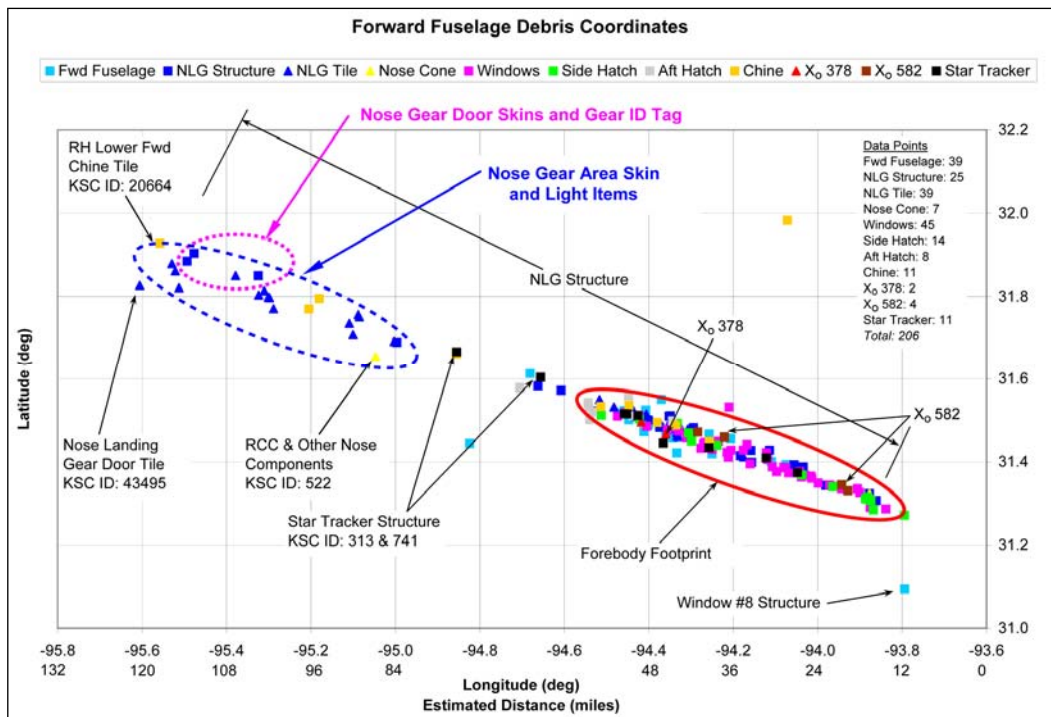


Figure 2.2-27. Forward fuselage debris field.

Two exceptions are the nose landing gear skin items and one landing gear nametag foil that was recovered farther west. These are two very thin pieces of nose landing gear skin and one thin foil piece with very low ballistic numbers, similar to that of the TPS debris.

2.2.4.3 Payload bay doors

During normal entry, the PLBDs and the sidewalls of the midbody are not exposed to high-temperature air flows. After the vehicle lost control, the PLBDs were exposed to abnormal midbody flexing. Also, as the orbiter changed attitude, parts of the vehicle that were not designed for high heating were periodically exposed to the velocity vector and the full force of entry heating. From a structural standpoint, the PLBDs are the most likely place for the first orbiter structural failure that is unassociated with the left wing degradation. RGPC data indicate that the Freon loops in the doors were intact at GMT 14:00:05. Since the Freon radiator loops are an integral part of the doors, this time bounds the earliest time at which the doors could have failed.

Figures 2.2-28 and 2.2-29 show the debris field coordinates for the recovered PLBD debris and a comparison of the PLBD vs. payload bay structures. Ballistics analysis showed very late release times (well past the CMCE)

that were considered suspect and assumed to contain errors due to lift generation and/or cascading events. Evaluation of the PLBD debris vs. payload bay structures shows that the debris field was extremely long, suggesting a very complex breakup and cascading event.

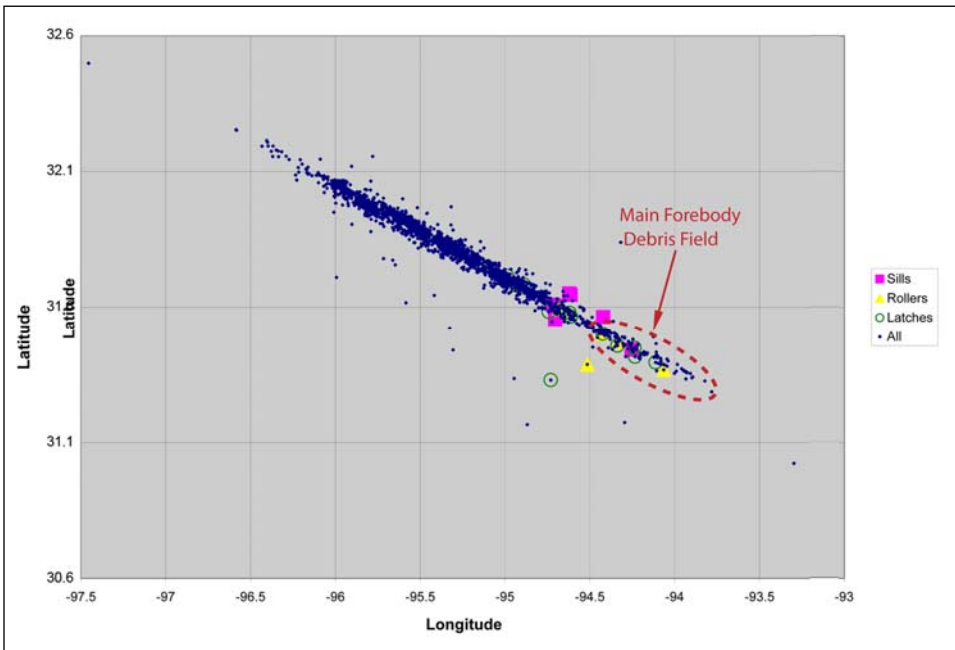


Figure 2.2-28. Payload bay door debris footprint relative to the main crew module debris field.

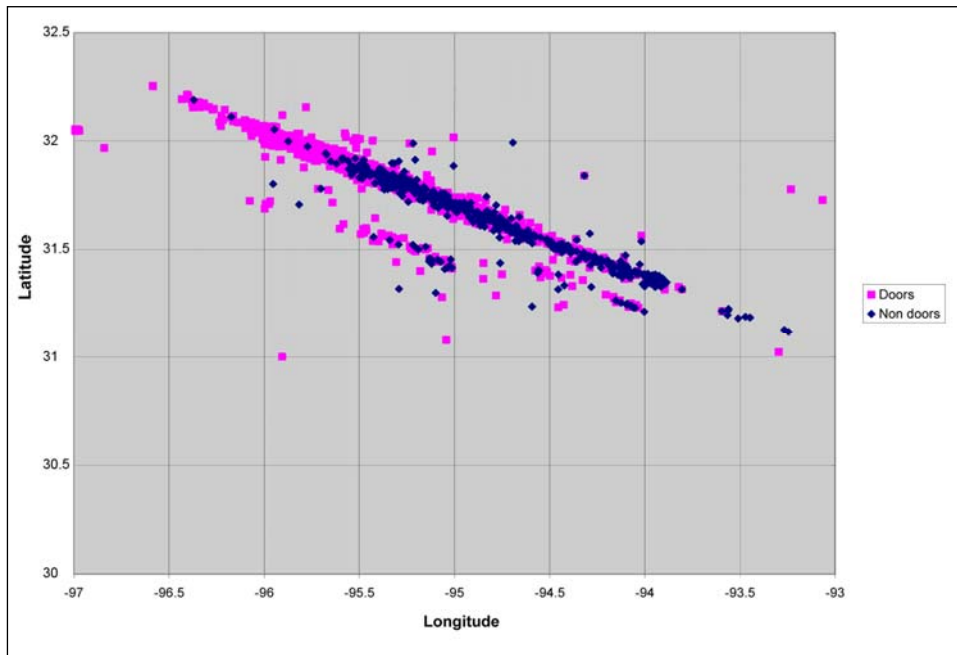


Figure 2.2-29. Payload bay door debris footprint relative to the payload bay structure.

The PLBDs could have begun failing as early as immediately after the last available RGPC data, at GMT 14:00:06, or about 12 seconds before the CE. If this were the case, the debris cluster evidence could be interpreted to indicate that the sills and structural elements of the doors remained intact as a part of a larger section of structure after the departure of the doors.

2.2.4.4 Forebody separation event

Comparison to *Challenger*

Very little *Challenger* data regarding the CM structure were found. Most data were gathered by locating individuals who had performed some part of the assessments. In many cases, anecdotal reports were all that were available. It was anecdotally reported to the team that in the *Challenger* mishap, the CM separated from the orbiter between the X_o 576 and X_o 582 ring frame bulkheads. Figure 2.2-25 shows a picture of the two bulkheads relative to each other. This anecdotal information was subsequently found to be incorrect.

During the CAIB investigation, all *Columbia* debris were evaluated, but only items deemed significant to the cause of the accident were placed on the reconstruction grid and easily accessible. Significant efforts were carried out to identify CM structural debris, but not much was done on the midbody structure. As a result, the initial CSWG debris review resulted in the belief that no material had been recovered from the X_o 582 ring frame bulkhead, although significant elements had been found of the X_o 576 bulkhead. This belief was incorrect. X_o 582 ring frame bulkhead items were recovered; they were simply not readily available for inspection. This oversight led to the assumption that the failure mode was the same for *Columbia*, and this assumption was reported to the CAIB.⁹

However, the SCSIT review of *Challenger* debris photographs clearly showed that part of the X_o 582 ring frame bulkhead was recovered with the *Challenger* X_o 576 bulkhead debris (figure 2.2-30).



Figure 2.2-30. Recovered X_o 576 bulkhead of the *Challenger* crew module showing a portion of the X_o 582 ring frame bulkhead (circled in red).

This discovery led to a detailed search through *Columbia* debris for any recovered portions of the X_o 582 ring frame bulkhead. It should be noted that the X_o 582 ring frame bulkhead contains less mass than the X_o 576 bulkhead (a ring shape rather than a flat plate (figure 2.2-25)) and so significantly less debris would have been expected. As a result of this extensive search, conducted with the assistance of the *Columbia* Research and Preservation Team, four items of X_o 582 ring frame bulkhead debris were found. Plotting the ground coordinates on the debris field (figure 2.2-28) showed that these recovered elements of the X_o 582 ring frame bulkhead impacted the ground well within the recovered forebody debris cluster. This strongly

⁹*Columbia* Accident Investigation Board Report, Volume I, August 2003, p. 77.

suggests that most of the X_o 582 ring frame bulkhead stayed with the forebody and only broke up when the forebody broke up. This is consistent with what appears in the *Challenger* photograph.

Load path assessment

With or without the PLBDs, stress concentrations and the highest structural loading would have occurred in the areas adjacent to the X_o 582 ring frame bulkhead (attachment of the forebody to the midbody) and X_o 1307 bulkhead (attachment of the aftbody to the midbody). At the X_o 1307 bulkhead, the wings and wing carry-through structures provide the area with some additional strength. Structural assessment shows that the weaker link is at the X_o 582 ring frame bulkhead area because this area must react to a more concentrated loading from the CM through the two x-links attaching to the midbody sill longerons.

By design, the forward splice of the X_o 582 ring frame bulkhead is much stronger than the aft splice because this bulkhead was built integrally with the FF shell and attached to the FF by multiple longitudinal frames or longerons, while the aft of the bulkhead is spliced to the midbody by only two sill longeron joints and the lower/side skin splice.

Without the PLBDs, the weak zone between the forebody and the midbody is the sill joint gusset on the aft side of the X_o 582 ring frame bulkhead (figure 2.2-31). This gusset is an offset structural connection that transfers the major X-axis loads from the CM to the midbody sill longeron via the x-links.

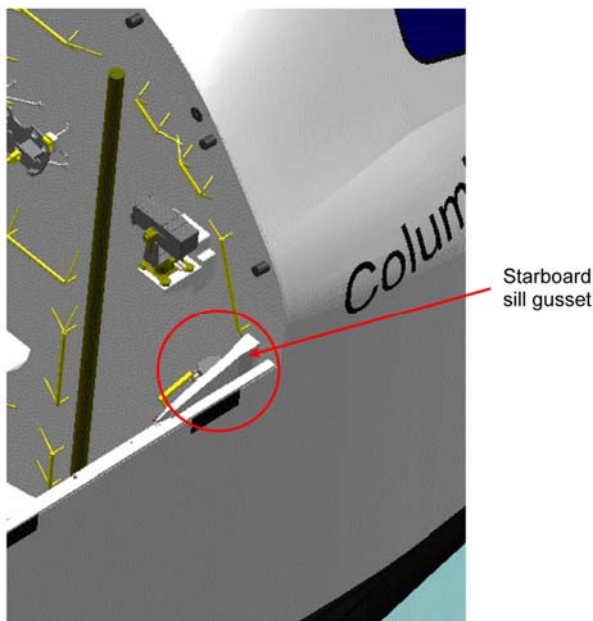


Figure 2.2-31. Close-up of the starboard sill gusset area.

This assessment agrees with the debris field assessment finding that the X_o 582 ring frame bulkhead stayed with the forebody at the CE.

Midbody and X_o 582 ring frame bulkhead structure comparison

The midbody and forebody skin debris that originated from near the X_o 582 ring frame bulkhead was evaluated for confirming evidence. Specifically, the two forward hoist fittings that were used to lift the orbiter during ground processing and were aligned with the X_o 582 ring frame bulkhead, and the lower midbody skin from Bay 1, the forward-most section of the payload bay that is adjacent to the X_o 582 ring frame bulkhead, were evaluated.

The recovered starboard forward hoist fitting (figure 2.2-32) is still attached to FF skin. This is evidence that the midbody skin separated from the FF structure aft of the X_o 582 ring frame bulkhead. It was recovered

from the westernmost portion of the forebody debris field. The green-colored Koropon primer shown in the photograph is similar to the condition of the side skin a few feet above it (figure 2.2-33), which was recovered near the center of the forebody debris field. These elements most likely stayed with the forebody after the CE and only departed at the forebody breakup event. Temperatures above 400°F (204°C) degrade the primer's appearance, and high temperatures (>900°F) (486°C) will completely ablate it. The presence of Koropon indicates that the breakup of these elements was caused by mechanical overload rather than thermal effects. The presence of intact primer indicates that the FF TPS protected this area from entry heating until the forebody breakup at the CMCE.

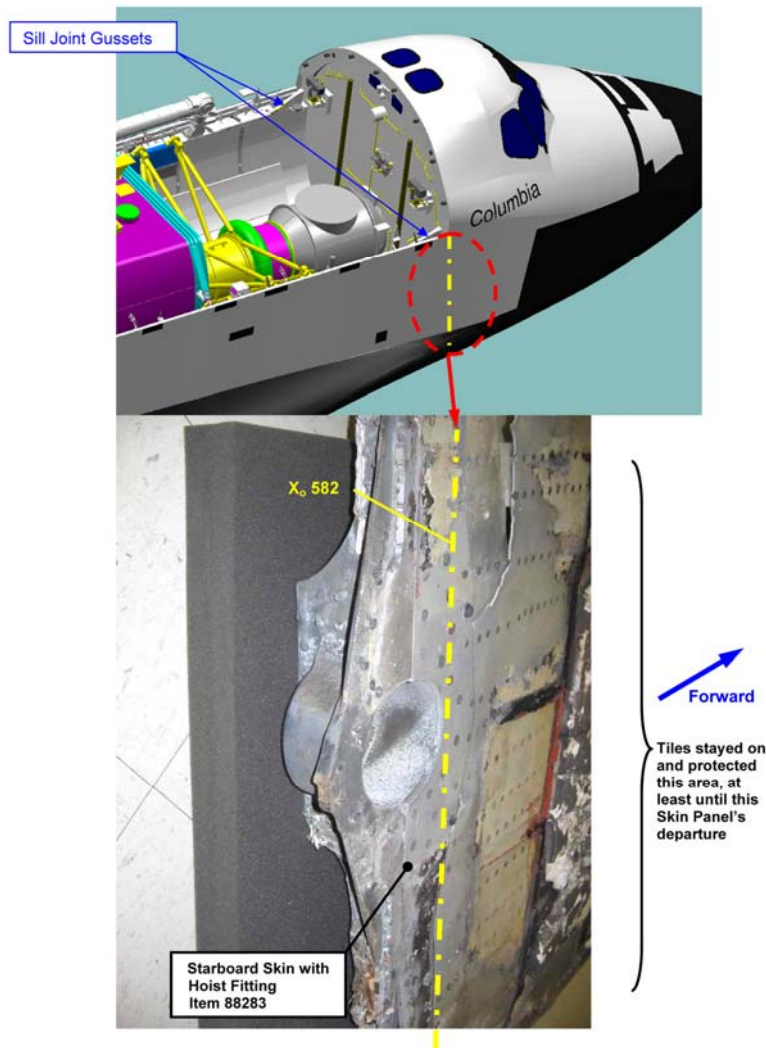


Figure 2.2-32. Forward fuselage skin still attached to the starboard hoist fitting.

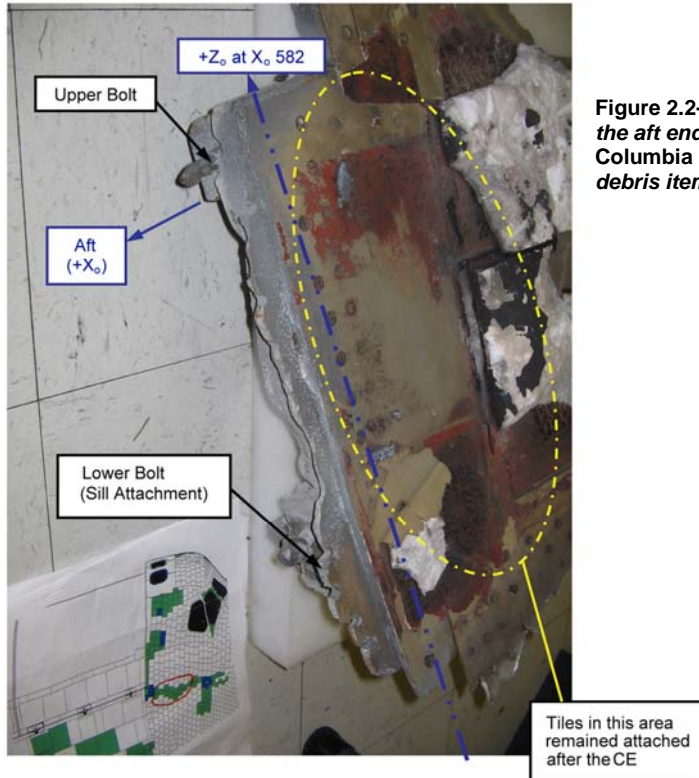


Figure 2.2-33. Thermal erosion on the aft end of the starboard-side skin, Columbia Reconstruction Database debris item no. 2436.

The condition of the recovered forward portside hoist fitting (figure 2.2-34) indicates that the Xo 582 ring frame bulkhead likely broke away from the midbody skin via mechanical failure, prior to any thermal effects. The Bay 1 side skin pulled away because of mechanical failure. The midbody skin splice severed the fasteners from the titanium hoist fitting by mechanical force, some Hilok bolts were cut off, and some flush bolt heads pulled through the skin splice. This damage, which may have occurred at the CE, suggests that the forebody yawed left and pitched down relative to the midbody. This motion may also have broken the port x-link lug (discussed in the next section). This kind of mechanical failure could only happen when the hoist fitting was still attached to the FF, when sufficient mass existed to exert this level of force.

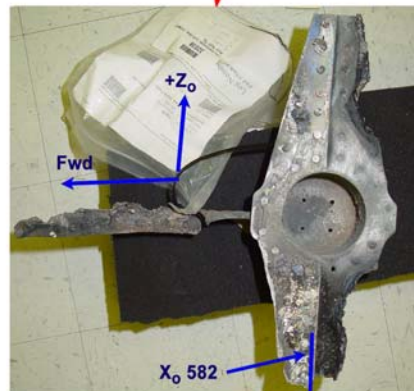
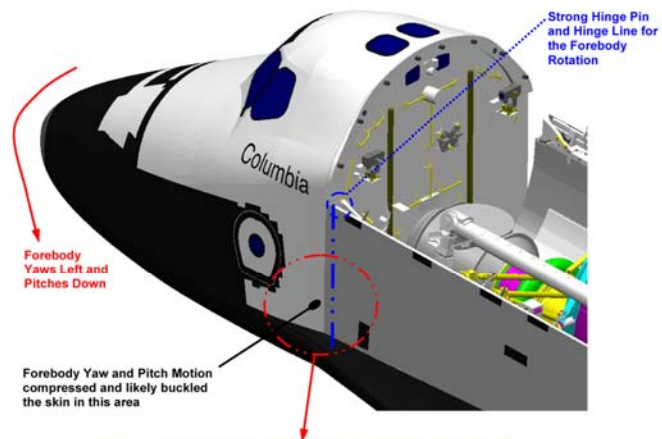


Figure 2.2-34. Forward port hoist fitting, Columbia Reconstruction Database debris item no. 32038.

Unlike the starboard hoist fitting, the skin panel forward of the port hoist fitting was not recovered. One possible explanation is that the FF skin on the forward side of this item was deformed or wrinkled by compression loading at the CE when the forebody yawed left and pitched down. This may be supported by the fact that the port forward hoist fitting was recovered in the middle of the forebody debris field while the starboard hoist fitting was found in the western end of the debris field. Wrinkled skin most likely debonded TPS tiles, so this area would be subjected to thermal flow damage on at least the skin-side surface starting at the CE, then on both sides after it departed from the forebody after the CMCE. Alternatively, the port area may have simply stayed intact longer and received more entry heating following the CMCE.

The recovered midbody bottom skin pieces from Bay 1 (the most forward bay in the midbody, immediately aft of the X₀ 582 ring frame bulkhead (figures 2.2-35, 2.2-36, and 2.2-37)) show little or no heat damage to the skin at the splice aft of the X₀ 582 ring frame bulkhead. The damage is mainly mechanical breakup of the frame to skin splice.

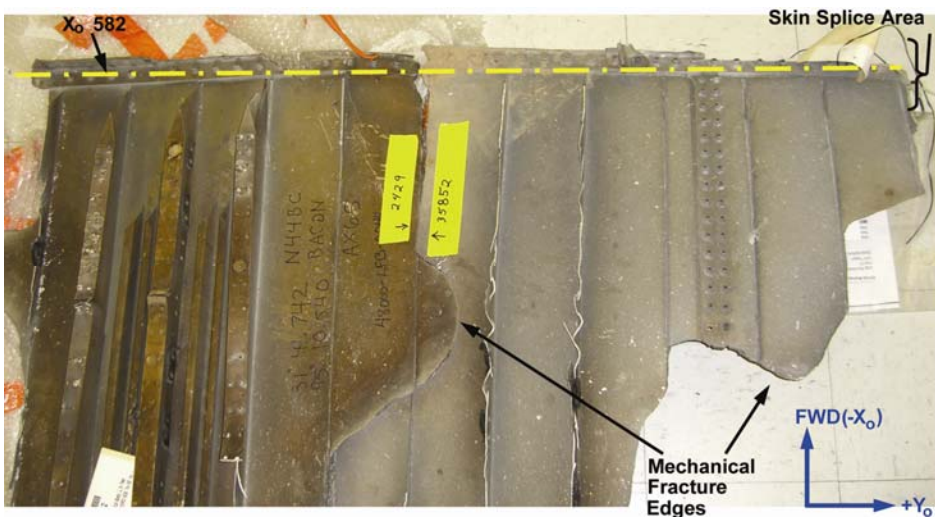


Figure 2.2-35. Bay 1 midbody bottom skin, Columbia Reconstruction Database debris item nos. 2429 and 33852.



Figure 2.2-36. Bay 1 midbody skin, Columbia Reconstruction Database debris item no. 88290.

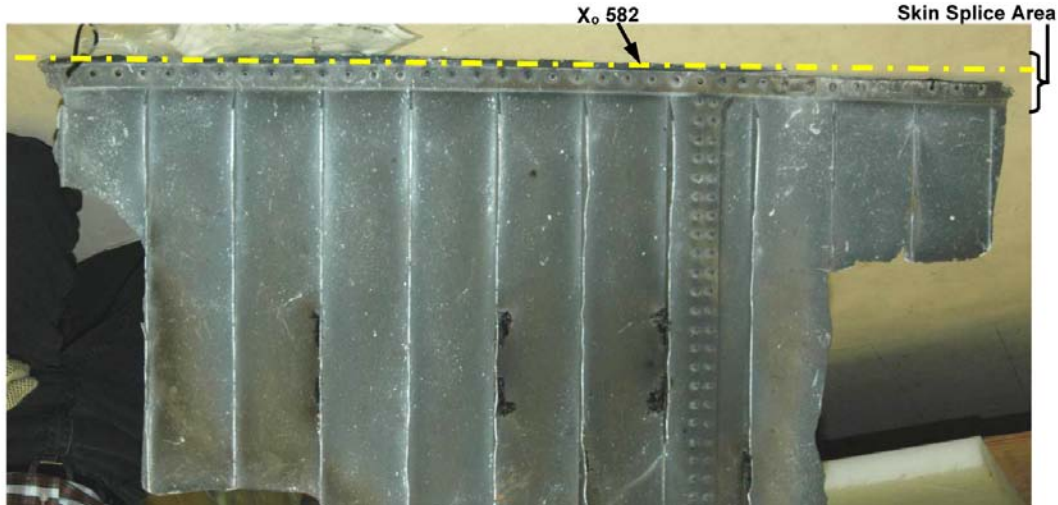


Figure 2.2-37. Bay 1 midbody skin, Columbia Reconstruction Database debris item no. 14908.

The *Columbia* Reconstruction Team noted that thermal damage to the midbody was not generally severe.¹⁰ The thin skin and stringers of Bay 1 experienced some heating but not sufficient to melt the material. One scenario that may explain this is that this bay corresponded to the X location of the structural failure and disintegrated quickly during or immediately after the CE. Even if the bay skin remained with the midbody at the CE, without the X_o 582 ring frame bulkhead frame aerodynamic loads would peel off the Bay 1 skin quickly. This is consistent with the interpretation that the forebody and midbody separated in this area.

Crew module attach fittings

The primary attach fittings of the CM to the forebody are the x-links, the y-links, and the z-link (figures 2.2-23 and 2.2-24). All are made of titanium. The x-links also connect the FF and CM to the midbody and will be addressed here. The y-links and z-link will be discussed in Section 2.4.

The x-links are normally protected by the PLBDs, which also provide stiffness for the orbiter. By design, the x-link attachment to the CM is stronger than its attachment to the FF and midbody because it is attached to the extension webs of the CM flight deck floor and X_o 576 bulkhead.

Comparison of the recovered port and starboard x-links (figure 2.2-38) shows two important differences. First, the starboard x-link was recovered with a portion of the X_o 582 ring frame bulkhead and starboard sill attached, while the port x-link failed forward of the X_o 582 ring frame bulkhead. Second, the starboard x-link experienced much more thermal erosion than the port x-link. It is clear that the directionality of the thermal damage (aft to forward flows above the x-links, and forward to aft flows along the bolt heads) is the same on both links. This orientation was shown to be unlikely due to a common trim attitude when free-flying (see Section 2.1). This strongly suggests that they were in the same relative orientation (still attached to forebody structure) when exposed to heating. The common thermal pattern on the x-link body is discussed in Section 2.4.

¹⁰STS-107 *Columbia* Reconstruction Report, NSTS-60501, June 2003, p. 55.

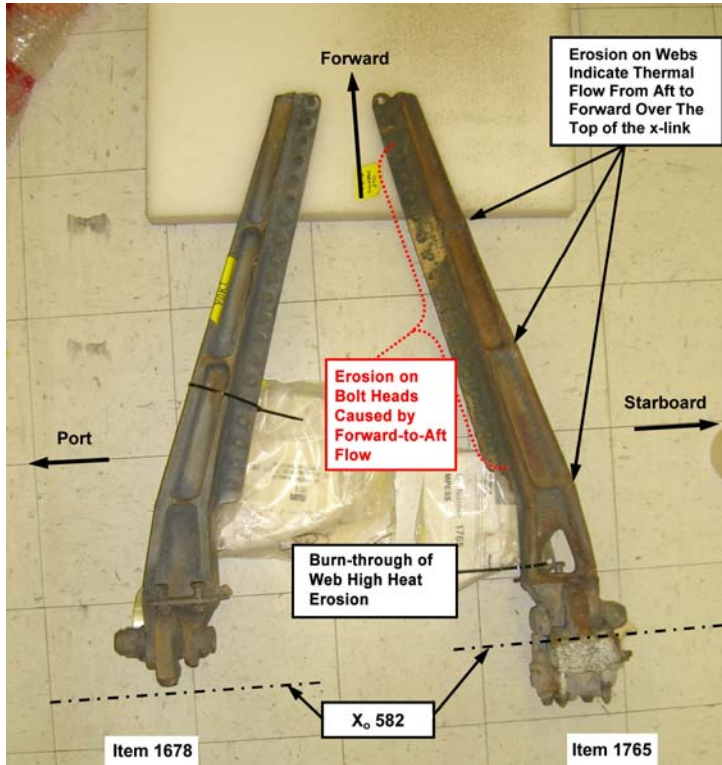


Figure 2.2-38. Port and starboard x-links.

Starboard x-link assessment

Figures 2.2-39 and 2.2-40 show the heavy thermal erosion on the sill joint gusset that is attached to the starboard x-link. The portion of side skin splice from just outboard of the starboard x-link was also recovered. Heavy heat erosion was noted on the midbody side (aft side of X_o 582 ring frame bulkhead), but was not significant elsewhere on the debris. This skin panel was recovered near the center of the forebody debris field. Together, this confirms that the CM stayed inside the FF shell until the forebody breakup, and suggests that the trailing edge (midbody side) was exposed to heating.

The structure aft of the X_o 582 ring frame bulkhead on both the starboard covering side skin and the starboard x-link was heavily damaged by heat. The heat erosion pattern on bolt heads on the aft side shows that the higher (+Z) and outboard (+Y) bolts experienced more heat erosion than the lower/inboard bolts. The resulting shape of eroded bolt heads indicates

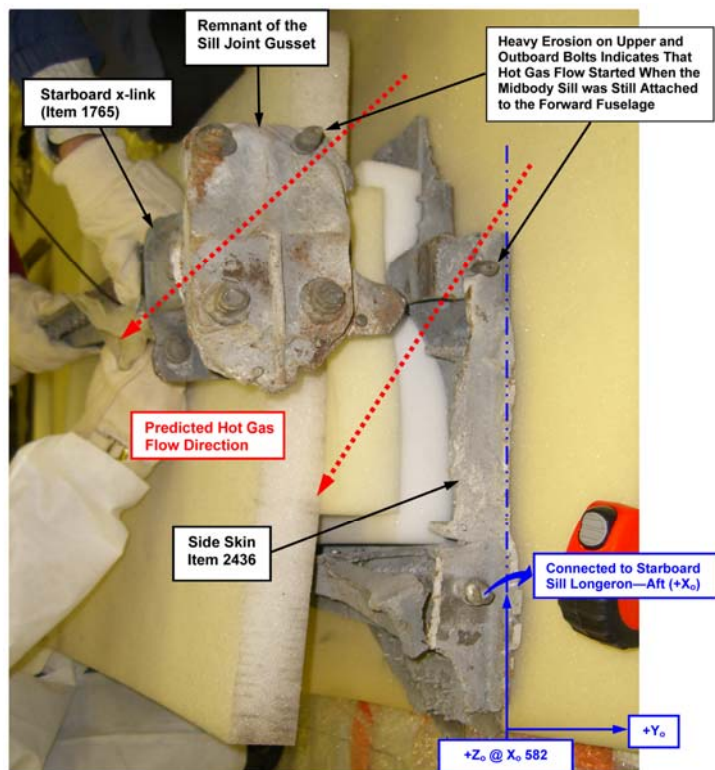


Figure 2.2-39. View looking forward at the starboard x-link and side skin.

that hot gas flowed down and inboard (figures 2.2-39 and 2.2-40). This suggests that the aft side of the starboard x-link area was exposed to hot gas while the starboard midbody sidewall/sill was still attached to the X_o 582 ring frame bulkhead and FF.

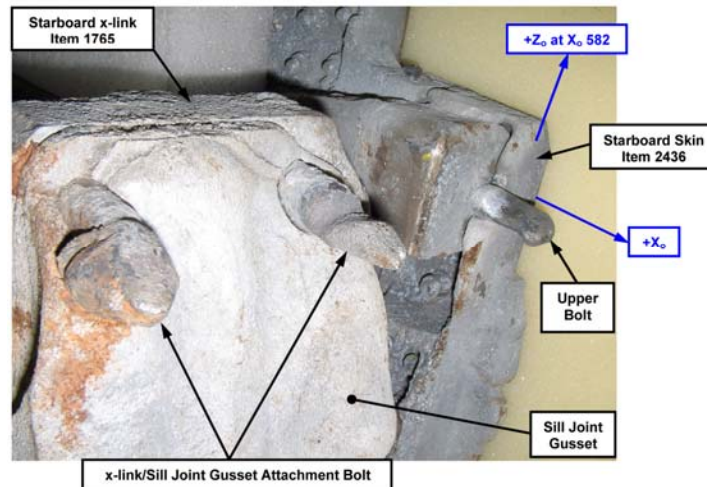


Figure 2.2-40. Detail of thermal erosion on the upper bolts at the starboard x-link and skin.

Hot gases flowing over the starboard sill and X_o 582 ring frame bulkhead could elevate the temperature of the starboard structural joint between the sill and the FF behind the starboard x-link while the sidewall shielded the lower portions of these structures. It appears that the sill and the sidewall were still attached to the FF when this thermal erosion took place. The condition of the remaining bolt heads indicates that these bolt heads and shanks did not fail by mechanical loading.

To summarize the assessment, the point of the orbiter that was weakest under dynamic rotational loading was likely to be the sill gusset immediately aft of the x-link and the X_o 582 ring frame bulkhead. Debris shows that for the starboard sill, the failure of the midbody sill joint occurred at a location aft of the X_o 582 ring frame bulkhead, perhaps near the middle of the gusset (figures 2.2-41 and 2.2-42). Since orbiter load limits were apparently not exceeded, this implies that thermal degradation was required.

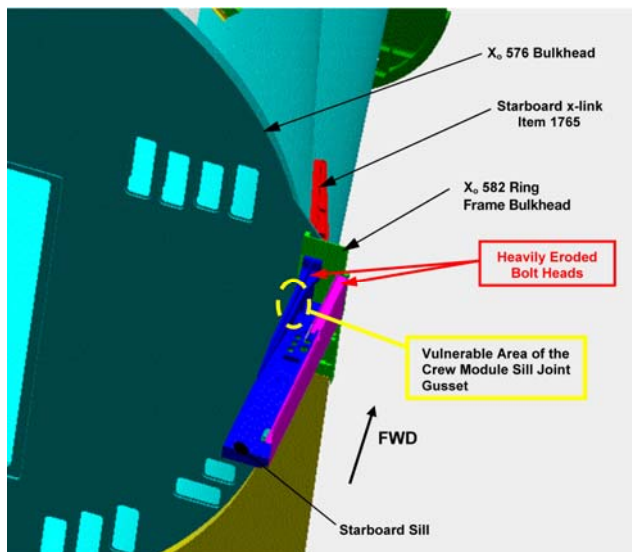


Figure 2.2-41. Weak links – sill joint gusset, starboard side.

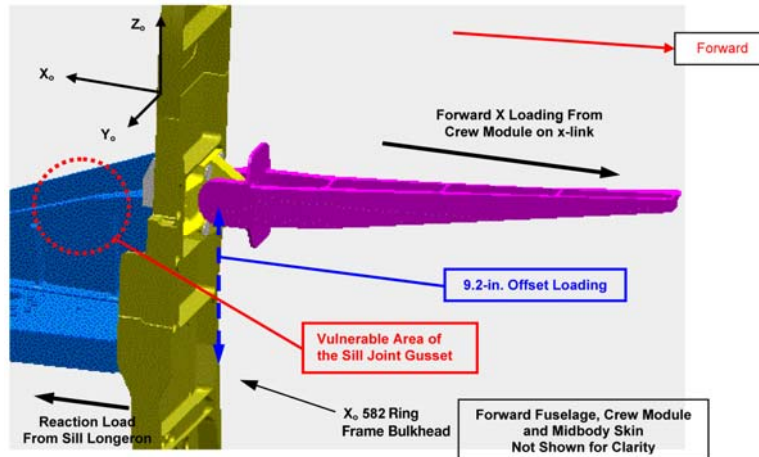
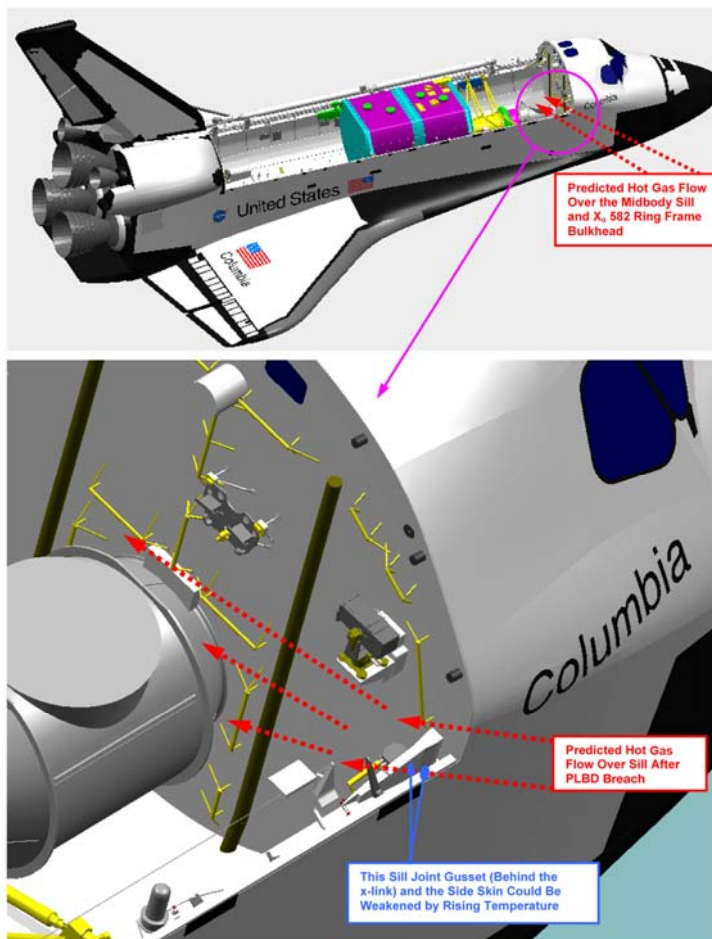


Figure 2.2-42. Structural loading from starboard x-link to sill longeron.



This thermal degradation could have occurred prior to the CE if the PLBDs departed or were compromised in that area (figure 2.2-43). Debris evidence shows that the starboard sill joint experienced more thermal damage than the port sill joint. This suggests the possibility that rising temperature on the starboard sill area weakened the sill joint until it failed mechanically. Although orbiter motion generally resulted in “belly-into-the-wind” orientation (see Section 2.1), with the large pitch and roll oscillations hot gas could flow beyond the belly of the orbiter, up and over the sill. However, hot gas exposure to the sill area could only be short and intermittent (<3 seconds at a time). Debris field and ballistic assessment of PLBD debris is inconclusive. However, a local failure or compromise on the starboard PLBD near the sill could have resulted in this scenario without evidence being apparent in these assessments.

Figure 2.2-43. Hot gas flow heats up starboard sill and the adjacent x-link.

It is unlikely that the temperature increase on the starboard-side sill joint was the primary cause in the orbiter breakup. High heating most likely played a contributing role for the starboard sill joint failure. The main cause for the sill joint failure was probably mechanical loading exceeding the capability of the thermally weakened structure. A failure in this location would likely cascade structural failures along load paths throughout the vehicle.

As illustrated in figure 2.2-44, failure of the starboard sill joint area would trigger a separation of the forebody away from the midbody. Starting from the starboard side, the midbody skin splice would fail progressively, opening from starboard to port at the forebody aft bulkheads.

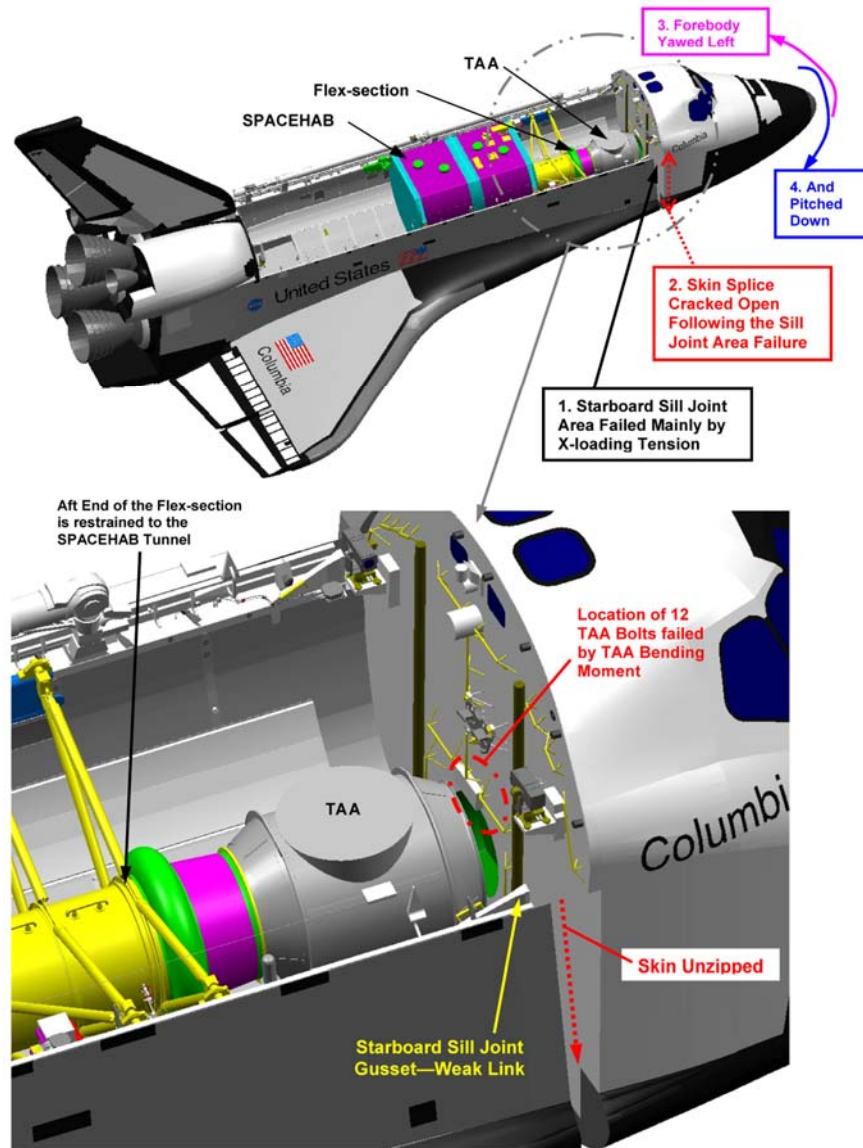


Figure 2.2-44. Forebody departed the midbody at the Catastrophic Event.

The other possibility is that a portion of the starboard midbody remained with the forebody after the CE and failed during subsequent motion of the forebody. However, it is unlikely that the forebody separated the midbody farther aft of the starboard sill joint area unless the farther aft area had been damaged earlier because of other thermal or mechanical causes, for which there is no clear evidence.